Chemical Geology 511 (2019) 279–313

Contents lists available at ScienceDirect

Chemical Geology

journal homepage: www.elsevier.com/locate/chemgeo

Cycles of trace elements and isotopes in the ocean – GEOTRACES and beyond

The elemental composition of the deep particle flux in the Sargasso Sea☆

M.H. Conte[a,b,*], A.M. Carter[b,1], D.A. Koweek[b,2], S. Huang[b,3], J.C. Weber[b]

[a] *Bermuda Institute of Ocean Sciences, St. Georges GE01, Bermuda*
[b] *Ecosystems Center, Marine Biological Laboratory, Woods Hole, MA 02543, USA*

ARTICLE INFO

Editor: Michael E. B

Keywords:
Particle flux
Trace elements
Oceanic Flux Program
Bermuda
Sargasso Sea
Sediment traps

ABSTRACT

The elemental composition of the deep particle flux at 500 m, 1500 m and 3200 m was measured at the Oceanic Flux Program (OFP) time-series site in the northern Sargasso Sea from September 2000 to March 2015. The results clearly show that the deep particle flux is sourced from two components: an "extrinsic flux" component that is derived from and temporally coupled with recent surface export fluxes, and an "intrinsic flux" component that is derived from chemical scavenging and suspended particle aggregation within the deep water column. Elemental fluxes show a seasonal cycle that is closely tied to the overlying cycle in primary production. Fluxes of biogenic minerals and nutrient elements peak during the late winter-spring maximum in overlying primary production. A small late winter-spring peak in fluxes of non-biogenic elements suggests that intrinsic flux generation within the deep water column also covaries with overlying production and the extrinsic flux. Flux elemental composition also shows a marked seasonal cycle that reflects dilution of the intrinsic flux in the late winter and spring with fresh biogenic materials sourced from recent overlying production. Factor of four increases in lithogenic element fluxes and lithogenic element ratios indicate that the source of the deep lithogenic flux is not Saharan dust but North American margin sediments that have been resuspended and advected to the region via Gulf Stream recirculation. High rates of authigenic mineral precipitation accompany organic matter degradation in mesopelagic waters. The excess Mn flux (i.e. flux not supported by lithogenic minerals) increases by an order of magnitude between 500 m and 1500 m, and the excess Ba flux increases by a factor of three. There is a major reorganization of element associations with flux carrier phases with increasing depth. In particular, the geochemical behavior and flux of P becomes increasingly independent of organic carrier phases and the geochemical behavior of Fe, Co, Ni, Cu and, to a lesser extent, V and Pb becomes increasingly controlled by manganese oxide scavenging.

This article is part of a special issue entitled: "Cycles of trace elements and isotopes in the ocean – GEOTRACES and beyond" - edited by Tim M. Conway, Tristan Horner, Yves Plancherel, and Aridane G. González.

1. Introduction

The oceanic particle flux controls the distributions and geochemical behavior of many elements (Collier and Edmond, 1984; Bruland and Lohan, 2003; Jeandel et al., 2015). Some elements are actively taken up by phytoplankton as trace nutrients (e.g. Martin and Knauer, 1973; Saito and Moffett, 2002; Morel and Price, 2003; Cullen and Maldonado, 2013; Twining et al., 2015) or as components of skeletal materials and become directly incorporated into the biogenic particle flux. Other elements become incorporated into biogenic particles through processes of elemental substitution (e.g. Price and Morell, 1990; Morse and Bender, 1990; Sunda and Huntsman, 1995; Ellwood and Hunter, 2000; Gehlen et al., 2002; Sternberg et al., 2005), bioaccumulation (e.g. Reinfelder and Fisher, 1991; Wang et al., 1996; Carvalho et al., 1999), chemical scavenging onto particle surfaces (e.g. Balistrieri et al., 1981; Yao and Millero, 1996; Clegg and Sarmiento, 1989; Gunnars et al., 2002; Nelson et al., 2002), and precipitation of authigenic minerals such as barite (Bishop, 1988; Griffith and Paytan, 2012) and Mn-Fe oxyhydroxides (Cowen and Bruland, 1985; Statham et al., 1998; Cowen, 1992; Tebo et al., 2004; Bargar et al., 2005). Elements in

---

☆ This article is part of a special issue entitled: "Cycles of trace elements and isotopes in the ocean – GEOTRACES and beyond" - edited by Tim M. Conway, Tristan Horner, Yves Plancherel, and Aridane G. González.

* Corresponding author at: Ecosystems Center, Marine Biological Laboratory, 7 MBL St., Woods Hole, MA 02543, USA.
E-mail address: mconte@mbl.edu (M.H. Conte).

[1] Current address: Nicholas School of the Environment, Duke University, Durham, NC 27708, USA.
[2] Current address: Dept. Global Ecology, Carnegie Institution for Science, Stanford, CA 94305, USA.
[3] Current address: AIR Worldwide, Boston, MA 02116, USA.

https://doi.org/10.1016/j.chemgeo.2018.11.001
Received 12 March 2018; Received in revised form 18 October 2018; Accepted 3 November 2018

Table 1
Percent loss of elements from the flux material into the trap cup supernatant during deployment. Supernatants were analyzed in trap samples recovered in March 2009 (sampling dates Nov 2008–Mar 2009).

Element	Depth								
	500 m (n = 8)			1500 m (n = 10)			3200 m (n = 10)		
	Average	Min	Max	Average	Min	Max	Average	Min	Max
Mg	< 0.1			< 0.1			< 0.1		
Al	< 0.1	0.1	0.8	< 0.1			< 0.1		
Si	9.7	5.8	15.8	5.7	3.3	8.2	3.6	0.9	5.6
P	19.8	4.7	31.1	12.0	7.1	18.9	5.3	2.8	11.1
Ca	< 0.1			< 0.1			< 0.1		
Sc	0.2	0.1	0.3	0.1	< 0.1	0.1	< 0.1		
Ti	0.1	< 0.1	0.2	< 0.1			< 0.1		
V	19.6	13.4	28.0	6.1	3.7	7.9	3.4	1.7	4.7
Cr	n.d.			n.d.			n.d.		
Mn	46.0	13.4	64.1	< 0.1			< 0.1		
Fe	< 0.1			< 0.1			< 0.1		
Co	7.3	0.1	15.4	0.4	< 0.1	2.2	0.1	< 0.1	0.2
Ni	5.2	1.0	11.5	2.0	0.6	4.5	0.3	0.3	0.3
Cu	0.6	0.1	1.1	1.5	0.2	6.3	< 0.1		
Zn	3.4	0.9	8.9	5.9	4.2	7.6	< 0.1		
Sr	40.0	2.2	76.3	8.9	1.0	18.9	< 0.1		
Cd	4.8	0.1	15.8	18.1	10.1	29.9	0.9	< 0.1	2.8
Ba	3.4	2.0	5.1	0.6	0.5	0.9	0.6	0.4	1.0
Pb	< 0.1			< 0.1			< 0.1		

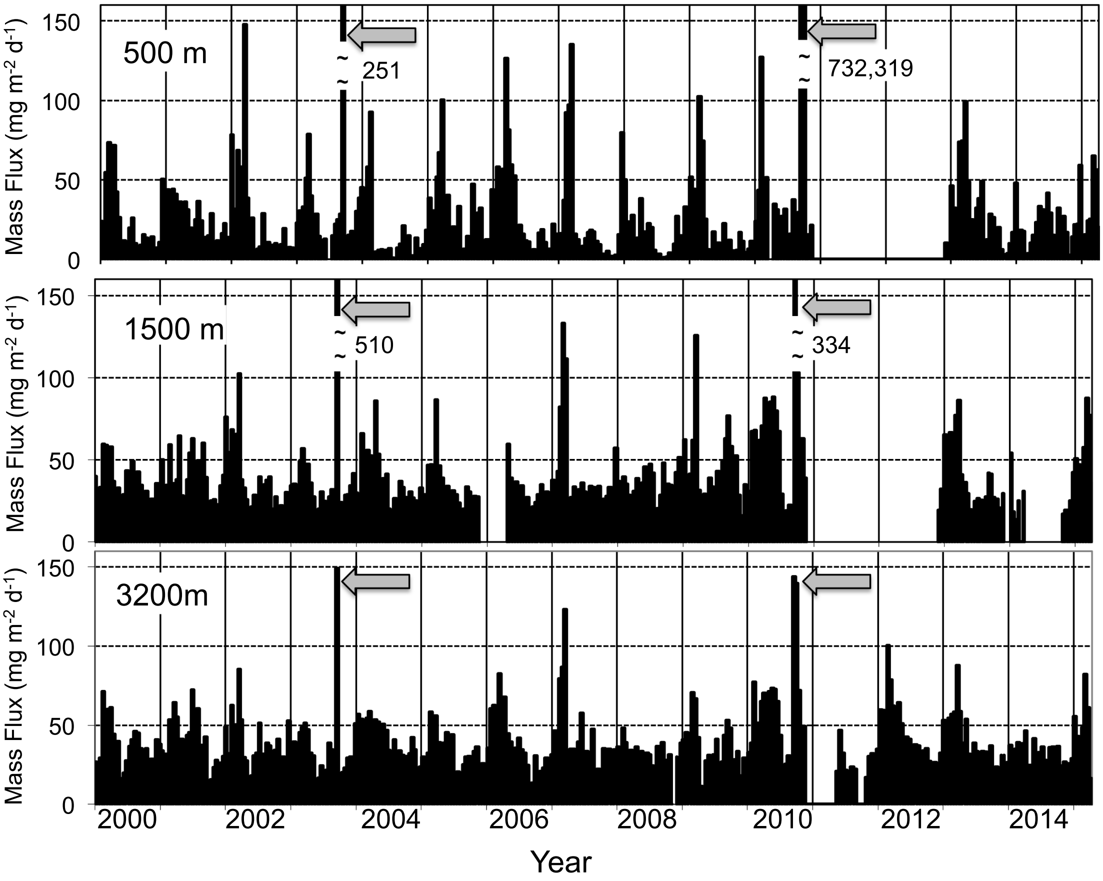

Fig. 1. Mass flux at the Oceanic Flux Program (OFP) site, shown for the time period corresponding to elemental data presented in this paper. The arrows indicate plumes of Bermuda platform sediments that were resuspended by Hurricanes Fabian (Cat 3, Sep 2003) and Igor (Cat 1, Sep 2010) and advected to the OFP site.

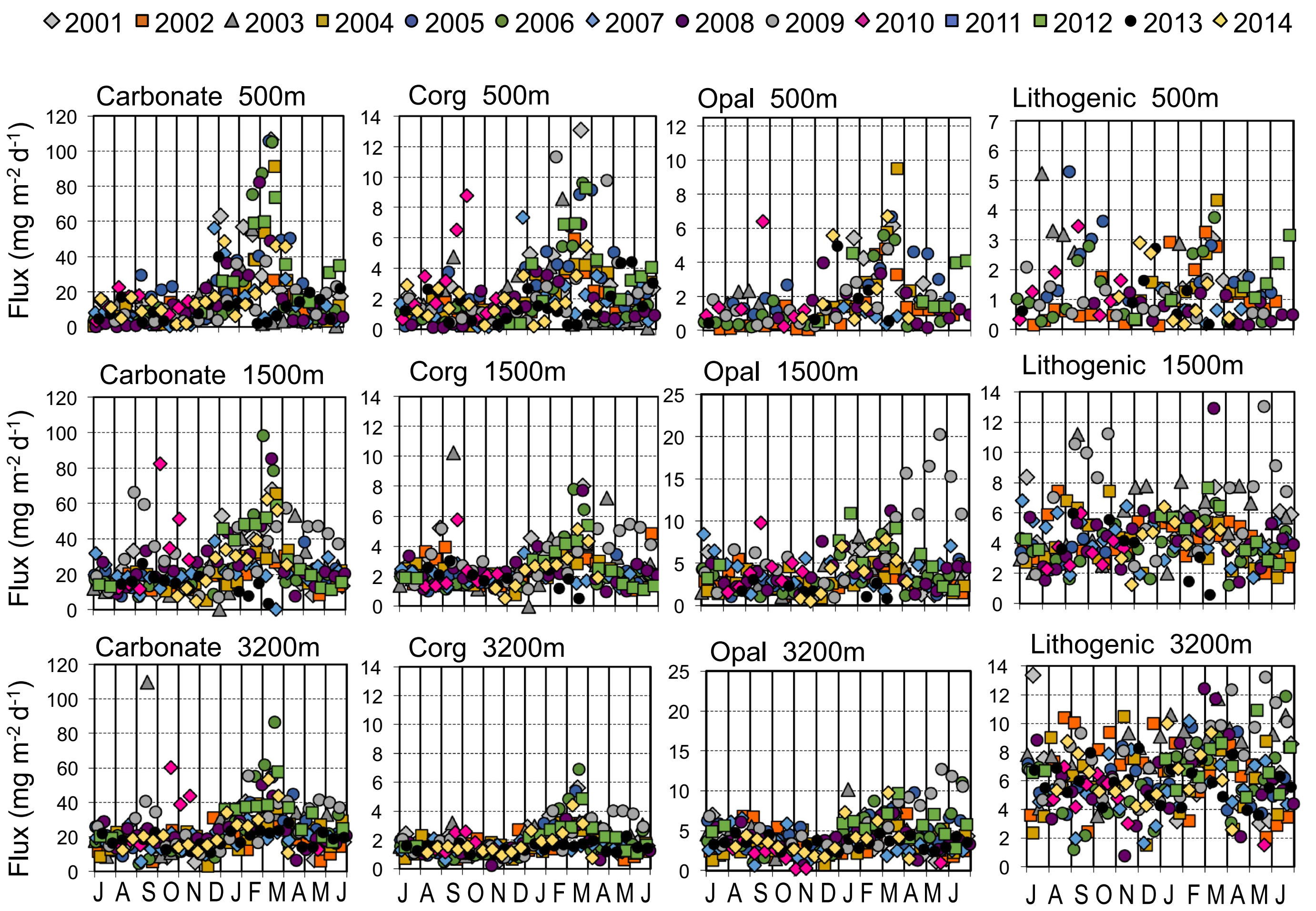

Fig. 2. Seasonal variation in fluxes of carbonate, organic carbon, opal and lithogenic material at the three trap depths. Lithogenic material is estimated from total Si and Al data using the average clay composition in deep sea sediments (Li and Shoonmaker, 2003); opal is calculated by difference (see Section 3.3.1). The fluxes are plotted July–July to better display the late winter–spring annual flux maximum. The years correspond to the year of the July start date (i.e. the symbol for 2001 denotes July 2001–June 2002). The y-axis is scaled to show the general seasonal trends and so may differ between trap depths (extreme fluxes associated with the Hurricanes Fabian (2003) and Igor (2010) sediment plumes are off scale).

suspended particles become incorporated into the flux via particle aggregation facilitated by zooplankton grazing activities, adhesion onto the sticky surfaces of amorphous aggregates such as transparent exopolymer particles (TEP) (e.g. Passow, 2002), and particle coagulation (e.g. Burd, 2013 and references therein).

The export of biogenic particles and other associated materials out of the surface waters, either via particle settling or mixing, transfers nutrient and particle-reactive elements to depth and efficiently cleanse the upper ocean of accumulated materials. While the export of materials to depth removes nutrient elements from surface waters, limiting plankton productivity, it provides the main food that supports deep water ecosystems (e.g. Dall'Olmo et al., 2016 and references therein).

Only a small fraction of the surface export flux is carried by rapidly sinking particles and efficiently transferred to the seafloor. Most of the material exported out of the surface waters is subjected to myriad particle recycling processes within the mesopelagic and bathypelagic zones before it eventually makes its way to the seafloor. Macrozooplankton grazing on particles results in repeated cycles of particle fragmentation and aggregation. Gelatinous filter-feeding zooplankton accumulate dissolved and particulate materials onto mucous feeding nets, which are then discarded to become part of the sinking flux. Passage of material through the gut environment provides recurring opportunities for elements to desorb, bioaccumulate, form organic-metal complexes, or be repackaged into fecal pellets. Microbial decomposition of biogenic materials leads to solubilization of elements and their release into the water column in dissolved, colloidal or suspended form (Fisher and Wente, 1993; Lee and Fisher, 1992; Reinfelder et al., 1993). Authigenic minerals such as barite precipitate within particle microenvironments created as organic matter decomposes (Bishop, 1988). Authigenic Mn-Fe oxyhydroxides (hereafter “Mn oxides”) precipitate on particle surfaces by bacterially-mediated redox reactions which also scavenge other redox sensitive elements from the water column via co-precipitation and/or adsorption (e.g. Statham et al., 2005; Moffett and Ho, 1996; Yao and Millero, 1996; Pohl and Hennings, 1999).

Thus, the deep particle flux can be considered as the sum of two

Table 2
Summary statistics of elemental fluxes (μg m^{-2} d^{-1}) at the three trap depths. Sediment plumes that were collected during Hurricanes Fabian (Sep 2003) and Igor (Sep 2010) are not included in statistics. Q1 - 25% quartile, Q3 - 75% quartile.

		Depth		
		500 m	1500 m	3200 m
Mg	Mean	118	224	236
	(Min, max)	(10.1, 744)	(28, 947)	(21, 905)
	Median	73	197	217
	(Q1, Q3)	(44, 140)	(136, 271)	(166, 291)
	Q-range	131%	69%	57%
Al	Mean	108	372	535
	(Min, max)	(10.9, 444)	(50, 1097)	(65, 1122)
	Median	86	349	526
	(Q1, Q3)	(45, 136)	(252, 453)	(407, 657)
	Q-range	107%	58%	48%
Si	Mean	1095	2714	3325
	(Min, max)	(74, 5046)	(505, 11,704)	(490, 8609)
	Median	847	2355	3081
	(Q1, Q3)	(456, 1460)	(1743, 3283)	(2430, 4064)
	Q-range	119%	65%	53%
P	Mean	208	70	36
	(Min, max)	(8.69, 1027)	(18, 325)	(8, 174)
	Median	187	62	29
	(Q1, Q3)	(122, 267)	(41, 78)	(22, 44)
	Q-range	77%	59%	76%
Ca	Mean	8353	10,060	9225
	(Min, max)	(196, 59,404)	(1491, 39,749)	(1027, 31,187)
	Median	5018	8441	8074
	(Q1, Q3)	(2430, 10,829)	(6110, 11,850)	(6268, 10,995)
	Q-range	167%	68%	59%
Sc	Mean	0.017	0.05	0.07
	(Min, max)	(0.002, 0.132)	(0.01, 0.18)	(0.01, 0.16)
	Median	0.013	0.05	0.07
	(Q1, Q3)	(0.006, 0.024)	(0.04, 0.06)	(0.06, 0.09)
	Q-range	138%	54%	47%
Ti	Mean	5.1	16.2	22.7
	(Min, max)	(0.1, 23.6)	(2.3, 63.1)	(2.8, 48.3)
	Median	3.7	14.6	22.0
	(Q1, Q3)	(2.0, 6.5)	(11.1, 19.8)	(16.3, 28.2)
	Q-range	124%	60%	54%
V	Mean	0.22	0.74	1.12
	(Min, max)	(0.01, 1.46)	(0.10, 2.77)	(0.13, 2.45)
	Median	0.14	0.68	1.11
	(Q1, Q3)	(0.08, 0.26)	(0.49, 0.91)	(0.83, 1.28)
	Q-range	134%	61%	49%
Cr	Mean	0.39	0.45	0.59
	(Min, max)	(0.03, 2.99)	(0.06, 1.34)	(0.09, 1.41)
	Median	0.22	0.41	0.57
	(Q1, Q3)	(0.10, 0.43)	(0.30, 0.55)	(0.42, 0.73)
	Q-range	150%	60%	54%
Mn	Mean	2.5	30.5	38.6
	(Min, max)	(0.2, 19.7)	(4.6, 88.8)	(5.0, 83.6)
	Median	1.1	29.0	38.2
	(Q1, Q3)	(0.6, 2.8)	(21.0, 38.5)	(29.3, 47.5)
	Q-range	196%	60%	48%
Fe	Mean	74	221	326
	(Min, max)	(2.0, 447)	(30, 705)	(41, 686)
	Median	56	208	324
	(Q1, Q3)	(30.1, 101)	(153, 271)	(245, 400)
	Q-range	126%	57%	48%
Co	Mean	0.09	0.36	0.42
	(Min, max)	(0.01, 0.42)	(0.05, 0.95)	(0.06, 0.86)
	Median	0.06	0.36	0.41
	(Q1, Q3)	(0.03, 0.12)	(0.27, 0.45)	(0.32, 0.51)
	Q-range	150%	50%	48%
Ni	Mean	0.74	1.29	1.37
	(Min, max)	(0.06, 3.84)	(0.29, 4.56)	(0.18, 3.64)
	Median	0.50	1.12	1.26
	(Q1, Q3)	(0.33, 1.05)	(0.80, 1.57)	(0.98, 1.67)
	Q-range	145%	70%	55%
Cu	Mean	1.16	2.16	2.77
	(Min, max)	(0.13, 5.20)	(0.31, 7.44)	(0.36, 6.42)
	Median	0.89	1.97	2.71
	(Q1, Q3)	(0.42, 1.50)	(1.50, 2.54)	(2.14, 3.32)
	Q-range	122%	53%	44%
Zn	Mean	2.91	2.56	1.96
	(Min, max)	(0.02, 22.83)	(0.31, 11.25)	(0.11, 10.71)
	Median	2.15	2.13	1.58
	(Q1, Q3)	(1.39, 3.40)	(1.49, 3.29)	(1.12, 2.36)
	Q-range	93%	85%	79%
Sr	Mean	50	69	64
	(Min, max)	(2, 298)	(9, 271)	(6, 230)
	Median	33	59	57
	(Q1, Q3)	(16, 61)	(45, 78)	(44, 76)
	Q-range	135%	56%	56%
Cd	Mean	0.095	0.033	0.018
	(Min, max)	(0.002, 0.829)	(0.004, 0.203)	(0.001, 0.120)
	Median	0.051	0.024	0.015
	(Q1, Q3)	(0.023, 0.113)	(0.016, 0.040)	(0.010, 0.023)
	Q-range	175%	100%	87%
Ba	Mean	10.9	28.8	27.7
	(Min, max)	(0.4, 53.4)	(3.6, 90.9)	(3.4, 60.9)
	Median	7.7	27.0	26.7
	(Q1, Q3)	(4.1, 13.8)	(21.3, 35.0)	(20.4, 34.0)
	Q-range	127%	51%	51%
Pb	Mean	1.3	2.8	3.4
	(Min, max)	(0.1, 8.0)	(0.4, 10.4)	(0.8, 11.4)
	Median	0.9	2.4	3.0
	(Q1, Q3)	(0.5, 1.4)	(1.6, 3.4)	(2.2, 4.0)
	Q-range	107%	73%	60%

components. First, there is an "extrinsic" flux component that is sourced from and closely temporally coupled with overlying plankton production and surface export and efficiently transferred to depth. Second, there is an "intrinsic" flux component that is generated within the water column by processes including suspended particle aggregation, de novo large particle production by zooplankton, chemical scavenging and authigenic mineral precipitation.

While eventually particle-reactive elements arrive at the seafloor, this may not occur until significant lateral advection has taken place. In particular, dissolved and suspended materials from ocean margins can be advected thousands of kilometers by ocean currents before removal by intrinsic flux generation processes within the water column.

Despite the central role of particle flux processes on the cycling and distributions of many elements within the ocean, there have been few investigations of the detailed elemental composition of the particle flux. Kuss and Kremling (1999a) and Kuss et al. (2010) analyzed the elemental flux in the deep northeast Atlantic at three Kiel sediment trap mooring sites (33° N, 47° N and 54° N) along the 20° W transect over the time period from 1992 to 1996. Stern et al. (2017) made additional measurements of Ba and lithogenic element fluxes at 2000 m depth at the 33° N site over the time period from 2002 to 2008. Shorter studies of elemental fluxes at coastal sites have also been conducted in the Baltic Sea (Pohl et al., 2004), the Cariaco Basin (Calvert et al., 2015) and the polynya area of Prydz Bay, Antarctica (Sun et al., 2016).

The Oceanic Flux Program (OFP) time-series of particle flux in the northern Sargasso Sea is the longest time-series of its kind. Jickells et al. (1984, 1990) conducted limited analyses of elemental fluxes in the deep 3200 m trap and showed that the elemental flux has a seasonality corresponding to the annual cycle of overlying primary production.

Beginning in the late 1990s, we modified the OFP mooring design and sample collection and processing methods to obtain flux samples of highest purity for trace element (and organic) analyses. Huang and Conte (2009) presented data on elemental fluxes in the three OFP traps (500 m, 1500 m, 3200 m) covering the period between 2001 and 2005, and provided an initial assessment of flux carrier phases.

In this paper we build upon the Huang and Conte (2009) study, extending the time-series an additional ten years to 2015. We summarize data from 668 individual sediment trap samples (137 at 500 m depth, 224 at 1500 m depth and 308 at 3200 m depth) and provide a uniquely detailed and comprehensive assessment of elemental fluxes in the deep waters of the western North Atlantic gyre. The focus here is on the seasonal cycle in elemental fluxes and flux composition, and on the depth evolution of flux composition and elemental associations with flux carrier phases. Non-seasonal drivers of deep flux temporal variability will be described in subsequent papers.

2. Study area

The Bermuda Time-Series Site is located in the northern Sargasso Sea within the Gulf Stream recirculation gyre (Joyce and Robbins, 1996; Talley, 1996). The site is one of the most extensively studied open ocean regions in the world and hosts several ongoing, complementary time-series: the Hydrostation S time-series (since 1954) of water column hydrographic properties (Michaels and Knap, 1996; Steinberg et al., 2001; Phillips and Joyce, 2007), the Oceanic Flux Program (OFP) time-series (since 1978) of the deep ocean particle flux (Deuser, 1986; Conte et al., 2001; Conte and Weber, 2014), the Bermuda Atlantic Time-Series study (BATS, since 1988) time-series of upper ocean biogeochemistry (Michaels and Knap, 1996; Steinberg et al., 2001; Lomas et al., 2013), and from 1994 to 2007, the Bermuda Testbed Mooring (BTM) (Dickey et al., 2001). The Tudor Hill tower observatory on Bermuda has been the site of multiple atmospheric campaigns, including studies on long-range atmospheric transport and deposition of Saharan dust and pollutants (e.g. Huang et al., 1999; Arimoto et al., 2003; Sedwick et al., 2005). Together with remote sensing, these time-

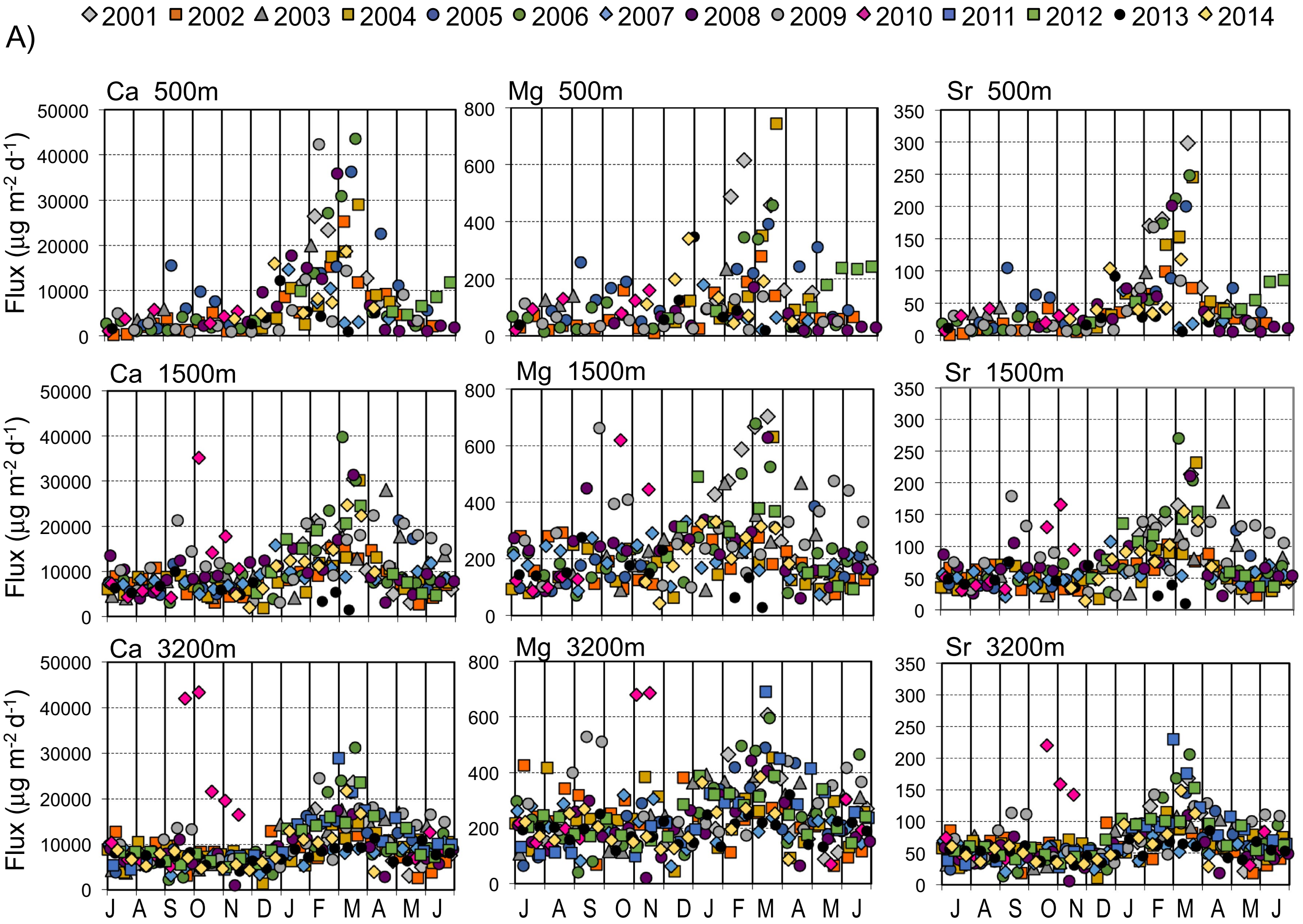

Fig. 3. Seasonal variation in elemental fluxes at the three trap depths. The fluxes are plotted July–July to better display the late winter–spring annual flux maximum. The years correspond to the year of the July start date (i.e. the symbol for 2001 denotes July 2001–June 2002). The y-axis is scaled to show the general seasonal trends and so may differ between trap depths (extreme fluxes associated with the Hurricanes Fabian (2003) and Igor (2010) sediment plumes are off scale). (a) Carbonate elements (b) nutrient elements (c) lithogenic elements (d–f) authigenic and mixed source elements.

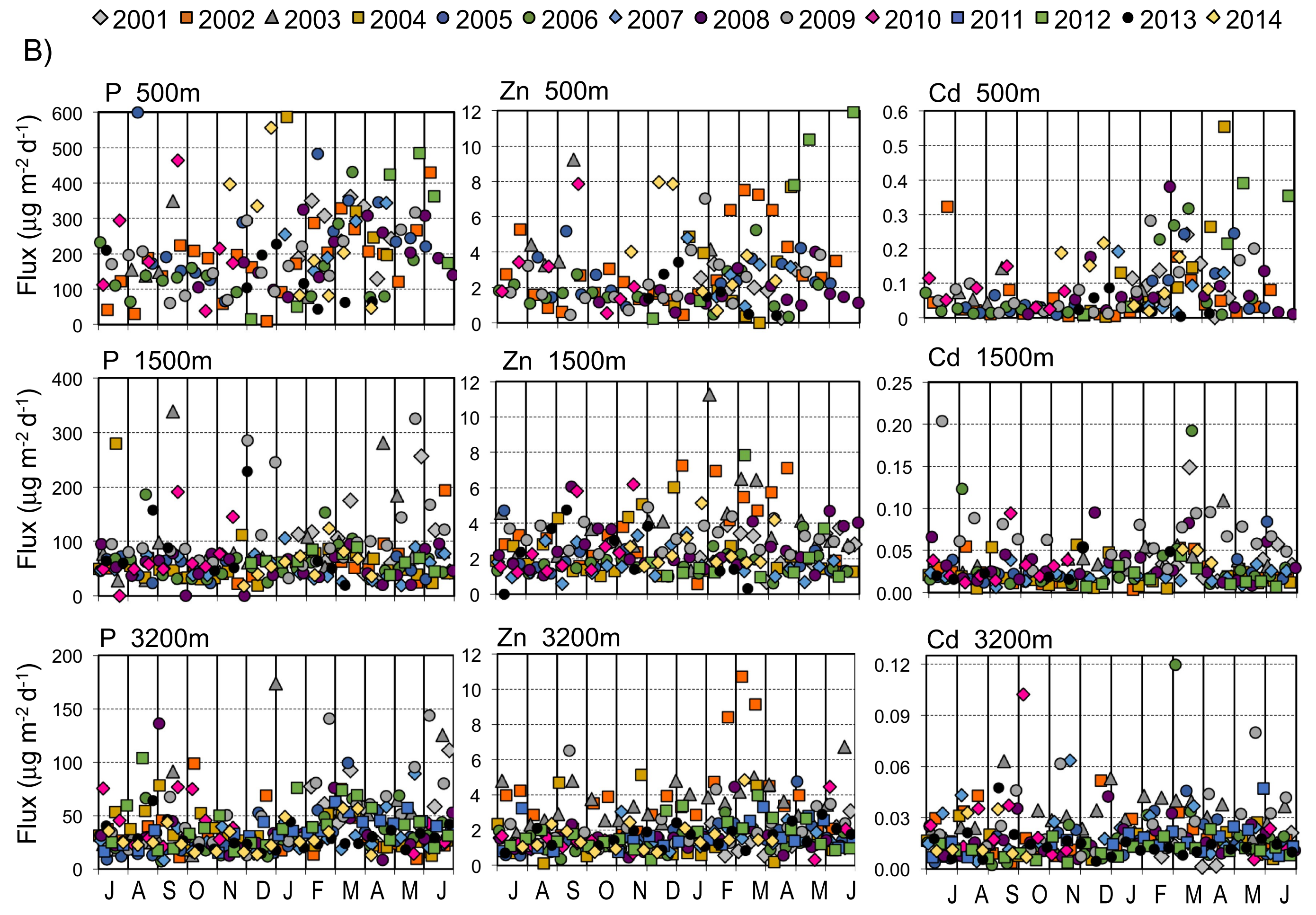

Fig. 3. (*continued*)

series provide a uniquely detailed view of the complex interactions among physics, chemistry and biology in the oligotrophic western North Atlantic gyre.

The seasonal cycle in upper ocean biogeochemistry and primary productivity has been previously described (Michaels and Knap, 1996, Steinberg et al., 2001, Lomas et al., 2013). The mixed layer reaches a maximum depth of 250–300 m in January to early February. With the onset of seasonal stratification in late February–early March, a short spring bloom develops and phytoplankton biomass and particulate organic carbon (POC) and nitrogen reach maximum concentrations. As seasonal stratification intensifies, a shallow, nutrient-depleted surface mixed layer develops with a subsurface chlorophyll maximum at the base of the mixed layer. Strong thermal stratification in summer and autumn results in low vertical mixing that limits nutrient availability and primary production. Seasonal cooling in late autumn leads to gradual mixed layer deepening, renewed nutrient entrainment into the euphotic zone and increased productivity.

There is significant inter-annual variability in the seasonal cycle, as well as episodic and sub-seasonal variability in upper ocean biogeochemistry and surface export fluxes (Lomas et al., 2013) as well as in the deep water particle flux (Conte et al., 1998, 2001, 2003). Much of the variability on time-scales of weeks to months arises due to short-term physical forcing of the surface waters and nutrient upwelling that is associated with the passage of synoptic-scale weather systems and mesoscale features such as eddies (e.g. McGillicuddy et al., 1998; McNeil et al., 1999; Dickey et al., 2001; Conte et al., 2003; Krause et al., 2010; Shatova et al., 2012).

3. Methods

3.1. Sampling methods

The OFP mooring is located southeast of Bermuda (31°50′ N, 64°10′ W) in 4500 m water depth. McLane Parflux sediment traps (0.5 m^2 surface aperture area; McLane Labs, Falmouth, MA, USA) are deployed at 500 m, 1500 m and 3200 m depths. The OFP mooring and sample collection protocols are detailed in Conte et al. (2001). Mooring hardware and operational protocols were updated in the mid-1990s with 316 stainless chain and hardware. Epoxy coated mooring terminations are used in the proximity of traps to minimize organic and trace element contamination during sampling. The OFP traps are not immune from swimmers (e.g. fish, amphipods), which can seriously compromise sample integrity. Although problems are not as severe as in more productive areas, it has been necessary to install a high purity titanium

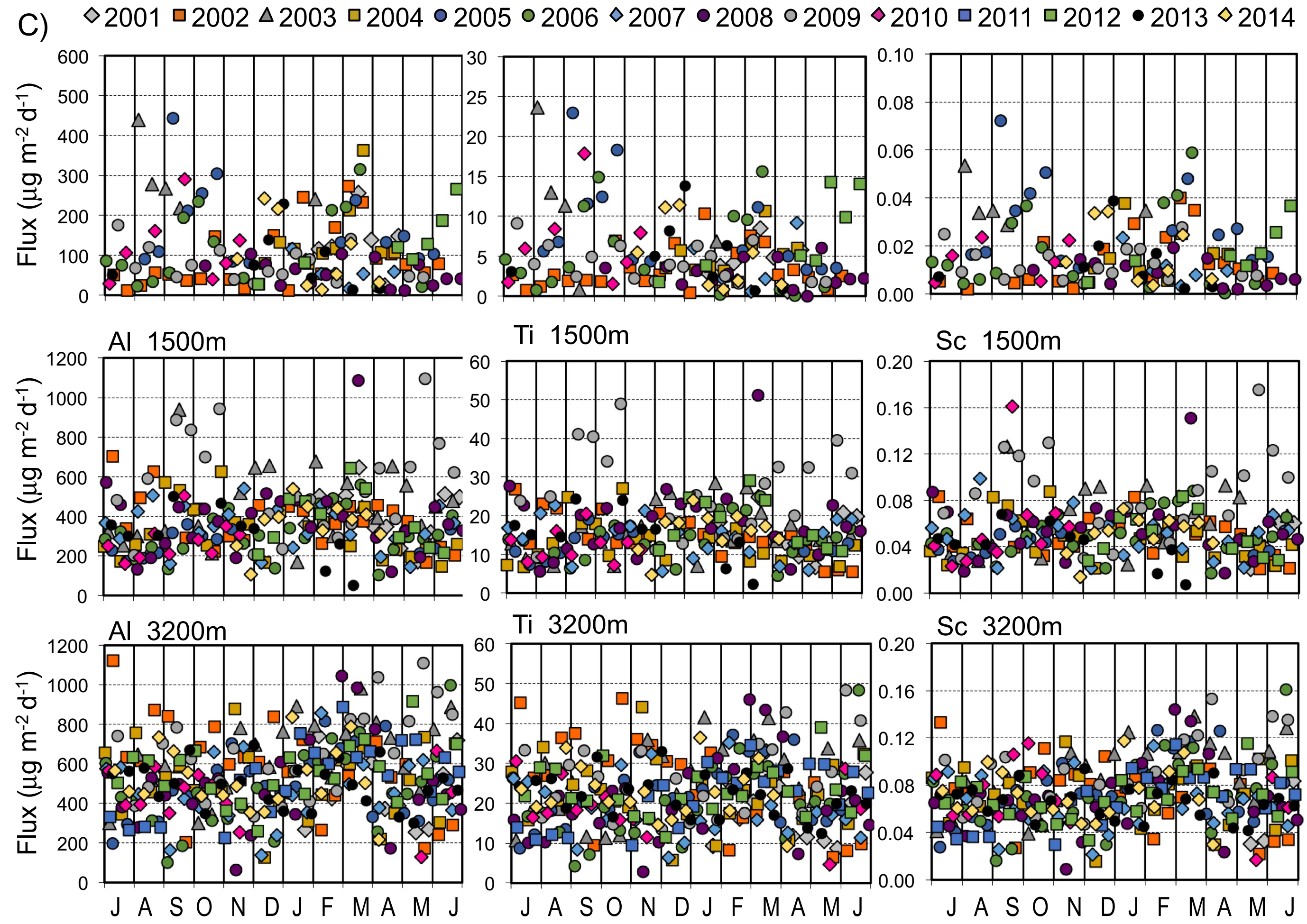

Fig. 3. (*continued*)

screen (Grade 1 titanium, 1.25 cm mesh opening, 16 mm wire diameter) on the 500 m trap honeycomb to prevent fish and large swimmers from entering the trap funnel. (The screen was first installed in July 2004.) Swimmers are only rarely a problem in the 1500 m and 3200 m traps so no screens are installed at these depths.

The trap carousel is carefully cleaned and rinsed with deionized water just prior to loading the sample bottles. The polyethylene sample bottles are trace metal cleaned and leached with deionized water during storage, using procedures described in Conte et al. (2001) and Huang et al. (2007). Prior to deployment, the bottles are filled under a laminar flow hood with a trace metal clean brine (~40 ppt) poisoned with ultra-purity mercuric chloride ($200\,\mathrm{mg\,l^{-1}}$) to arrest bacterial activity. The brine is made from unfiltered seawater collected at 3000 m depth using trace-metal clean Go-Flo bottles on clean Kevlar line. The seawater is concentrated to 40 ppt by freezing in a trace-element clean LDPE carboy dedicated for this purpose. To assess for contamination during brine preparation and/or sample collection, process and deployment blanks are collected on each deployment.

3.2. Analytical methods

3.2.1. Sample processing

OFP sample processing protocols used for elemental analysis have been previously described (Huang and Conte, 2009). All sample processing is conducted under a laminar flow hood using trace metal cleaned plastic and Teflon ware. Before sample processing, an aliquot of supernatant is removed for dissolved analyses (P, Si and for select samples multi-elemental determination by ICPMS). The > 1 mm sized fraction of the trap material (which interferes with quantitative sample splitting) is gently removed by screening before splitting. The < 1.0 mm material is split (± 3% reproducibility) using a McLane 10-place splitter equipped with a custom Teflon coated tray and spigots. Sample supernatant brine is used for rinsing steps. One split (10% of the sample) is collected in a trace metal cleaned LDPE centrifuge tube for elemental analyses. This split is centrifuged, briefly rinsed with 18 Ω□ MilliQ water to remove the brine solution and then freeze-dried. Three splits are removed for organic analyses and six splits (60% of the total sample) are combined and further processed, as described in Conte et al. (2001), for bulk compositional analyses.

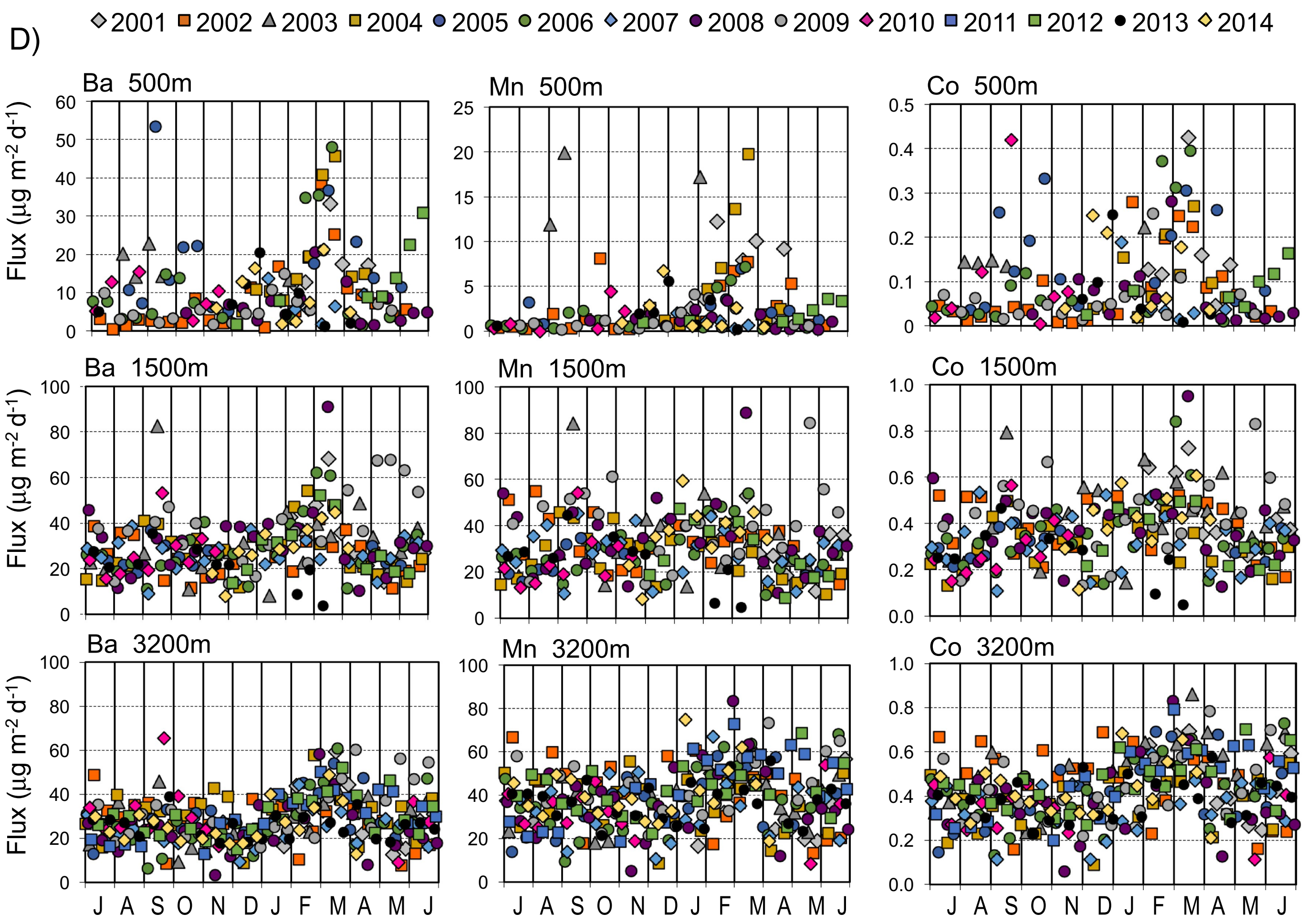

Fig. 3. (*continued*)

3.2.2. *Elemental analysis*

Elements are quantified using a fusion ICPMS method developed in our lab for multi-elemental analysis of small (mg) quantities of sediment trap material (Huang et al., 2007; Huang and Conte, 2009). Briefly, the dried < 1 mm sediment trap material is processed by fusion with high purity lithium metaborate ($LiBO_2$) flux at 1000 °C in a dedicated combustion furnace. Prior their use for sample analyses, Pt crucibles are first repeatedly leached by conducting multiple fusion cycles to reduce Pb blanks, which arise from impurities in the Au in the crucibles. The sample to $LiBO_2$ flux ratio for fusion is approximately 1:2.5. The fused sample bead is subsequently dissolved in 1 M HNO_3 for ICPMS analysis. From 2000 to 2004, we used 1–2 mg of flux material for analysis, but in 2005 we increased this to ~6 mg to reduce analytical variability associated with particle heterogeneity. Blank analyses of the $LiBO_2$ flux are run with each sample set to assess contamination.

The final sample solution was analyzed on a high resolution Finnigan Element 2 ICPMS. A matrix-matching multi-element external standard solution was used for determination of the trace element concentrations.

To assess analytical reproducibility and uncertainty over the analysis period (2004–2015) and to allow for data intercalibration, we ran the certified standard PACS-2 (National Research Council of Canada) with each fusion group, and also periodically ran well-characterized working standards of OFP sediment trap material. (These are bimonthly samples collected early in the time-series when a larger trap was employed.) The average coefficients of variation (CV) for element measurements in PACS-2 standards analyzed within each ICPMS analytical session, which includes fusion group variability as well as ICPMS variability were: Mg (6.2%), Al (5.8%), Si (7.7%), P (8.2%), Ca (5.9%), Sc (7.1%), Ti (5.4%), V (6.0%), Cr (6.4%), Mn (5.8%), Fe (5.3%), Co (9.1%), Ni (19.9%), Cu (7.3%), Zn (11.4%), Sr (8.0%), Cd (15.4%), Ba (6.7%), and Pb (10.4%). The average coefficients of variation (CV) for the trap working standard SCIFF/OFP8/82 in five ICPMS sessions, with between 4 and 14 trap working standard analyses per session, were similar: Mg (5.7%), Al (6.9%), Si (7.3%), P (6.8%), Ca (5.9%), Sc (7.6%), Ti (6.8%), V (7.7%), Cr (ND), Mn (7.6%), Fe (7.6%), Co (14.0%), Ni (11.7%), Cu (15.8%), Zn (21.0%), Sr (9.3%), Cd (17.1%), Ba (10.6%), and Pb (30.2%). The high CV for Zn and Pb in the trap working standards arises from an intermittent crucible (Pb) and lab (Zn) contamination that was a problem in early analyses (c.f. Huang et al., 2007).

The overall CV for PACS-2 runs over the entire analysis period was approximately twice that observed within each ICPMS session. This indicated additional variability associated with the ICPMS analytical

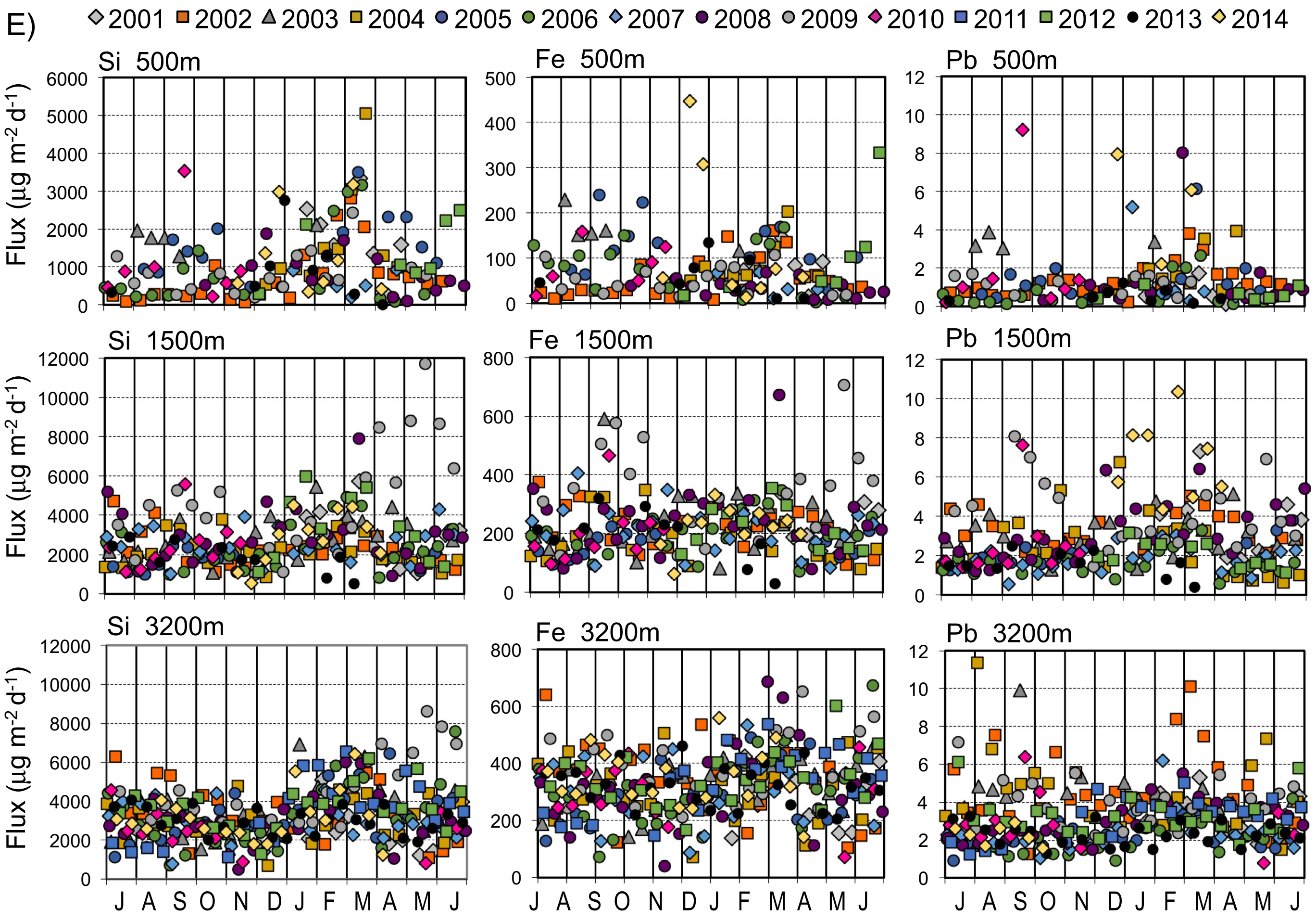

Fig. 3. (*continued*)

sessions, possibly resulting from slight differences in instrument tuning or other ICPMS setup conditions. Therefore, to intercalibrate the data, we normalized the raw ICPMS data using the average PACS-2 response (i.e. measured versus certified value) within that ICPMS analytical session. We used the PACS-2 standard as the basis for intercalibration rather than sediment trap working standards because PACS-2 replicates were routinely run whereas the OFP sediment trap working standards were run infrequently given the limited quantities and valuable of the trap material.

The P and Si data presented here include both the particulate fraction and the dissolved fraction in the supernatant resulting from dissolution of material in the trap cup during deployment. We measured P and Si in sample supernatants in duplicate using a LACHAT autoanalyzer (Lachat Instruments, Milwaukee WI), correcting for background concentrations in the brine blank of the corresponding deployment. The masses of P and Si in the supernatant were added to particulate mass determined by ICPMS to obtain total P and Si concentrations.

To assess dissolution losses of other elements, we analyzed the elemental concentrations in supernatants by ICPMS for a recovery set of samples spanning collection dates from Nov 2008 to April 2009. Excess elemental concentrations in the supernatant were determined by subtracting the brine blank for the deployment. The average percent dissolution of each element in the flux material post-collection is given in Table 1. At 3200 m depth, dissolution losses into the supernatant were < 1% for all elements except P (5.3%), Si (3.6%) and V (3.4%). At 1500 m, losses were higher and more variable, averaging between 1 and 5% for Ni and Cu, between 5 and 10% for Si, V, Zn and Sr and > 10% for P (12.7%) and Cd (18%). Losses at 500 m were significantly higher and even more variable, averaging between 1 and 5% for Zn, Cd and Ba, between 5 and 10% for Si, Co and Ni. Losses of P (20%), V (20%), Mn (46%) and Sr (40%) were significant. The higher losses of nutrient elements in the 500 and 1500 m traps likely reflect the greater solubility of these elements in labile organic phases, and possibly additional sources from swimmers in the 500 m trap. The high losses of Sr in the 500 m and 1500 m traps likely reflect the dissolution of the celestite ($SrSO_4$) tests of acantharia. The significant loss of Mn at 500 m depth, but not in the deeper flux suggests its association with a labile phase at mesopelagic depths. The reason for the high solubility of V in the 500 m trap is not clear, but possibly reflects a weak association with a more labile phase(s) in the mesopelagic. No seasonal trends were apparent in this limited dataset, although the more extensive LACHAT dataset for supernatant P concentration indicates greater P solubilization in the 500 m flux during high flux periods (data not shown), suggesting a

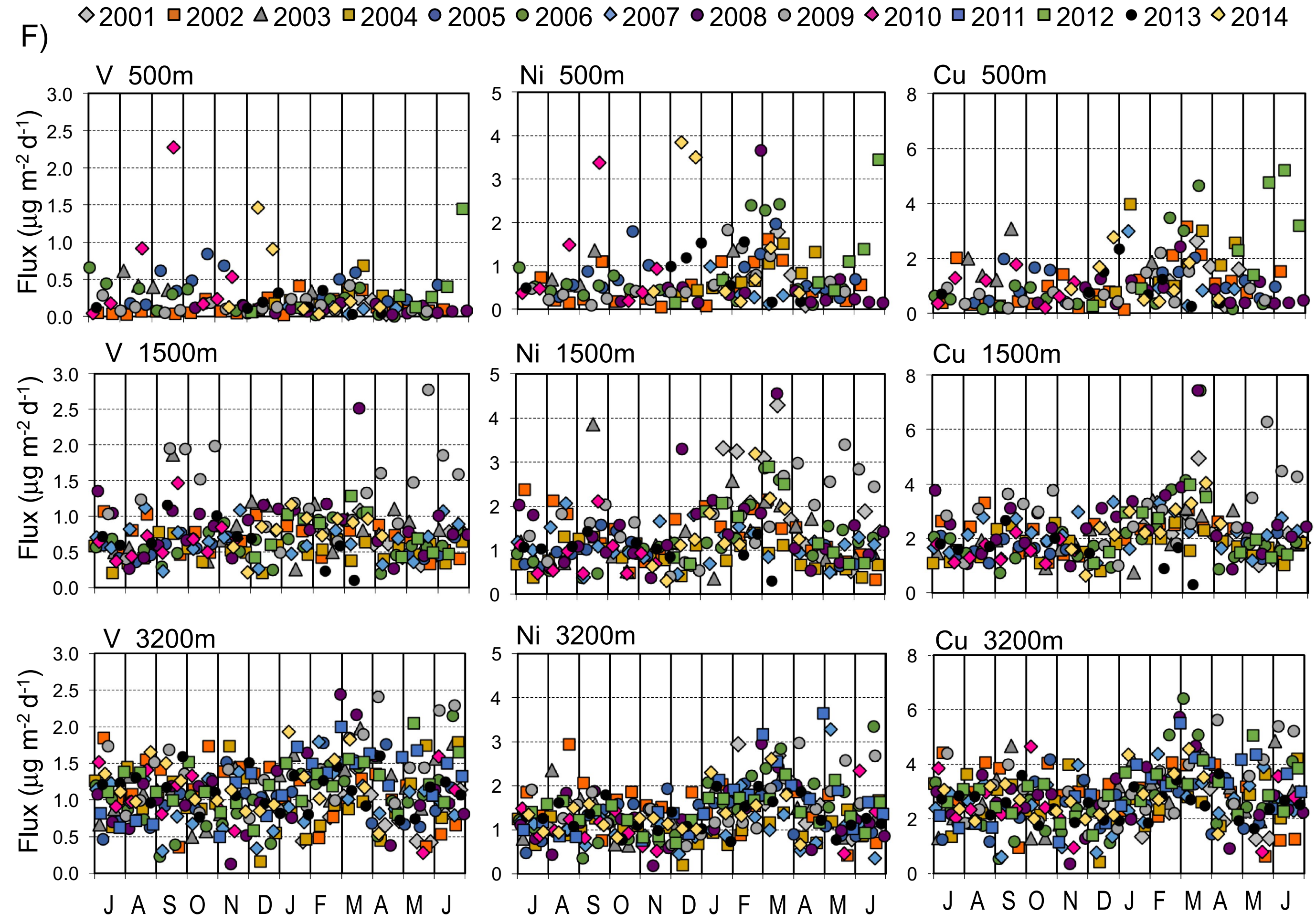

Fig. 3. (*continued*)

possible influence of organic matter lability. Because of the large sample variability in the supernatant ICPMS data, we did not apply any universal correction factor to correct for losses of these elements into the supernatant. Therefore, reported fluxes of V, Cd, Mn and Sr in the 500 m trap and Cd in the 1500 m trap should be considered minimum values. As noted above, the P and Si data reported here were corrected for post-collection dissolution losses.

We observed intermittent, but extreme, Cr contamination of the flux material in the 500 m trap (1–2 orders of magnitude higher than median concentrations) but rarely in the deeper traps. Cr data was excluded in the elemental database when concentrations were > 3× higher than the median. One possible source of Cr contamination is the Ti screen installed on the 500 m trap, but this seems unlikely as the Ti screen has only trace amounts of Cr and no obvious Ti co-contamination was observed. A more likely source of the contamination is the 316 stainless chain and hardware just above the trap, as stainless steel has a high Cr content (~18%). Microbes bioaccumulate Cr (e.g. Iyer et al., 2004). Microbial growth, which forms a slimy mucous coating on mooring surfaces, including stainless components, is far more prevalent at the 500 m depth and thus would be more likely to intermittently slough off from hardware above the trap and enter in sampling funnel. Despite the potential for Cr contamination, the Cr data show valuable trends and elemental associations so we have chosen to include these data here, noting this caveat.

3.2.3. *Bulk composition analyses*

Total carbonate was measured by closed system digestion with sulfuric acid using a Coulometrics Model 5011 carbon analyzer. For organic carbon and nitrogen analysis, dried sample material (2–3 mg) was first carefully decalcified with H_2SO_3 using a modification of the Verrado et al. (1990) method. The decalcified samples were analyzed in duplicate for carbon and nitrogen concentration and isotopic composition on a Europa ANCA-SL elemental analyzer - gas chromatograph preparation system attached to a continuous-flow Europa 20-20 gas source stable isotope ratio mass spectrometer. Certified reference materials and well-characterized working standards of sediment trap material and sediments are analyzed with each sample batch to ensure data inter-calibration. Data intercalibration is also routinely checked through repeat analyses of selected archived samples.

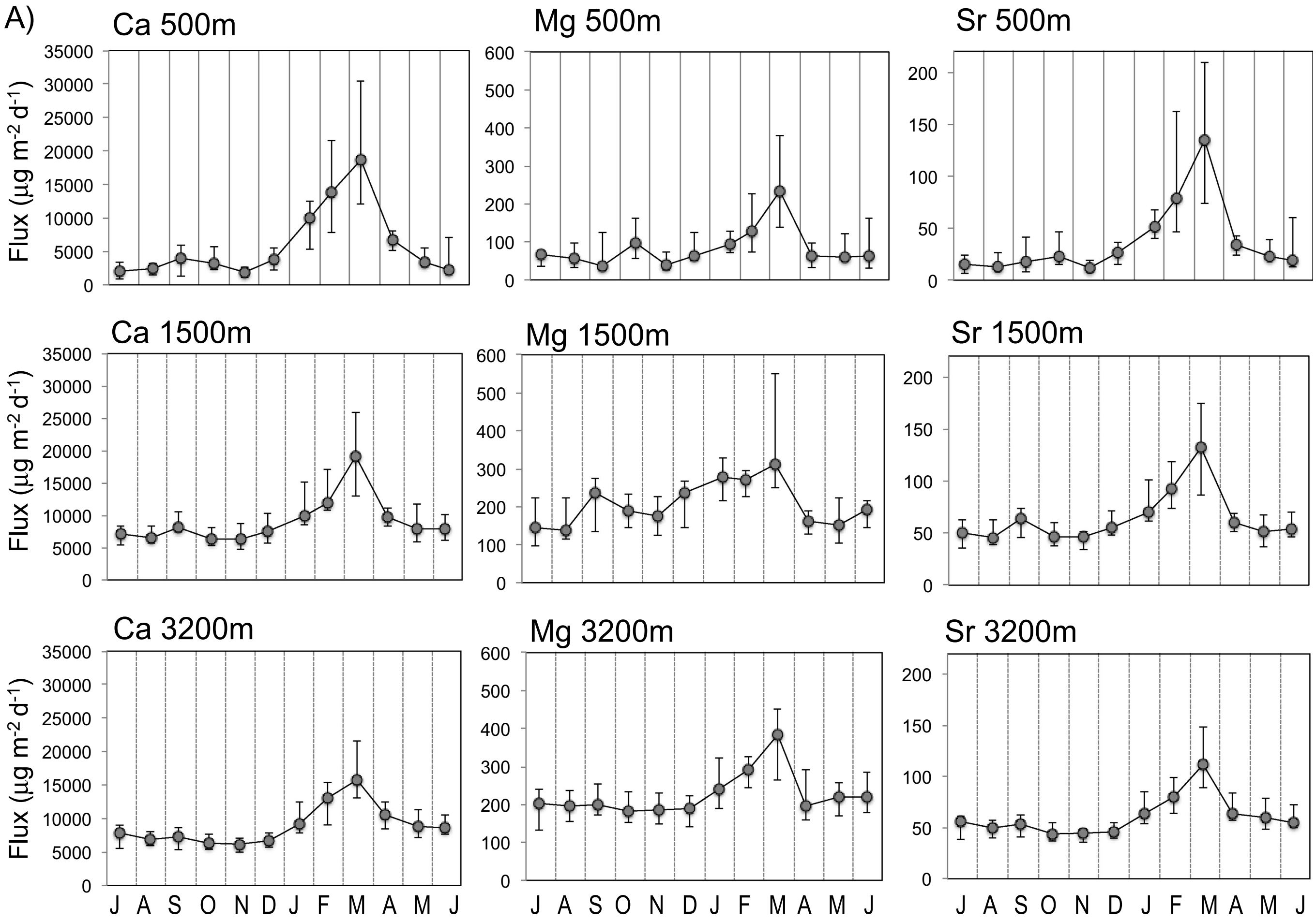

Fig. 4. Summary statistics of monthly elemental fluxes at the three trap depths. The fluxes are plotted July–July to better display the seasonal maximum. The y-axis is scaled to show the general seasonal trends and so may differ between depths. Plotted are the median fluxes and bars showing the range between 25% and 75% quartiles. (a) Carbonate elements (b) nutrient elements (c) lithogenic elements (d–f) authigenic and mixed source elements.

3.3. Data analysis

3.3.1. Lithogenic and opal contributions

Bulk lithogenic concentration was estimated from the Al concentration determined by ICPMS, assuming that the Al in the flux material was carried mainly by lithogenic particles and that Al concentration of the lithogenic flux particles is similar to that of pelagic clay sediments (8.4%, Li and Shoonmaker, 2003),

$$[Lithogenic] = \frac{[Al]}{0.084} \tag{1}$$

This assumption is supported by the dominance of clays in north Atlantic sediments (Biscaye, 1965), but may slightly overestimate the actual lithogenic fraction because dissolved Al can be scavenged by organic matter (e.g. Balistrieri et al., 1981) and also incorporated into opal (Dymond et al., 1997; Gehlen et al., 2002).

To estimate the lithogenic fraction of the total Si in the flux material, we assumed that the Si content of the lithogenic flux material approximates that of pelagic clay sediments (25% by weight, Li and Shoonmaker, 2003). The biogenic Si concentration was then estimated by subtracting the lithogenic Si from the total Si,

$$[Si_{bio}] = [Si_{total}] - [Si_{lith}] \tag{2}$$

We converted Si_{bio} to opal mass assuming the opal water content ($SiO_2 \cdot 0.4H_2O$) reported by Mortlock and Froelich (1989). Calculated opal is in good agreement with the opal data for a subset of 3200 m samples (reported in Deuser et al., 1995) that were previously analyzed using the opal dissolution method of Mortlock and Froelich (1989).

To validate the approach, we calculated the total sample mass, summing the carbonate, organic matter (estimated as CH_2O), opal, and lithogenic percentages. The calculated sample mass closely agrees with the sample mass that was measured gravimetrically. For 500 m samples the median percentage of calculated mass is 100% of the gravimetric mass (lower and upper quartiles of 95% and 104%), for 1500 m samples the median percentage is 101% (lower and upper quartiles of 99% and 104%), and for 3200 m samples the median percentage is 102% (lower and upper quartiles of 99% and 105%). Addition of authigenic barite and Mn oxide components would increase the calculated total mass by < 0.5% (see Section 4.4).

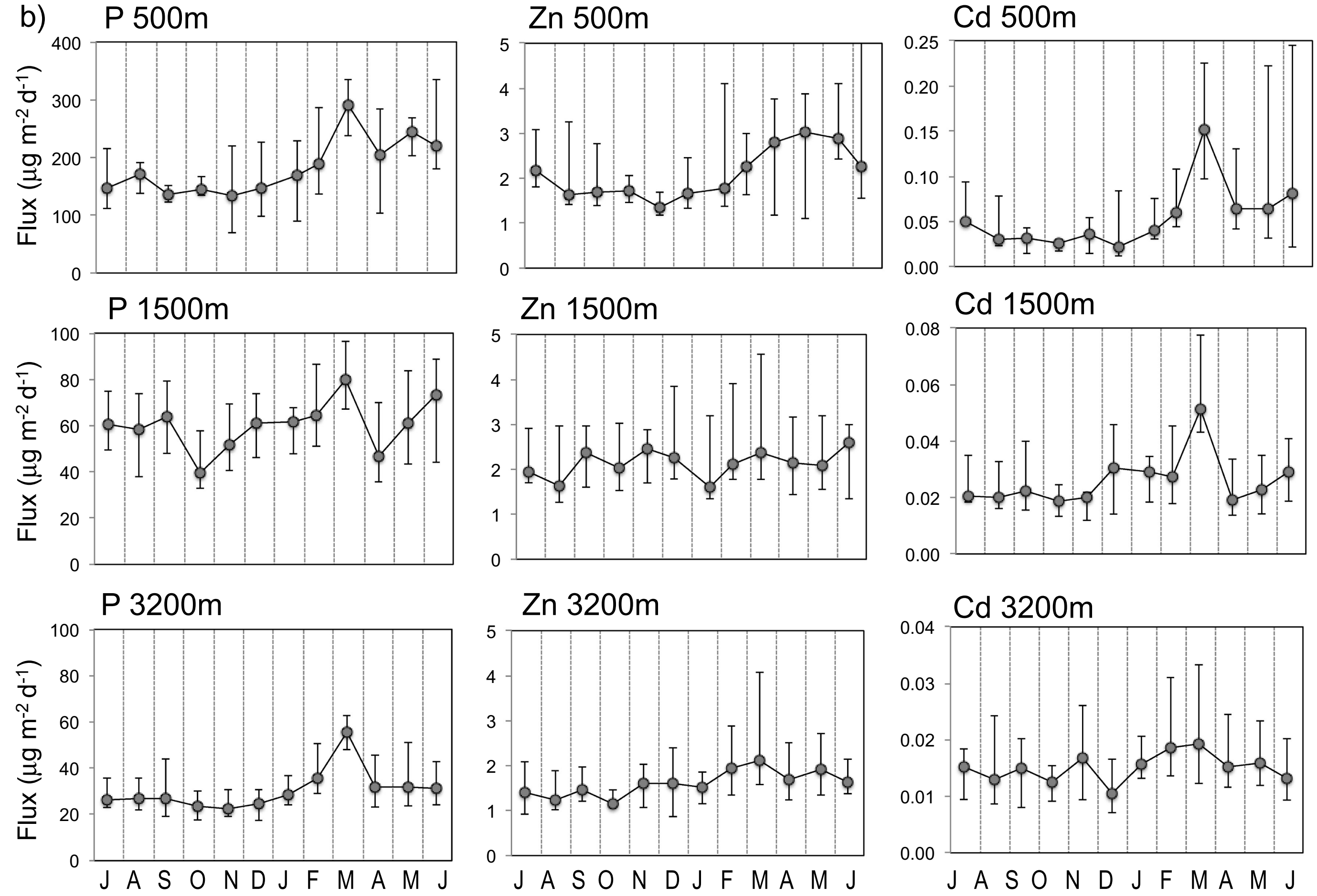

Fig. 4. (*continued*)

3.3.2. Enrichment factor and excess elemental concentrations

The enrichment factor (EF) for each element with respect to the average concentration of upper continental crust (UCC) was calculated by normalizing the data to Al,

$$EF = \frac{\frac{[X]}{[Al]}_{sample}}{\frac{[X]}{[Al]}_{UCC}} \tag{3}$$

using the Al-normalized element concentrations of UCC reported in Rudnick and Gao (2003). We used the UCC composition as currently there are no direct data on the bulk elemental composition of lithogenic material in the water column and the elemental composition of the pelagic sediments (Li and Shoonmaker, 2003) includes authigenic as well as lithogenic phases.

The "excess" elemental concentration ($[X]_{xs}$), i.e. the concentration that is unsupported by the lithogenic fraction, was calculated as

$$[X]_{xs} = [X]_{total} - [X]_{lith} \tag{4}$$

where $[X]_{lith}$ is the Al normalized concentration of element X in the upper continental crust reported in Rudnick and Gao (2003),

$$[X]_{lith} = [Al]_{total} \times \frac{[X]_{UCC}}{[Al]_{UCC}} \tag{5}$$

4. Results

4.1. Mass flux and bulk components

4.1.1. Mass flux

Fig. 1 shows the total mass flux at the OFP site for the period corresponding to the elemental data presented in this paper. (Gaps in the data between 2010 and 2011 at 3200 m depth, and between 2010 and 2012 at 500 m and 1500 m depths resulted from loss of the mooring, other gaps at 1500 m depth resulted from trap failure.) The OFP traps captured two plumes of detrital carbonate sediments from the Bermuda platform that were resuspended during passages of Hurricanes Fabian (Category 3, Sep 2003) and Igor (Category 1, Sep 2010) and advected offshore. As these extreme events are atypical, they are excluded from results and statistics presented here.

The main features of the mass flux over this time interval are similar to those described for the earlier 1978–1998 time interval (Conte et al., 2001). A clear seasonal cycle is observed in the mass flux that

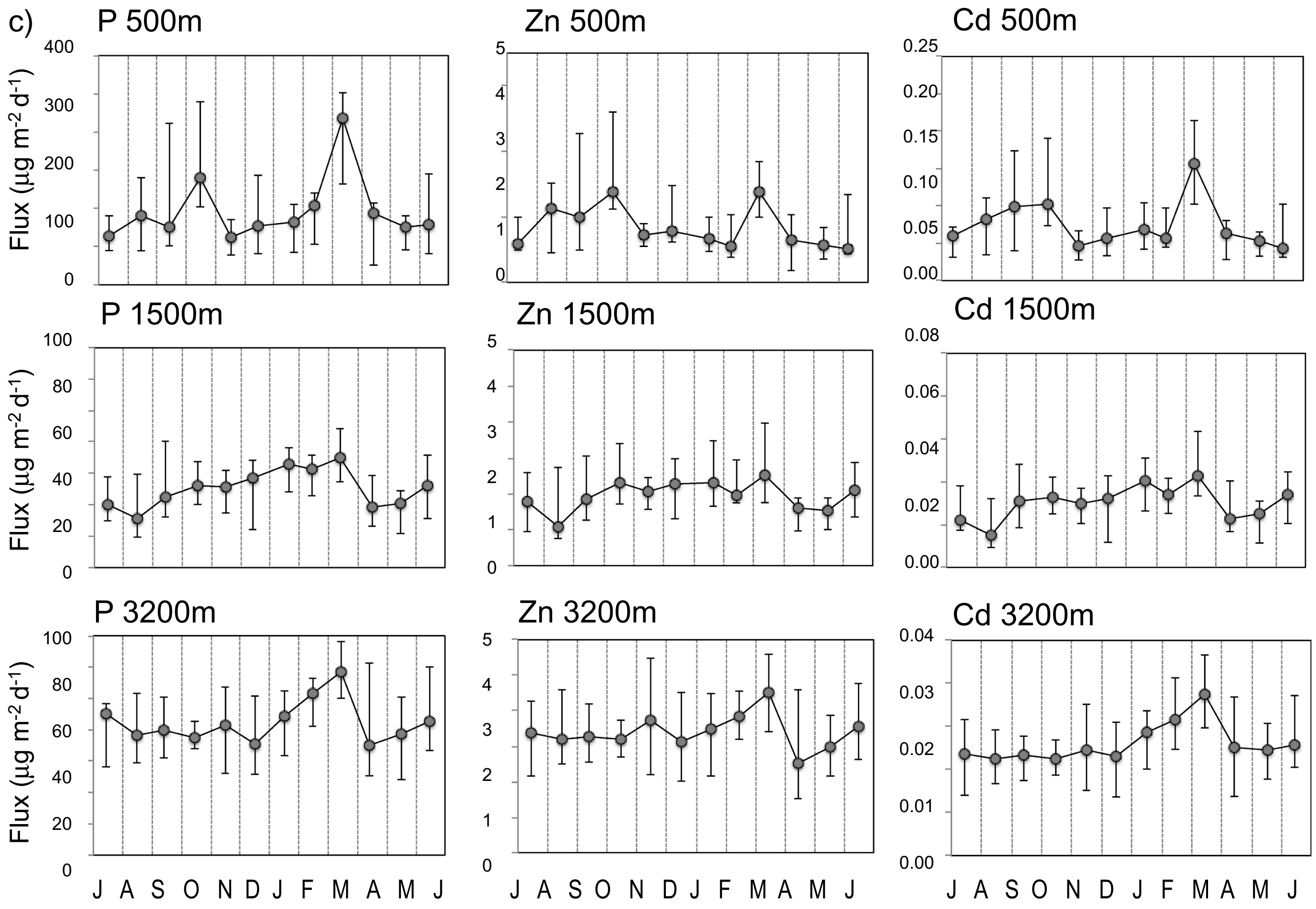

Fig. 4. (*continued*)

corresponds with the seasonal cycle in overlying primary production and surface export flux (Steinberg et al., 2001; Lomas et al., 2013). Significant variability is also observed on both shorter and longer time scales. There is a strong coherence and no temporal lag in mass flux at the three trap depths. Between 500 m and 1500 m depths, both flux variability and the amplitude of the seasonal cycle decrease markedly. The 1500 m and 3200 m fluxes suggest a quasi-constant background flux in the deep ocean that is absent at 500 m depth.

4.1.2. *Major flux components*

The four major components of the mass flux are the biogenic skeletal minerals carbonate and opal, organic matter, and lithogenic material (Conte et al., 2001). Carbonate is the largest component of the flux, averaging 52%, 62% and 60% of the total mass at 500 m, 1500 m and 3200 m depths, respectively, for the time period discussed here. Opal is only a minor fraction of the flux (7%, 10% and 12% at 500 m, 1500 m and 3200 m depths, respectively), consistent with the low diatom productivity at Bermuda (Steinberg et al., 2001, Lomas et al., 2013). Organic carbon (Corg) averages 13% of the flux at 500 m depth and declines to 7% of the flux at 1500 m depth, indicating rapid organic matter remineralization in the mesopelagic. The Corg fraction at 3200 m depth (5%) is only slightly less than at 1500 m depth. Nitrogen averages 2.3% of the flux at 500 m depth, declines to 1.0% of the flux at 1500 m depth and to 0.6% of the flux at 3200 m depth. Interestingly, the fraction of lithogenic material doubles between 500 m (6%) and 1500 m (13%) depth, and continues to increase to 27% of the flux at 3200 m depth.

Carbonate, opal and Corg exhibit a seasonal cycle in fluxes similar to that of the total mass flux, with maximum concentrations in late Feb–Mar coincident with the spring bloom (Fig. 2). (Note the data in Fig. 2 and subsequent figures are plotted July–July to better display the annual Dec–Mar flux maximum, e.g. the “2001” symbol represents the time period from July 2001 to Jun 2002.) The flux variability and seasonal amplitude decrease with depth for all components.

In contrast, lithogenic fluxes exhibit a less pronounced seasonal cycle, with fluxes in Feb–Mar only slightly elevated. In contrast to biogenic components, the variability in lithogenic fluxes is not dampened with increasing depth.

4.2. *Elemental fluxes*

4.2.1. *Summary statistics*

Element fluxes at the three trap depths (< 1 mm fraction) are summarized in Table 2. Like mass flux, the frequency distributions of

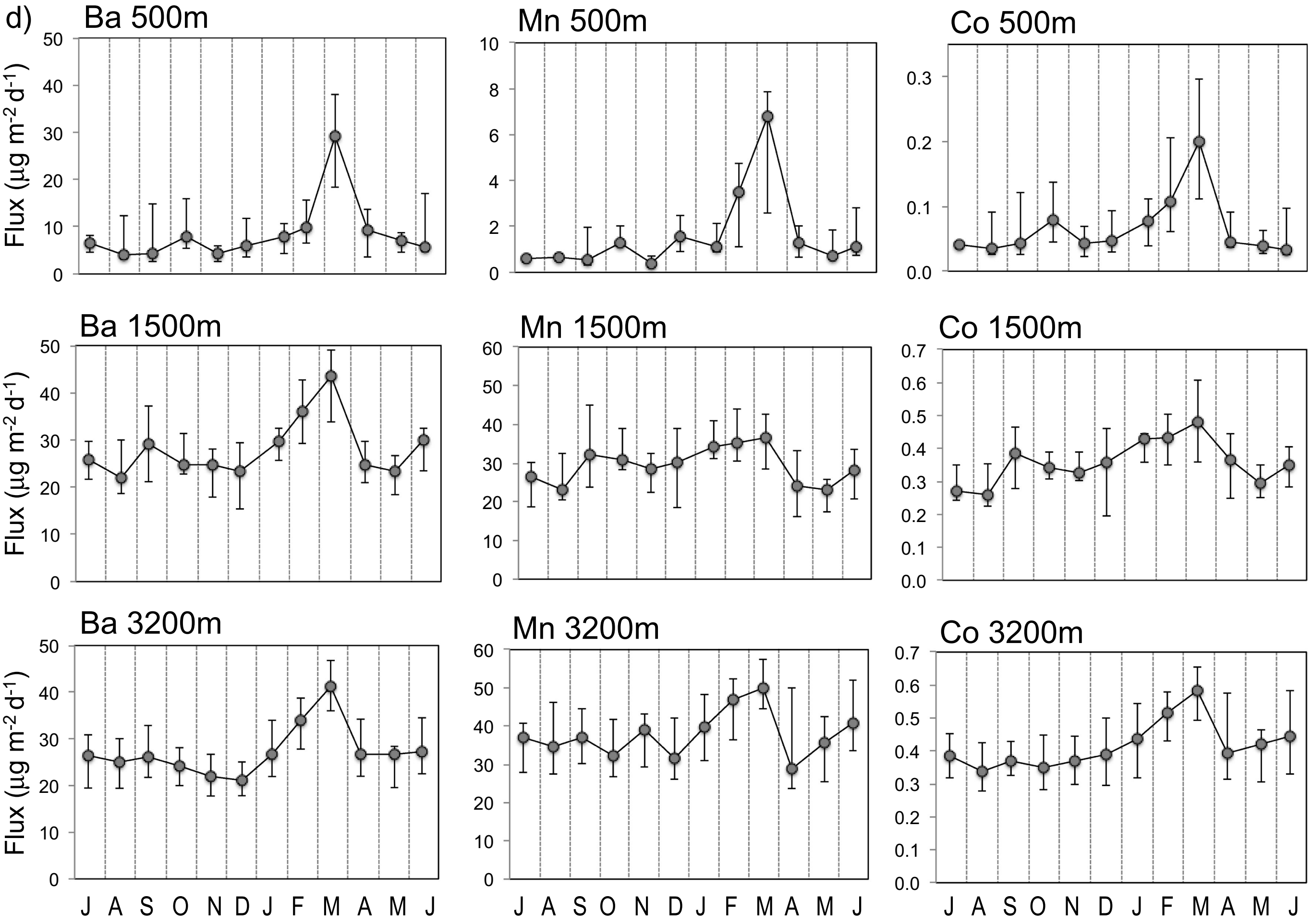

Fig. 4. (*continued*)

element fluxes are skewed with a tail of extreme values (Fig. 3). Thus, the median and quartile data better reflect the central tendencies in the flux than does the arithmetic average, and are used here.

A prominent feature in the element fluxes is the large decrease in fluxes of nutrient elements P and Cd between 500 m and 1500 m depths. Between 500 m and 1500 m depth, median fluxes of P and Cd decrease by 67% and 54%, respectively, indicating extensive losses of nutrient elements as labile organic tissues are degraded in the mesopelagic. Fluxes decrease a further 52% and 37%, respectively between 1500 m and 3200 m depth. In contrast, flux of the nutrient element Zn is similar at 500 m and 1500 m depths, and decreases by only 25% between 1500 m and 3200 m depth.

The losses in nutrient elements are countered by large increases in fluxes of lithogenic elements (Al, Sc and Ti). Median fluxes of Al, Sc, and Ti increase by ~300% between 500 m and 1500 m, and increase a further 40–50% between 1500 m and 3200 m depths. Cu and Ni, which are associated with both organic and lithogenic phases, show a smaller increase with depth, increasing by ~122% between 500 m and 1500 m depth, and by 37% and 13%, respectively, between 1500 m and 3200 m depth.

A second prominent feature in elemental fluxes is the order of magnitude increase in Mn flux between 500 m and 1500 m depth (Table 2, accounting for the ~45% solubilization loss of Mn in the 500 m trap particles). In comparison, the Fe flux only increases by a factor of 3.7 between 500 m and 1500 m depths. These results indicate strong precipitation of Mn oxides in the mesopelagic, and furthermore that Mn oxides are the predominant authigenic phase rather than Fe oxyhydr(oxides). Fluxes of Co and V, which are scavenged by Mn oxides and Fe oxyhydr(oxides) (Shieh and Duedall, 1988; Moffett and Ho, 1996; Hawco et al., 2018), also increase between 500 m and 1500 m depths- by 505% and 395%, respectively.

Ba flux also increases dramatically, by 252%, between 500 m and 1500 m depth, suggestive of significant authigenic barite production within the mesopelagic. Unlike Mn, the Ba flux remains constant between 1500 m and 3200 m depths, which suggests minimal barite production in the deep water column.

A simple measure of variability of the elemental fluxes which is insensitive to extreme values is the range between the 25% and 75 quartiles, normalized to the median (Q-range),

$$\mathrm{Q-range} = \frac{(\mathrm{Q3} - \mathrm{Q1})}{\mathrm{median}} \tag{6}$$

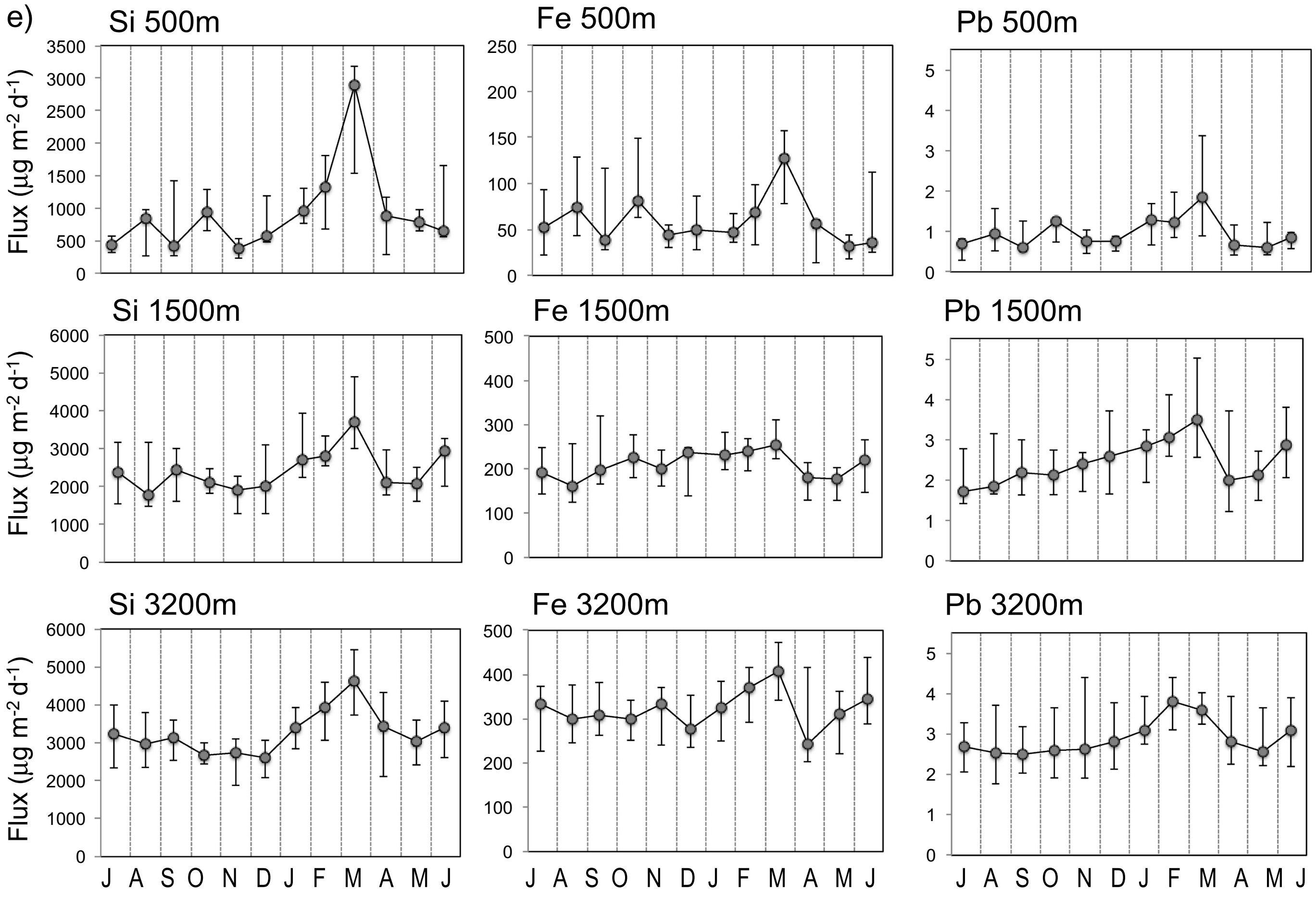

Fig. 4. (*continued*)

where Q3 is the value of the 75% quartile and Q1 is the value of the 25% quartile for the element. As observed for bulk components (Fig. 2), variability in elemental fluxes declines sharply between 500 m and 1500 m depths, and continues to decline between 1500 m and 3200 m depths for most elements (Table 2). In the 500 m flux, the Q-range varies from 77% for P to 196% for Mn (average 132%). In the 1500 m flux, the Q-range is lower and varies from 50% for Co to 100% for Cd (average 64%). The Q-range decreases slightly in the 3200 m flux, from 44% for Cu to 87% for Cd (average 56%). P, Zn and Cd exhibit much higher variability (Q-ranges 76%, 79%, 87%, respectively) in the 3200 m flux than do other elements (Q-ranges between 44 and 60%).

4.2.2. Seasonal variability

The seasonal cycle of individual element fluxes is shown in Fig. 3 and monthly summary statistics are plotted in Fig. 4. Elements associated primarily with carbonates (Ca, Mg, and Sr) exhibit a strong flux peak at 500 m depth that is coincident with the spring productivity maximum in overlying waters (Figs. 3a, 4a). For all three elements, the spring flux peak becomes more damped and broadens with increasing depth. Minimum fluxes are observed during the summer-fall period of low productivity and are higher at 1500 m and 3200 m depths than at 500 m depth. This suggests that aggregation of suspended detrital carbonate particles within the water column (an intrinsic flux component), sourced from past overlying production and/or lateral advection, supplies a more significant fraction of the deep carbonate flux during low productivity periods.

Unexpectedly, nutrient elements associated with organic matter (P, Zn, Cd) have a much less clear seasonal cycle (Figs. 3b, 4b). (Note that the P data is the summed particulate and supernatant fractions, whereas the Zn and Cd data include only the particulate fraction and are thus minimum values, c. f. Table 1). The seasonal cycle of these elements in the 500 m flux is masked by the extreme variability. This variability can be attributed to contamination by swimmers (a particular problem in the 500 m trap), but also reflects pronounced compositional heterogeneity of organic materials in the 500 m flux. Flux variability is much reduced in the 1500 m and 3200 m fluxes although still significant (Fig. 3b). P and Cd have slightly elevated fluxes in Mar, consistent with the seasonal peak in organic carbon (Fig. 2), while Zn shows no clear seasonal cycle (Figs. 3b, 4b).

An interesting feature in the fluxes of lithogenic elements (Al, Ti, Sc) is the evidence for a seasonal cycle (Figs. 3c, 4c). At 500 m depth, lithogenic element fluxes are highly variable, but fluxes tend to be

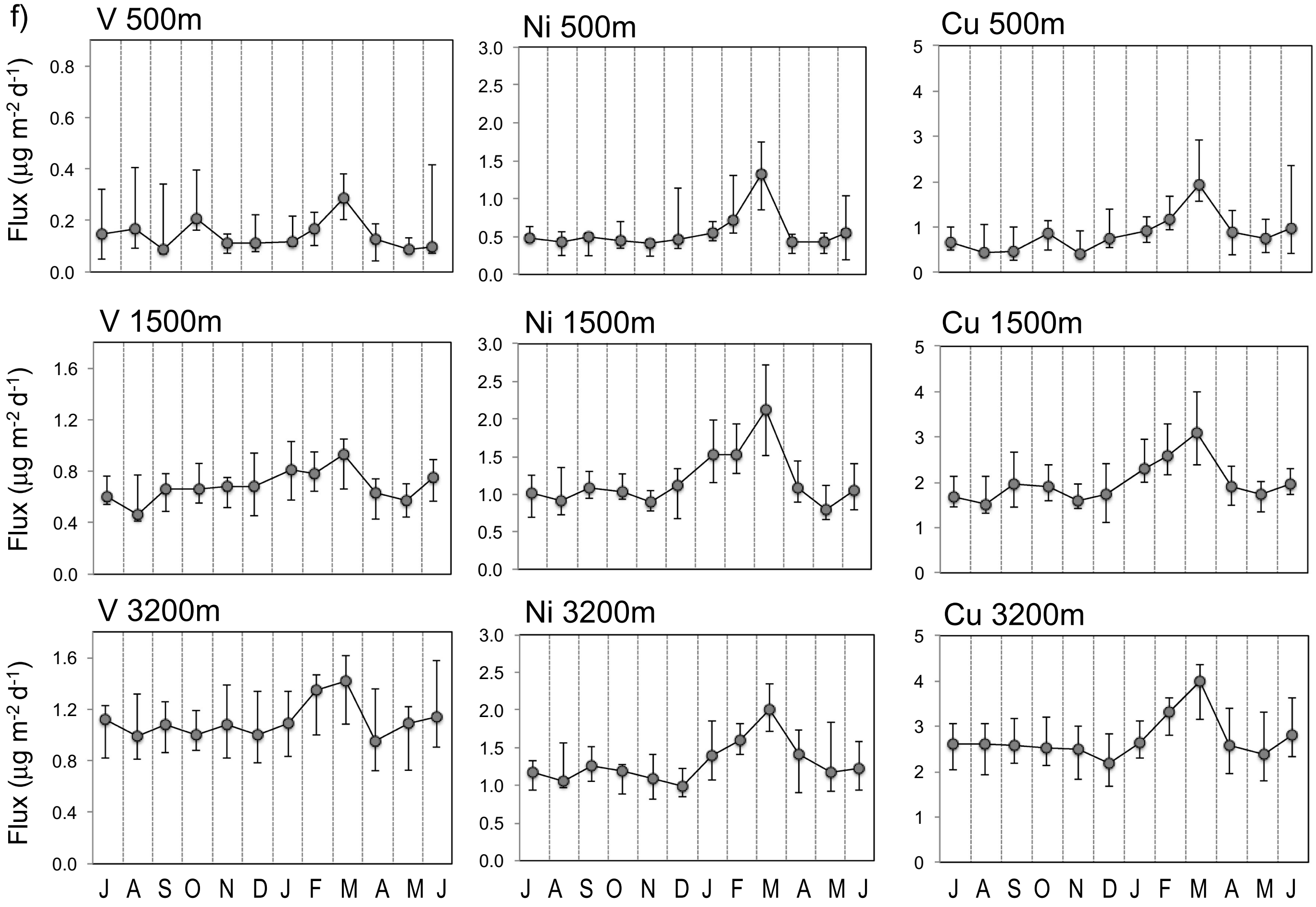

Fig. 4. (*continued*)

elevated in Mar during the spring bloom. Lithogenic fluxes also are elevated in the late summer-fall period in three years (Aug–Sep 2003, Sept–Oct 2005 and Sept–Oct 2006). The timing coincides with the season of Saharan dust deposition at Bermuda (Arimoto et al., 2003; Tian et al., 2008) and suggests that the 500 m trap captured dust deposition events (as observed in summer 2003, Sedwick et al., 2005). Even so, the flux peaks in these years do not rise above background in the 1500 m flux, indicating that any temporal pulses in dust deposition are effectively homogenized by 1500 m depth. No increase in lithogenic element fluxes is observed in the late summer-fall for other years.

A seasonal cycle is also observed in fluxes of elements associated with authigenic minerals (Ba, Mn, Co, Figs. 3d, 4d). The large spring flux peak of Ba at 500 m depth suggests a primary association of Ba with barite precipitated in decaying organic matter (e.g. Bishop, 1988). The seasonal cycle in Ba fluxes at 1500 m and 3200 m depths is remarkably similar (Fig. 4d), with fluxes increasing in Jan to a maximum in Mar at both depths. Mn fluxes also show a tendency for a spring flux peak suggesting a linkage on Mn oxide precipitation and export flux of phytodetritus. Co, which is associated with organic material as well as scavenged by Mn and Fe oxides (Moffett and Ho, 1996), similarly shows a strong spring flux peak at 500 m depth. As observed for lithogenic elements, the seasonal cycles in Mn and Co fluxes are more clearly defined at 3200 m depth than at 1500 m depth.

Elements associated with multiple phases (Si, Fe, Pb, V, Ni, Cu) exhibit spring flux peaks but their peak amplitudes differ (Figs. 3e & f, 4e&f). At 500 m depth, the median spring flux peak for Si, associated in part with opal, is approximately a factor of six higher than the minimum flux in late summer (Fig. 4e). For nutrient elements Fe, Ni and Cu, the spring flux maxima at 500 m depth are approximately 2–3 times higher than the minimum fluxes in late summer. However, for Pb and V, the spring flux maxima at 500 m depth are only ~50% higher than the minimum fluxes. A spring peak in Si, Pb, Ni and Cu fluxes is also clearly seen in the 1500 m and 3200 m fluxes, while for Fe and V, the spring flux peak is only clearly seen in the 3200 m flux, similar to the lithogenic elements (Fig. 4c).

There is significant inter-annual variability in elemental fluxes (Fig. 3). Interestingly, elevated fluxes are occasionally observed in the deep fluxes but not at 500 m depth. For example, fluxes of carbonate and lithogenic elements were elevated in Sep–Oct 2009 (1500 m depth), Feb–Mar 2009 and Apr–Jun 2010 (both 1500 m and 3200 m depths). (Note the data are plotted from Jul–Jul year, so spring 2008 and 2010 data are shown by 2007 and 2009 symbols, respectively.) Ba and Co fluxes were also elevated in the Sep–Oct 2009 event. None of these events were apparent at 500 m depth.

Table 3
Summary statistics of elemental concentrations (mg kg^{-1}) except Si and Ca (g kg^{-1}) and molar ratios. Extreme fluxes from Hurricane Fabian and Igor plumes are not included in statistics. Q1 - 25% quartile, Q3 - 75% quartile.

		Depth		
		500 m	1500 m	3200 m
Mg	Mean	4342	6009	6441
	(Min, max)	(999, 8905)	(2720, 12,322)	(2374, 10,569)
	Median	4123	5749	6405
	(Q1,Q3)	(3087, 5693)	(4951, 6883)	(5720, 7094)
	Q-range	63%	34%	21%
Al	Mean	4820	10,651	15,215
	(Min, max)	(477, 12,729)	(3481, 20,400)	(5567, 26,591)
	Median	4091	10,359	15,263
	(Q1, Q3)	(2327, 6765)	(8344, 12,559)	(12,862, 17,754)
	Q-range	108%	41%	32%
Si (g kg^{-1})	Mean	44	74	93
	(Min, max)	(6, 92)	(30, 133)	(39, 150)
	Median	43	72	91
	(Q1, Q3)	(29, 57)	(61, 85)	(80, 106)
	Q-range	65%	33%	28%
P	Mean	11,398	2170	1023
	(Min, max)	(623, 56,536)	(706, 17,783)	(425, 5175)
	Median	8442	1705	839
	(Q1, Q3)	(4910, 15,111)	(1207, 2364)	(713, 1075)
	Q-range	121%	68%	43%
Ca (g kg^{-1})	Mean	260	262	248
	(Min, max)	(36, 418)	(180, 444)	(130, 357)
	Median	253	257	245
	(Q1, Q3)	(212, 320)	(239, 282)	(231, 267)
	Q-range	43%	17%	15%
Sc	Mean	0.76	1.54	2.10
	(Min, max)	(0.04, 2.44)	(0.60, 2.98)	(0.77, 3.65)
	Median	0.63	1.50	2.09
	(Q1, Q3)	(0.42, 1.07)	(1.26, 1.84)	(1.82, 2.40)
	Q-range	103%	39%	28%
Ti	Mean	244	466	650
	(Min, max)	(6, 808)	(119, 937)	(227, 1224)
	Median	188	455	629
	(Q1, Q3)	(97, 372)	(368, 580)	(518, 773)
	Q-range	146%	47%	41%
V	Mean	9.5	21.0	31.9
	(Min, max)	(0.4, 61.1)	(7.1, 38.5)	(11.4, 51.7)
	Median	6.9	20.9	32.5
	(Q1, Q3)	(4.2, 11.3)	(16.9, 25.0)	(27.1, 37.1)
	Q-range	104%	39%	31%
Cr	Mean	12.0	12.8	16.9
	(Min, max)	(2.7, 42.9)	(3.9, 34.9)	(3.7, 36.2)
	Median	10.3	11.8	16.6
	(Q1, Q3)	(5.5, 15.3)	(9.4, 14.5)	(14.1, 19.8)
	Q-range	94%	43%	34%
Mn	Mean	87	881	1103
	(Min, max)	(13, 420)	(242, 1672)	(366, 1940)
	Median	62	898	1134
	(Q1, Q3)	(40, 99)	(691, 1049)	(936, 1286)
	Q-range	95%	40%	31%
Fe	Mean	3350	6341	9363
	(Min, max)	(154, 17,315)	(2044, 12,210)	(2887, 16,355)
	Median	2548	6099	9621
	(Q1, Q3)	(1481, 4596)	(4832, 7686)	(7957, 10,978)
	Q-range	122%	47%	31%
Co	Mean	3.4	10.4	12.1
	(Min, max)	(0.8, 10.3)	(4.2, 19.1)	(5.4, 21.8)
	median	2.8	10.3	12.2
	(Q1, Q3)	(2.2, 4.1)	(8.4, 12.6)	(10.2, 13.6)
	Q-range	69%	41%	28%
Ni	Mean	30.0	35.1	38.7
	(Min, max)	(3.2, 98.3)	(10.7, 66.3)	(10.7, 102.3)
	Median	23.6	34.3	37.6
	(Q1, Q3)	(16.8, 36.2)	(27.8, 40.7)	(32.2, 44.1)
	Q-range	82%	38%	32%
Cu	Mean	45	61	79
	(Min, max)	(6, 121)	(27, 101)	(32, 154)
	Median	41	59	80
	(Q1, Q3)	(29, 58)	(52, 68)	(68, 90)
	Q-range	70%	28%	28%
Zn	Mean	141	79	57
	(Min, max)	(0.2, 579)	(11, 304)	(4, 233)
	Median	117	67	46
	(Q1, Q3)	(59, 193)	(43, 102)	(36, 66)
	Q-range	115%	87%	66%
Sr	Mean	1638	1810	1714
	(Min, max)	(822, 3111)	(1285, 2922)	(970, 2309)
	Median	1586	1788	1686
	(Q1, Q3)	(1383, 1839)	(1655, 1919)	(1605, 1800)
	Q-range	29%	15%	12%
Cd	Mean	3.86	0.89	0.53
	(Min, max)	(0.10, 25.68)	(0.02, 5.84)	(0.02, 1.86)
	Median	2.24	0.72	0.44
	(Q1, Q3)	(1.34, 3.80)	(0.53, 1.00)	(0.30, 0.64)
	Q-range	110%	65%	78%
Ba	Mean	425	812	777
	(Min, max)	(37, 1134)	(447, 1659)	(412, 1266)
	Median	409	799	778
	(Q1, Q3)	(266, 564)	(683, 934)	(684, 872)
	Q-range	73%	31%	24%
Pb	Mean	55	80	94
	(Min, max)	(7, 205)	(21, 216)	(24, 280)
	Median	44	69	81
	(Q1, Q3)	(26, 77)	(51, 100)	(65, 113)
	Q-range	115%	71%	59%
(b) Molar ratios:				
Ti/Al	Mean	0.030	0.025	0.024
	(Min, max)	(0.007, 0.090)	(0.013, 0.033)	(0.014, 0.042)
	Median	0.029	0.025	0.024
	(Q1, Q3)	(0.022, 0.033)	(0.022, 0.027)	(0.022, 0.026)
	Q-range	38%	20%	14%
Al/Fe	Mean	3.2	3.5	3.4
	(Min, max)	(0.2, 9.8)	(2.6, 4.5)	(2.5, 6.3)
	Median	3.4	3.5	3.3
	(Q1, Q3)	(2.8, 3.4)	(3.3, 3.7)	(3.2, 3.5)
	Q-range	29%	12%	11%
Fe/Ti	Mean	13.2	12.0	12.6
	(Min, max)	(0.8, 9.5)	(8.3, 20.4)	(5.9, 19.1)
	Median	11.1	11.6	12.7
	(Q1, Q3)	(8.3, 14.6)	(10.7, 12.8)	(11.7, 13.5)
	Q-range	57%	18%	14%
Mn/Ti	Mean	0.5	1.7	1.5
	(Min, max)	(0.1, 0.9)	(0.6, 3.1)	(0.6, 2.4)
	Median	0.3	1.7	1.5
	(Q1, Q3)	(0.2, 0.6)	(1.5, 1.9)	(1.3, 1.7)
	Q-range	131%	30%	24%

4.3. Flux elemental composition

4.3.1. Summary statistics

Summary statistics of flux elemental composition at the three trap depths are shown in Table 3. Mean concentrations of the nutrient elements P, Zn and Cd decrease by 80%, 43% and 68%, respectively, between 500 m and 1500 m depth and then decrease by another 51%, 32% and 40% between 1500 m and 3200 m depth. Conversely, concentrations of the lithogenic elements Al, Sc and Ti increase by 153%, 137% and 143% respectively between 500 m and 1500 m depths, and increase by another 47%, 40% and 38%, respectively between 1500 m and 3200 m depth. Concentrations of elements such as Cu, Ni, Pb, which are associated with both organic and lithogenic/authigenic phases, show an intermediate enrichment, increasing by 45%, 45%, 57%, respectively, between 500 m and 1500 m depth, and a further 35%, 10%, 17%, respectively, between 1500 m and 3200 m depth.

Mn concentration increases by an order of magnitude from 500 m to 1500 m depth and by another 26% between 1500 m and 3200 m depth,

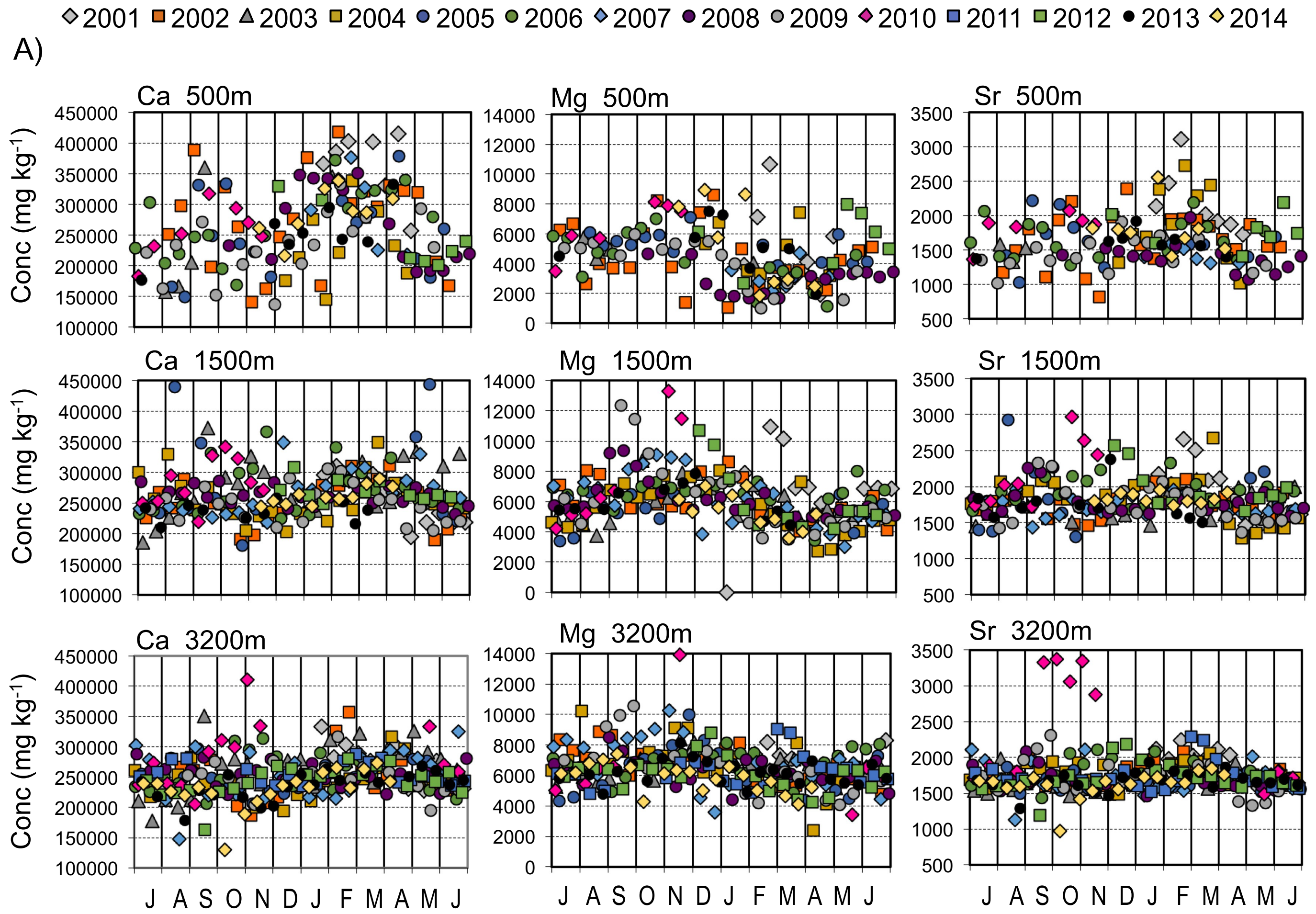

Fig. 5. Seasonal variation in elemental concentrations (mg kg^{-1}) at the three trap depths. The concentrations are plotted July–July to better display the late winter–spring annual flux maximum. The years correspond to the year of the July start date (i.e. the symbol for 2001 denotes July 2001–June 2002). The y-axis is scaled to show the general seasonal trends and so may differ between trap depths (extreme values associated with the Hurricanes Fabian (2003) and Igor (2010) sediment plumes are off scale). (a) Carbonate elements (b) nutrient elements (c) lithogenic elements (d–f) authigenic and mixed source elements.

consistent with high rates of authigenic Mn oxide precipitation in the mesopelagic. Co, an element strongly scavenged by Mn oxides, increases by 266% between 500 m and 1500 m depth, and a further 18% between 1500 m and 3200 m depth. V, another scavenged element, exhibits a different depth trend from Co, increasing by 204% between 500 m and 1500 m depths, then by 56% between 1500 m and 3200 m depths.

Ba concentration increases by 95% between 500 m and 1500 m depths but does not show any further increase between 1500 m and 3200 m depth, despite the continuing enrichment in lithogenic elements. This, as well as the lack of an increase in Ba flux between 1500 m and 3200 m (Figs. 3d, 4d), suggests that Ba is mainly associated with barite and that barite precipitation is largely confined to mesopelagic depths.

Elements associated with different phases show differences in the variability of their concentrations (Table 3). In particular, carbonate elements are significantly less variable than other elements. In the 500 m flux, Q-ranges for the carbonate elements Ca, Mg and Sr are 43%, 63% and 29%, respectively, while those of the lithogenic elements Al, Sc and Ti are 108%, 103% and 146%, respectively. Q-ranges for mixed source elements are also higher than for carbonates, ranging between 70% (Cu) to 122% (Fe).

As observed in bulk components (e.g. Conte et al., 2001), the compositional variability of the flux decreases rapidly between 500 m and 1500 m depths. Q-ranges of the carbonate elements Ca, Mg and Sr in the 1500 m flux (17%, 34% and 15%, respectively) are half that seen in the 500 m flux. Q-ranges of lithogenic elements decrease even more substantially by about 35% between 500 m and 1500 m depths. In contrast, the decrease in Q-ranges between 500 m and 1500 m depths for the nutrient elements P, Zn and Cd, and for Pb is lower, with Q-ranges in the 1500 m flux averaging 68%, 87%, 65%, 71%, respectively. At 3200 m depth, Q-ranges of carbonate and lithogenic elements are similar to those at 1500 m depth, whereas the Q-ranges of P, Zn, Cd and Pb are about 30% lower at 3200 m depth.

Selected molar ratios are given in Table 3. The median Ti/Al molar ratio decreases slightly from 0.029 to 0.025 between 500 m and 1500 m depths, and remains constant between 1500 m and 3200 m depths. The small increase in Al relative to Ti could reflect higher scavenging of Al onto biogenic phases (e.g. Bruland and Lohan, 2003). The Fe/Ti ratio increases slightly with depth, from 11.1 at 500 m depth to 12.7 at

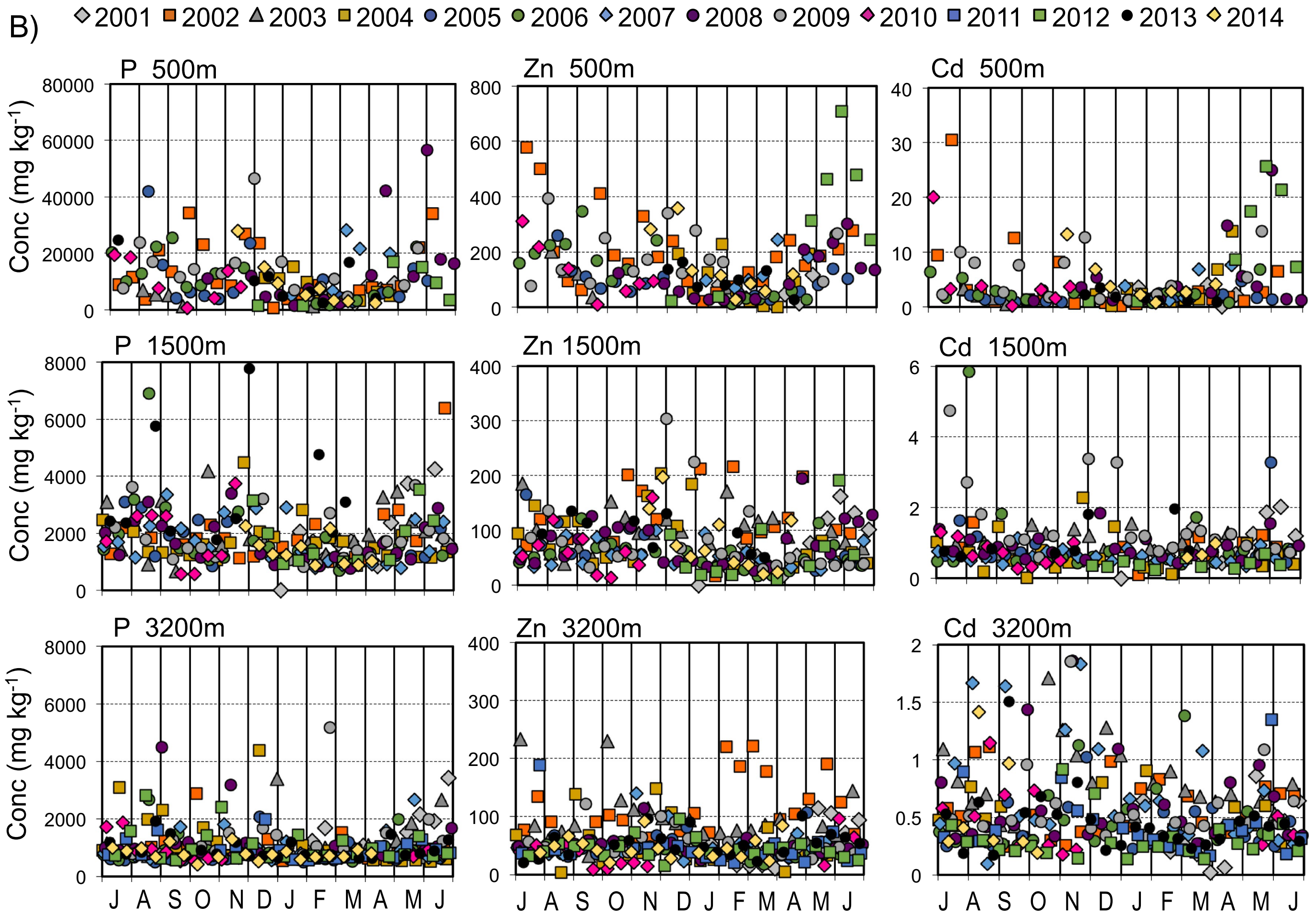

Fig. 5. (*continued*)

3200 m depth. The molar ratios in the flux are more similar to those of deep suspended particles collected at Bermuda and near the North American continental margin (Ohnemus and Lam, 2015) than those in Saharan dust (Ti/Al > 0.04, Fe/Ti ~5–8; Arimoto et al., 1995, Moreno et al., 2006, Tian et al., 2008, Trapp et al., 2008, Shelly et al., 2015). The molar Mn/Ti ratio, an indicator of the changes in relative abundance of authigenic Mn oxide relative to lithogenic material, increases sharply between 500 m (0.3) and 1500 m (1.7) depths but then decreases slightly in the 3200 m flux (1.5), suggesting higher aggregation of suspended lithogenics relative to increases from authigenic mineralization in the deep water column.

4.3.2. Seasonality in flux composition

Seasonal variation in flux composition reflects seasonal changes in the relative contributions of different flux carriers, in particular the balance between the processes of chemical scavenging and suspended particle aggregation that contribute to intrinsic flux generation within the water column and the extrinsic flux that is sourced from overlying surface water production. Elemental concentrations of individual samples are shown in Fig. 5 and summary statistics in Fig. 6. Seasonal variation in carbonate element concentrations (Figs. 5a, 6a) is highest for Ca, which peaks during the late Dec-Mar period of maximum biogenic carbonate production. A small spring peak is also observed in Sr concentration but not for Mg. Unexpectedly, concentrations of the nutrient elements P, Zn and Cd (Figs. 5b, 6b) are not elevated during the spring bloom period. At 500 m depth, concentrations are in fact at a minimum in Mar, indicating the dominance of biogenic carbonate production in extrinsic flux generation. Nutrient element concentrations subsequently increase in late spring and early summer in the 500 m flux, but remain relatively constant in the 1500 m and 3200 m flux.

The concentrations of the lithogenic elements Al, Ti and Sc (Figs. 5c, 6c) all exhibit a seasonal maximum in Sep–Oct and then decline to minimum concentrations in Mar that are a factor of 2–3 lower than the maximum concentrations. This seasonal cycle in concentrations indicates a seasonal dilution of the (intrinsic) lithogenic flux component with biogenic material, primarily biogenic carbonates (Fig. 5a), sourced from recent overlying production (the extrinsic flux component). The Sep–Oct maximum in lithogenic element concentrations likely reflects the low contributions from extrinsic biogenic fluxes during the seasonal minimum in productivity and possibly increased dust deposition in the fall.

Concentrations of Ba, Mn and Co (Figs. 5d, 6d), Si, Fe, Pb (Figs. 5e, 6e) and V and Cu (Figs. 5f, 6f) in the 1500 m and 3200 m flux exhibit similar, though smaller, Jan–Mar dilution patterns as the lithogenic elements but little evidence of a fall maximum. In contrast, Ni shows no

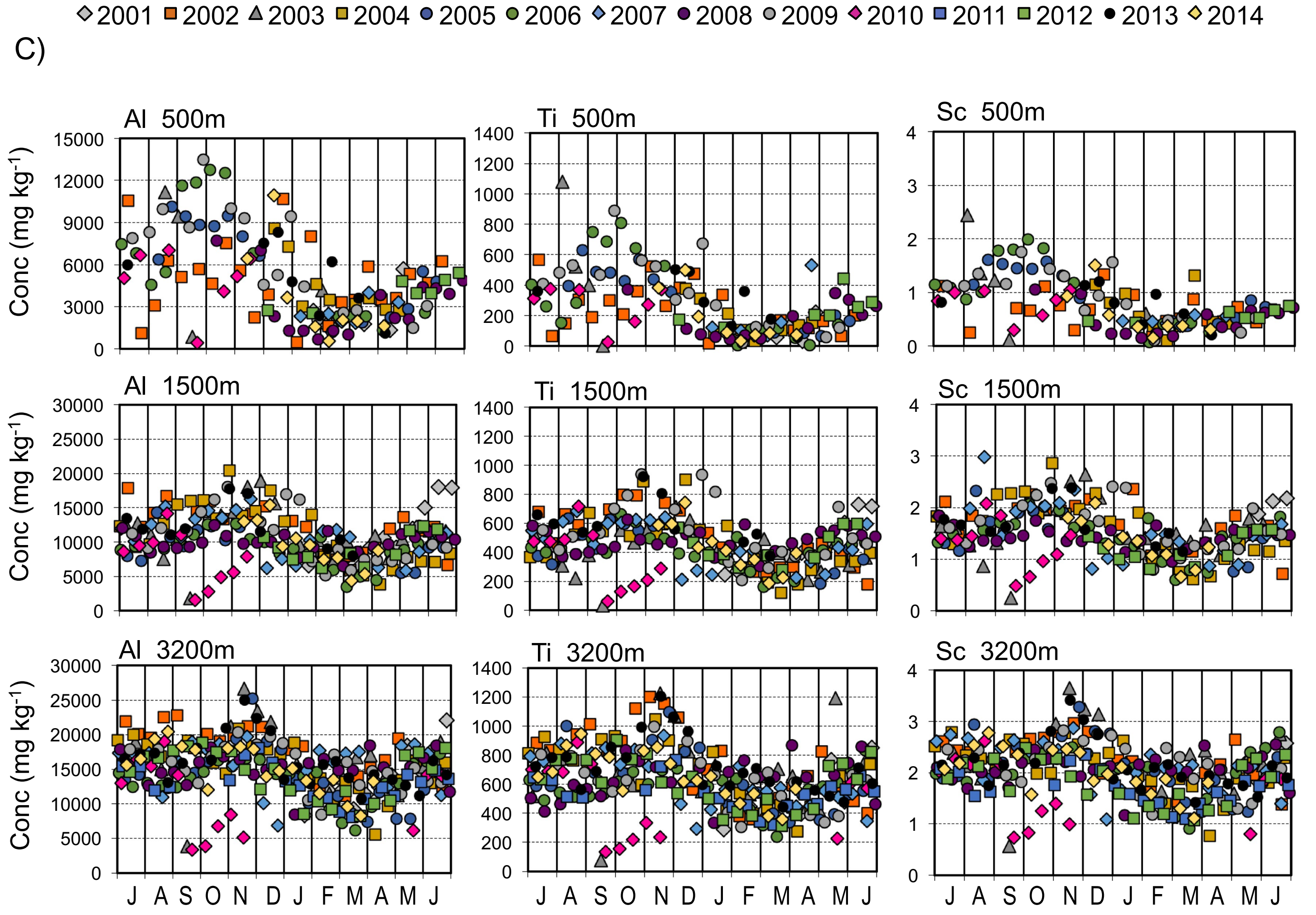

Fig. 5. (*continued*)

clear seasonal cycle in concentration (Figs. 5f, 6f).

4.4. Elemental partitioning among flux carrier phases

Principal Components Analysis (PCA) was performed to quantitatively examine elemental associations. PCA was first performed using the full element concentration dataset, including organic carbon, nitrogen and carbonate as variables. The first PCA factor comprised 36.4%, 42.0% and 43.1% of the total variance in the 500 m, 1500 m and 3200 m data, respectively (Fig. 7). Lithogenic (and authigenic) elements are heavily loaded on PCA Factor 1 at all depths. PCA Factor 2 comprised 18.1%, 12.9% and 10.2% of the total variance in the 500 m, 1500 m and 3200 m data, respectively. Organic carbon and nitrogen are heavily loaded on Factor 2 at all depths.

Scatter plots of the element loadings on Factor 1 ("Lithogenic") versus Factor 2 ("Organic Matter") show a clear transition in element associations with increasing depth (Fig. 7). At 500 m depth, the nutrient elements P, Zn are strongly loaded on Factor 2 ("Organic Matter"), as are Cd and Pb to a lesser extent. Most other elements are strongly positively loaded on Factor 1 ("Lithogenic"), although the loadings of Ni, Cu and Cr are weaker. The similar loading of Al with Sc and Ti on Factors 1 and 2 indicates a strong association of Al with lithogenic phases and that Al associations with non-lithogenic organic and/or carbonate phases is minor. This pattern in factor loadings shifts in the 1500 m flux. The loading of P on Factor 2 decreases, and loadings of Cu, Ni, Cr and Pb on Factor 1 increase. This trend continues in the 3200 m flux. In the 3200 m flux, P is no longer loaded on Factor 2. Additionally, Zn and Cd loadings on Factor 2 decrease while the loading of Cd on Factor 1 increases. These results indicate that with increasing depth, the association of the nutrient elements P, Zn and Cd with organic matter weakens, and that most elements (e.g. Cd, Cu, Ni, Pb) become increasingly associated with lithogenic and authigenic phases.

The PCA results above do not differentiate between the associations of elements with lithogenic versus authigenic phases. To explore further how element associations with non-lithogenic phases change, we first compared the elemental concentrations in the flux material with that of the upper continental crust (UCC, Rudnick and Gao, 2003) and calculated elemental enrichment factors (EFs). The comparison with UCC is necessarily a rough approximation of the actual lithogenic flux composition and thus calculated EFs will include any deviation between the UCC and the actual lithogenic composition.

Calculated EFs for the flux material at the three trap depths are given in Table 4. EFs for Sc, Ti are near unity while Fe is only slightly enriched (1.5–1.6), indicating that these elements can be primarily

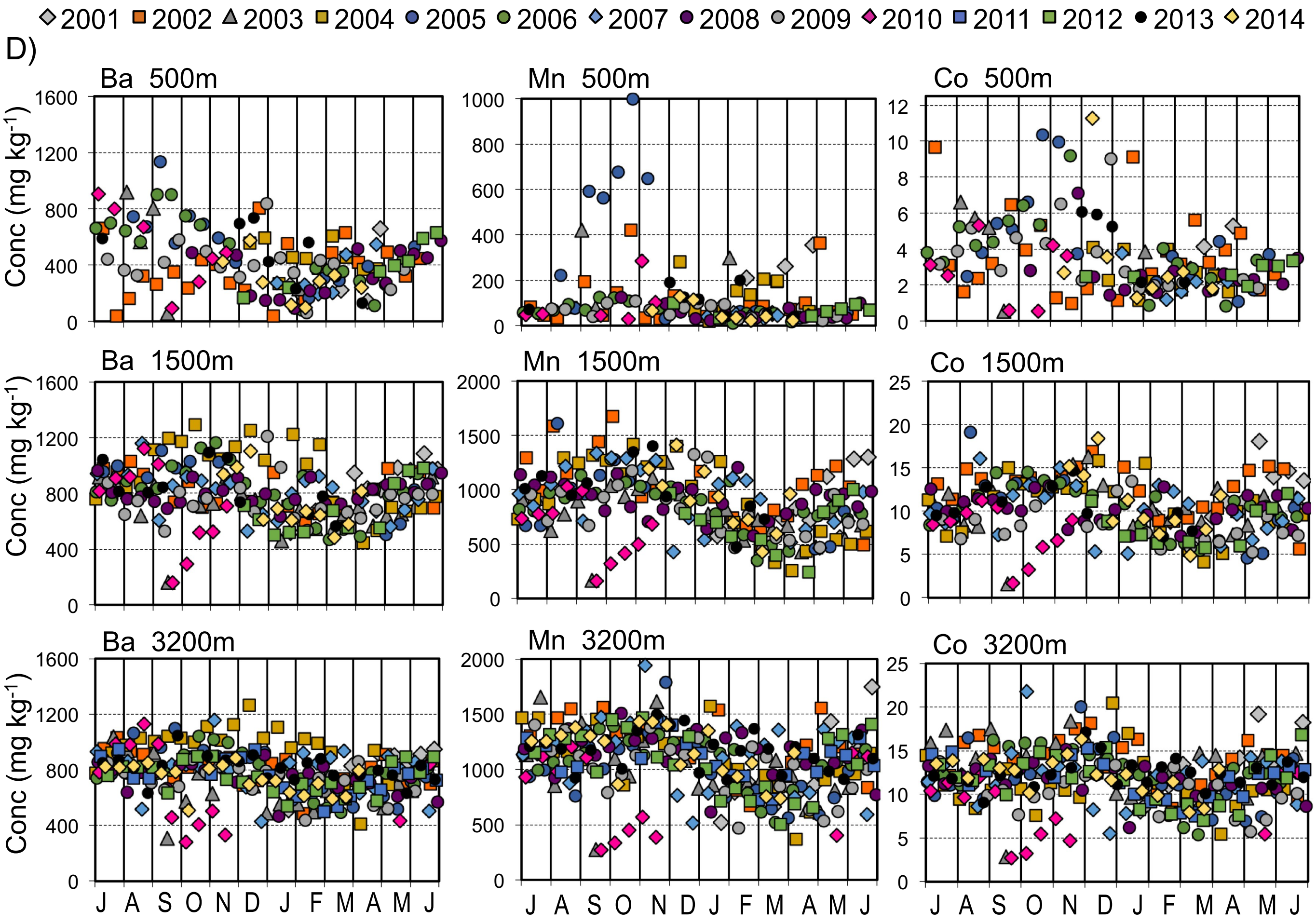

Fig. 5. (*continued*)

attributed to a lithogenic component. In contrast Si at 500 m depth is enriched by a factor of three, reflecting its occurrence in opal. The EF of Si decreases from 3.0 at 500 m depth to 2.0 at 1500 m depth, suggestive of opal dissolution in the mesopelagic. The EFs of Cd, Ni, Zn, Cu and Pb at 500 m depth range from 13 (Ni) to 690 (Cd), and also decrease significantly with depth, consistent with their release during organic matter remineralization in the mesopelagic. Not surprisingly, the EF of Mn increases by a factor of four between 500 m and 1500 m depths, from 2.2 to 10.4, indicative of strong authigenic precipitation of Mn oxides in the mesopelagic. In contrast, there is no increase in the EF of Fe with depth, indicating that authigenic precipitation of Fe oxyhydr (oxides) in the mesopelagic is minor at this site. The EFs of Co and V also increase between 500 m and 1500 m depths, indicative of their strong scavenging by Mn oxides.

Using the first order assumption that lithogenic flux composition is similar to that of the UCC, the "excess" flux and concentrations of the elements (i.e. that is not supported by lithogenic material) were calculated, which was then used to estimate the percentage of the element flux carried by lithogenic phases (Table 5). In the 500 m flux, 94% of the Sc and 84% of the Ti is carried by lithogenic phases. In contrast, 1% or less of the carbonate elements Ca and Sr, and the nutrient elements Zn, Cd or Pb are sourced from lithogenic material. Estimates for Cu (2%) and Ni (6%) also indicate a minimal lithogenic carrier phase at 500 m depth. Other elements show intermediate lithogenic contributions in the 500 m flux, ranging between 20% for Co to 73% for Cr. With increasing depth, the fraction of the element concentrations that can be attributed to a lithogenic source increases substantially for Mg, Ni, Cu, Pb and especially Zn.

In contrast, the fraction of Mn associated with a lithogenic phase decreases by a factor of five, from 50% in the 500 m flux to 10% in the flux at 1500 m and 3200 m depths. Assuming that the Mn_{xs} is sourced entirely from Mn oxides, and estimating the Mn oxide chemical composition as simply MnO_2 (e.g. Lam et al., 2015), Mn oxides contribute < 0.01% of the 500 m flux, 0.13% of the 1500 m flux (range 0.03%–0.24%) and 0.15% of the 3200 m flux (range 0.05% to 0.28%).

Ba_{xs} fluxes tripled between 500 m and 1500 m depths, confirming the high barite precipitation in the mesopelagic, but remained constant between 1500 m and 3200 m depths. Assuming that all the Ba_{xs} is sourced from authigenic barite, barite contributes about 0.07% of the 500 m flux (range 0.01%–0.18%) and increases to approximately 0.12% in both the 1500 m flux (range 0.07%–0.26%) and 3200 m flux (range 0.06%–0.19%).

Excess fluxes of Cd, P and Zn decrease by 95%, 70% and 15% between 500 m and 1500 m depth (Table 5), indicative of their relative

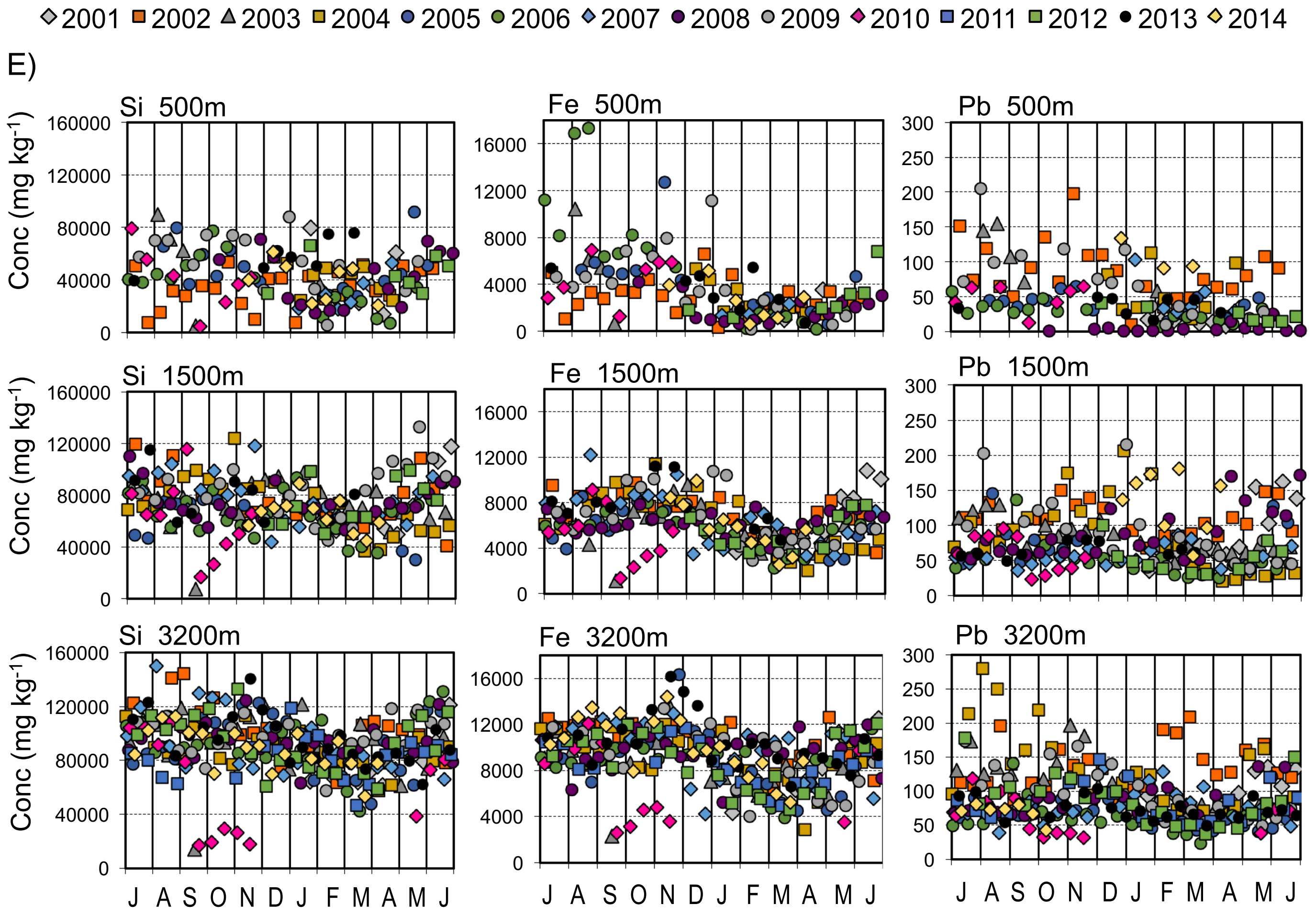

Fig. 5. (*continued*)

rates of net loss in the mesopelagic. Excess fluxes continue to decrease between 1500 m and 3200 m depth by 67%, 55%, and 35%, respectively, between 1500 m and 3200 m. In contrast, excess fluxes of V, Fe, Co, Ni, Cu and Pb increase with depth, suggesting scavenging by Mn oxides.

To further investigate element associations with non-lithogenic phases, a second PCA analysis was performed using elemental excess concentrations. Fig. 8 shows elemental loadings on the first three PCA factors at 500 m and 1500 m depths, which comprised 49.8% and 52.9% of the variance, respectively. (Factors 4–6 loadings did not show meaningful patterns and so are not shown.) At 500 m, Factor 1 (20.7% of the variance) has high loadings of organic carbon, N, P and Zn as well as Cd, Ba and Pb, clearly an organic matter signature. Small loadings of Ti and Fe may reflect incorporation of a lithogenic component within organic aggregates such as fecal pellets and amorphous aggregates and/or Fe association with organic phases. Factor 2 (16.2% of the variance) has high loadings of residual Ti and Fe, Co, Ni, Cu and Ba and moderate loading of Cu and Zn, suggestive of an authigenic barite plus additional Fe oxide and/or lithogenic phases having compositions that differ from that of UCC. Factor 3 (12.9% of the variance) has high loadings of the nutrient elements Cu, Zn, Ni, Cd, and moderate loadings of organic carbon, N, P and Ba. This signature of high loadings of easily-remineralized elements on Factor 3 suggests an organic fraction that is more labile and remineralized at a different rate than the organic fraction represented by Factor 1. In the 1500 m flux, Factor 1 (24.2% of the variance) has high loading of Mn, Ba and elements scavenged by Mn-Fe oxides, with a moderate loading of residual Ti, clearly an authigenic signature. Factor 2 (17.3% of the variance) has high loadings of organic carbon, N and the nutrient elements P, Zn and Cd, clearly an organic signature. Factor 3 (11.4% of the total variance) has high loadings of carbonate and carbonate elements Ca and Sr and a small loading of Mg, clearly a carbonate signature.

The PCA result at 3200 m depth (Fig. 9) shows many similarities with that at the 1500 m depth (Fig. 8) but there are also several revealing differences. At 3200 m depth, Factor 1 (26.1% of the variance) has very high loadings of Ba, Mn and Fe (Fig. 9). Elements heavily scavenged by Mn oxides (Co, V, Ni, Cu) also are mainly loaded on Factor 1, clearly an authigenic signature. In addition, Factor 1 also has moderate loadings of Cd and Pb. Factor 2 (13.0% of the variance) has high loadings of carbonate and carbonate elements Ca, Mg, Sr, clearly a carbonate signature. There is also a small loading of Zn and Co on Factor 2. Factor 3 (11.4% of the variance) has high loadings of organic carbon and N, clearly an organic factor. There are also small loading of Sc and Ca on Factor 3, suggestive of organic-mineral associations (e.g.

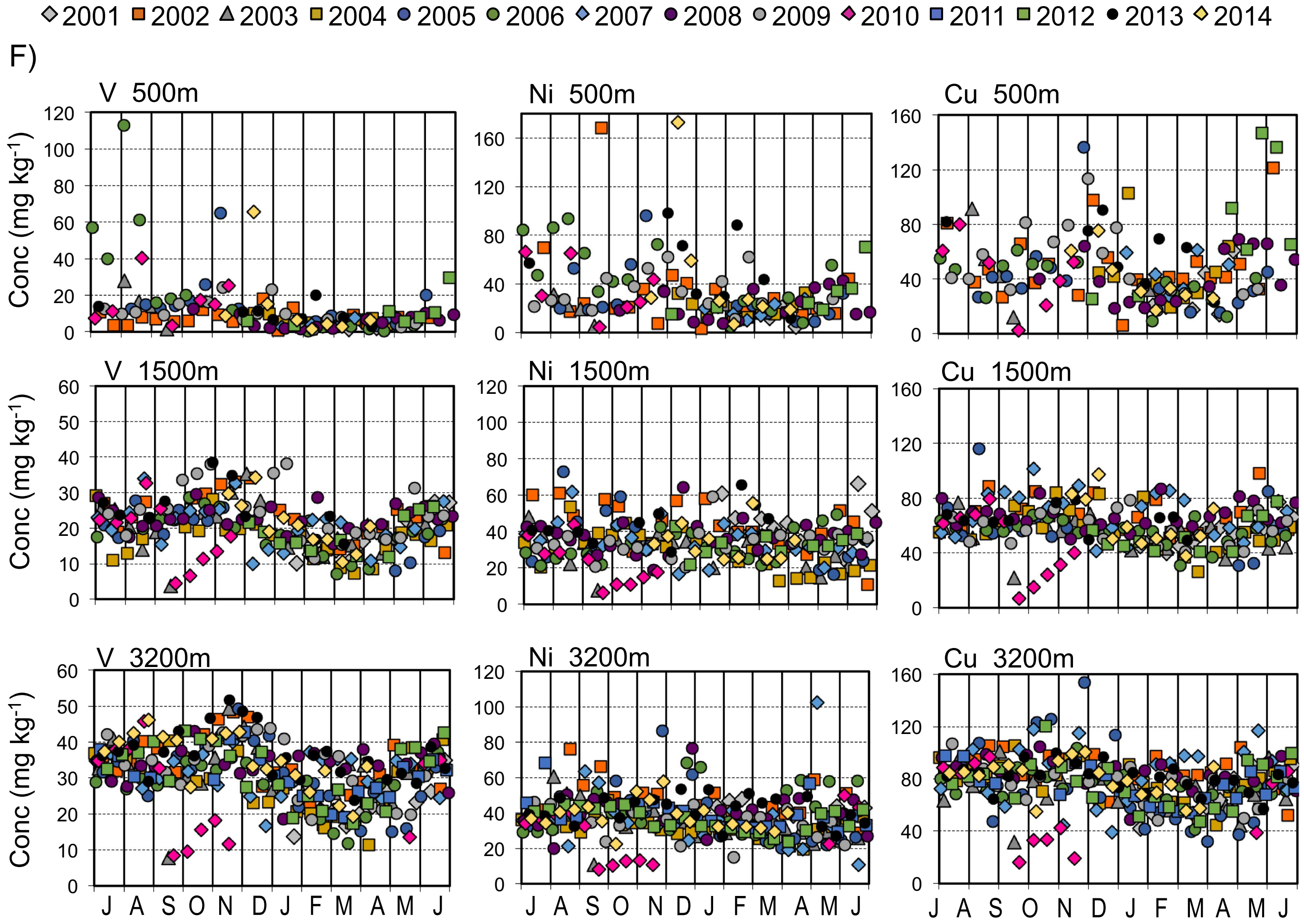

Fig. 5. (*continued*)

organic coatings on particles). Loadings of nutrient elements (Cd, Zn, Ni, P) are minor or nearly zero (P) on Factor 3, indicating that by 3200 m depth these elements are largely disassociated from organic flux carrier phases. Factor 4 (8.9% of the variance) is heavily loaded with the residual Sc, Ti, and Mg and has minor loadings of Fe, Cr, Ni and Cd. This element pattern appears to reflect a mafic component of the lithogenic material, as these elements are enriched in mafic and ultramafic minerals relative to UCC. Factor 5 is loaded mainly with Cr and Ni. These elements are components of stainless steel (~18% and 8%, respectively), so this likely reflects intermittent or low level contamination from the stainless mooring components (see Section 3.2.2.). Factor 6 (6.2% of the variance) is loaded mainly with Si, P and Zn, reflecting a biogenic Si (opal) component. The loading of Zn on Factor 6 is consistent with its incorporation into opal (Ellwood and Hunter, 2000). The loading of P is consistent with its association with opal (Latimer et al., 2006), as well as the strong partitioning of P on opal in the deep OFP traps (Carter et al., 2016). It is interesting that the only significant loading of P on any of these six factors is with the opal factor, indicating that in the deep water column, the geochemical behavior of P is largely independent of the organic carbon phases.

Scatterplots of excess concentrations provide further evidence for the depth evolution in the associations of trace elements Fe, Co, Ni, Cu and V with authigenic Mn oxides (Fig. 10). In the 500 m flux, no correlations are observed between Mn_{xs} and excess concentrations of any of these elements, indicating that they are not closely associated with authigenic Mn oxides at this depth. However by 1500 m depth, all elements are significantly correlated with Mn_{xs}. The slopes of the regressions on Mn_{xs} in the 1500 m flux range from 2.53 for Fe_{xs} (2.49 molar Fe/Mn ratio) to 0.007 for Co_{xs} (0.0065 molar Co/Mn ratio) and V_{xs} (0.0075 molar V/Mn ratio). In the 3200 m flux, significant regressions of these elements on Mn_{xs} concentration are also observed, but with differences that indicate change in the Mn oxide composition. For Co_{xs} and Ni_{xs}, regressions on Mn_{xs} are nearly identical in the 1500 m and 3200 m flux, with slopes of 0.01 and 0.02, respectively. In contrast, the slopes of the regressions of Fe_{xs} (3.81), Cu_{xs} (0.05) and V_{xs} (0.014) in the 3200 m flux are 50%, 14% and 100% higher, respectively, than those in the 1500 m flux. Furthermore, the r^2 of the regression for V_{xs} in the 3200 m flux is double that in the 1500 m flux. The differences

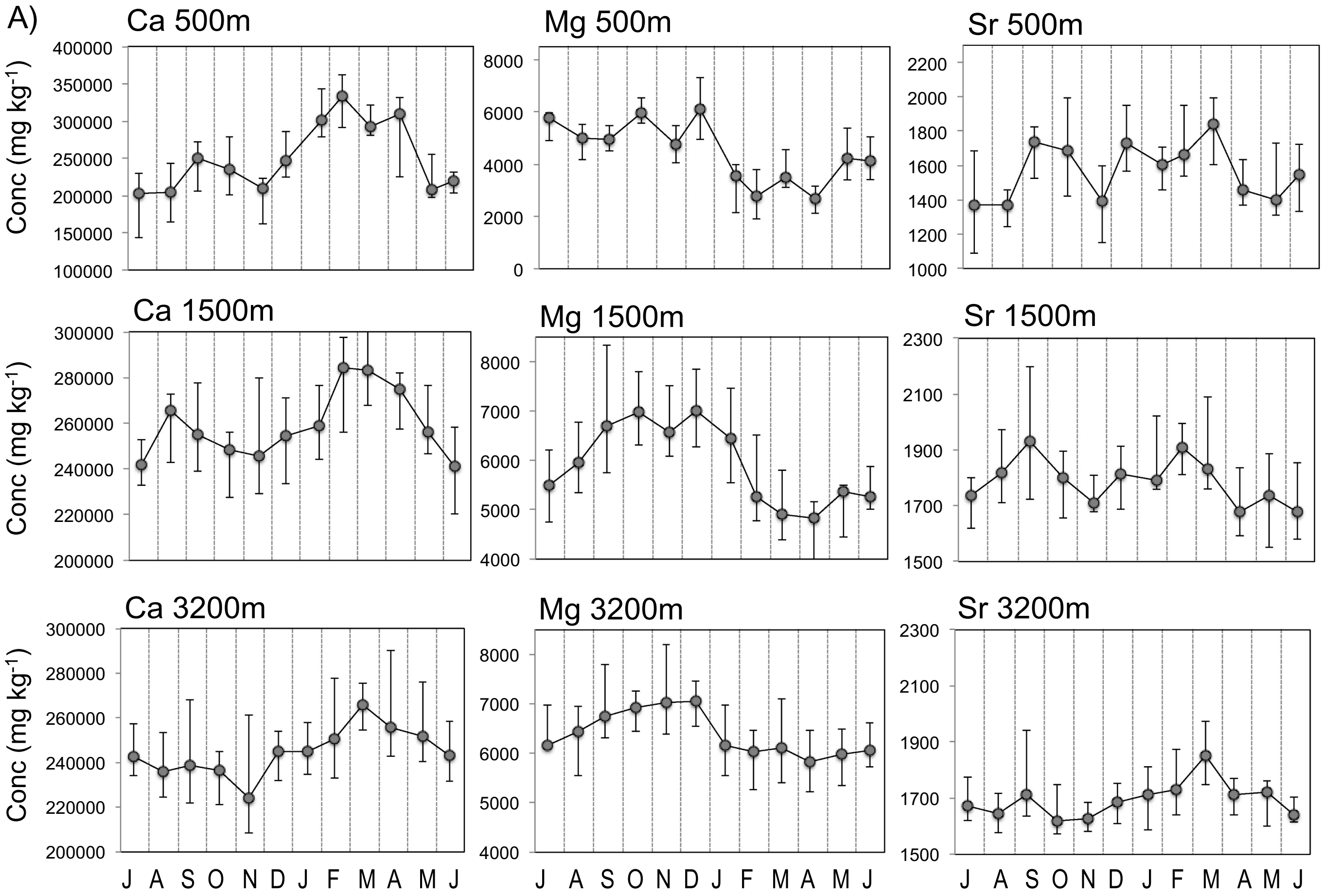

Fig. 6. Summary statistics of monthly elemental concentrations at the three trap depths. The data are plotted from July–July to better show the seasonal flux maximum. The y-axis is scaled to show the general seasonal trends and so may differ between depths. Plotted are the median concentrations and bars showing the range between the 25% and 75% quartiles. (a) Carbonate elements (b) nutrient elements (c) lithogenic elements (d–f) authigenic and mixed source elements.

indicate significant enrichment of Fe, Cu and V, but not Co or Ni, in Mn oxides in the 3200 m flux relative to the Mn oxides in 1500 m flux.

5. Discussion

5.1. Seasonal variability in elemental fluxes and flux composition

The elemental fluxes at the OFP site highlight the strength of the coupling between the deep particle flux and upper ocean biogeochemistry. The nutrient elements P, Zn, Cd, Co, Ni, and Cu, which are important trace elements in phytoplankton (Martin and Knauer, 1973; Morel and Price, 2003) exhibit a spring flux peak at 500 m depth that coincides with the timing of the overlying spring bloom (Fig. 3). PCA factor loadings indicate these elements are closely associated with organic material in the 500 m flux (Figs. 7, 8). These observations are consistent with their primary association with cellular material in the euphotic zone (Twining et al., 2015) and with the correlations observed between POC and particulate Cd, Co, Ni, Cu and Zn in surface waters (Kuss and Kremling, 1999b). These data confirm that labile organic material, in particular the surface export of phytodetritus from the spring bloom, is a major carrier of these elements into the mesopelagic. However, as discussed below, the close association of many of these elements with organic flux carrier phases breaks down with increasing depth as organic material is remineralized, and these elements become more strongly associated with non-biogenic flux carrier phases, in particular Mn oxides (Fig. 8, 9, 10).

Strong seasonality and a spring seasonal flux peak are also observed for Ba (Fig. 3e), indicating a linkage between production of authigenic barite and the export flux of phytodetritus from the spring bloom. This is consistent with barite production in microenvironments of decaying phytoplankton cells (Bishop, 1988).

The fluxes of Ca, Mg and Sr (Fig. 3a) clearly mirror the seasonal cycle of calcifying plankton productivity at Bermuda. The amplitude of the seasonal cycle becomes dampened with depth, and there is also the enigmatic observation that the carbonate flux in the deeper traps during the summer-fall minimum in surface water productivity is, on average, higher than that at 500 m depth (Fig. 2). Together, these observations suggest that an increasing fraction of the carbonate flux with depth is sourced from aggregation of suspended carbonate particles within the water column (an "intrinsic" flux component, possibly including advected material) rather than from recent export production (the "extrinsic" flux component). This conclusion is reasonable as the extrinsic

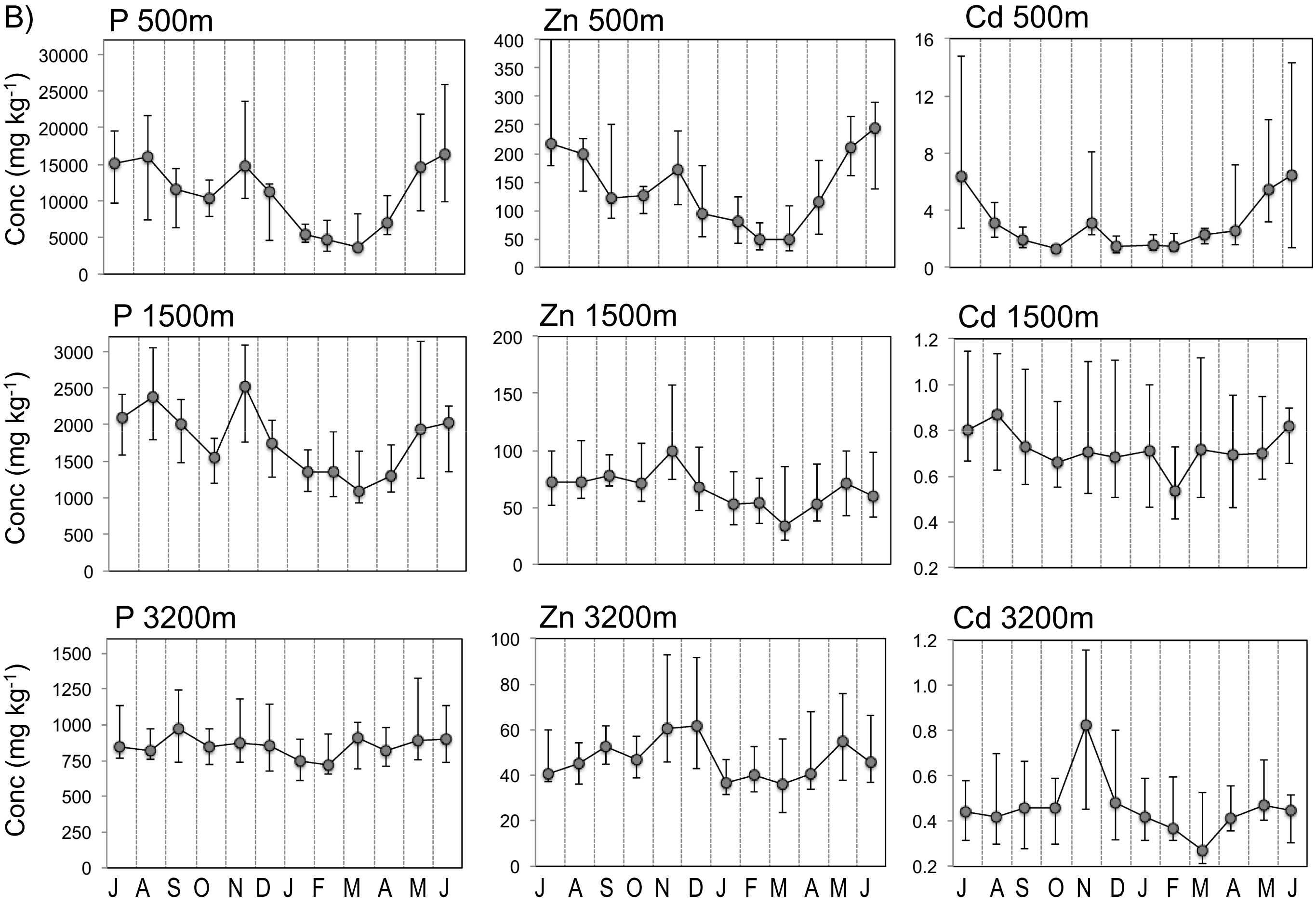

Fig. 6. (*continued*)

flux would be expected to decrease with depth as particles degrade and are disaggregated and recycled by animal grazing activity, whereas the intrinsic flux would be expected to become a larger contributor to the flux due to the repeated cycles of suspended particle aggregation within the water column.

Lithogenic elements also evidence aggregation of suspended particles (e.g. clays) within the deep water column and indicate a background of intrinsic flux generation. In contrast to biogenic elements, lithogenic element fluxes in the deep water column shown only a weak seasonal cycle, indicating that the deep water intrinsic flux generation via suspended particle aggregation remains relatively constant throughout the year. This constancy would dampen the seasonal variation in deep intrinsic carbonate fluxes and also explain why carbonate fluxes at 1500 m and 3200 m depths are higher than at 500 m depth in summer and fall when overlying productivity, and extrinsic fluxes, is at a minimum.

Even so, there is a small but significant late winter–spring maximum in lithogenic element fluxes in the deep water column (Figs. 3c, 4c) indicating that intrinsic flux generation varies in phase with overlying productivity and export. Jickells et al. (1984) first noted a seasonal cycle in Al and Fe fluxes in the 3200 m trap that corresponded to the seasonal cycle in overlying production. Observations of aggregated fly-ash particles in the 3200 m flux (Deuser et al., 1983a) further reinforced the conclusion that zooplankton grazing activity and production of large biogenic particles (fecal pellets, aggregates, marine snow etc.) exerts a major control on removal of non-biogenic material from the water column (Deuser et al., 1983b). Physical processes such as sticky particle encounters and coagulation, and DOM polymeric self-assembly can generate large particles (e.g. Burd, 2013 and references therein). However, given the low particle and DOM concentrations in the deep water column, passive physical aggregation would be expected to be of minor importance relative to active biological aggregation by zooplankton. In particular, mesopelagic and bathypelagic filter-feeding gelatinous zooplankton (e.g. Youngbluth et al., 2008; Robison et al., 2010) can have a pronounced impact on suspended particle aggregation and intrinsic flux generation due to their exceptionally high clearance rates, particle retention efficiencies and large particle production (e.g. Gorsky and Feneaux, 1998; Madin and Deibel, 1998; Katija et al., 2017). The higher intrinsic fluxes observed in spring suggest a seasonal modulation of particle aggregation rates (e.g. Conte et al., 2001, 2003), possibly arising from a co-variation in the seasonal cycle of deep-dwelling zooplankton populations (and their grazing pressure) and/or higher grazing rates in spring when phytodetritus flux, and particle food quality, increases. Additionally, higher particle densities in spring

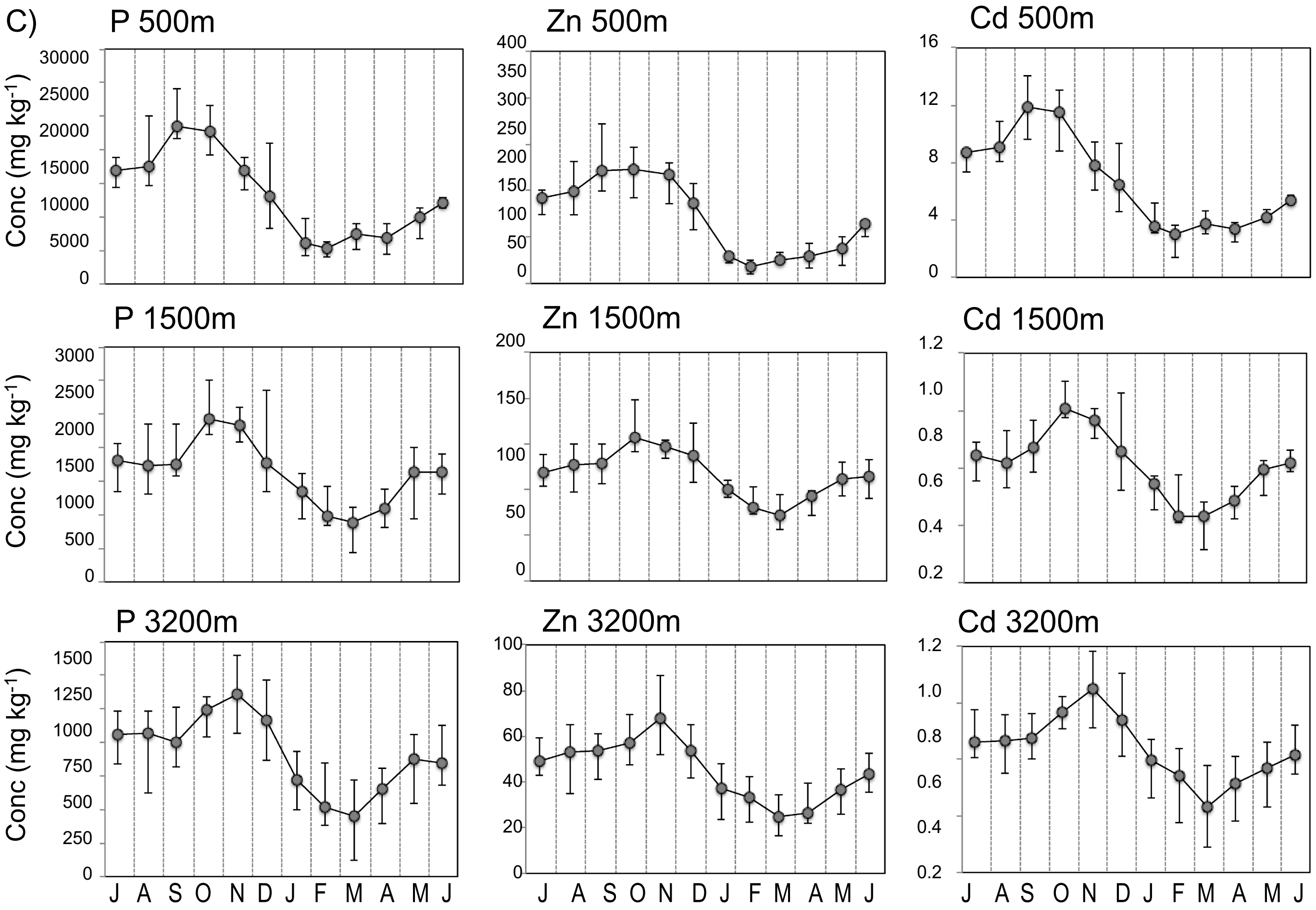

Fig. 6. (*continued*)

and possibly greater stickiness of decomposing organic matrices may also increase physical aggregation rates.

The data provide little evidence of direct coupling between atmospheric dust deposition and deep fluxes. Although lithogenic element concentrations (Figs. 5c, 6c) are enriched in the fall at the end of the dust deposition season, consistent with the upper water column enrichment in Fe and other dust-derived elements in the summer–fall (e.g. Sedwick et al., 2005), the seasonal cycle in lithogenic element fluxes is clearly not in phase with the late summer-fall season of Saharan dust deposition at Bermuda (Arimoto et al., 2003; Tian et al., 2008). There are only three years over the entire time-series (2003, 2005 and 2006) that suggest any direct temporal coupling between dust deposition and lithogenic flux at 500 m depth (Fig. 3c), and even these events are no longer distinctive by 1500 m depth. Rather, as discussed below in Section 5.2, the results indicate that the main source of the deep lithogenic flux at Bermuda is laterally-advected North American continental margin sediments which are then aggregated by intrinsic flux generation processes within the water column.

The seasonal cycle in flux composition (Figs. 5, 6) reflects dilution of lithogenic and authigenic phases in the late winter to early spring with biogenic material originating from overlying surface water production and export (the extrinsic flux). The Dec-Jan onset of increasing extrinsic fluxes coincides with the secondary peak that is observed in the mass flux (Conte et al., 2001). Early winter is the period of mixed layer destratification at Bermuda, which is characterized by alternating periods of weak mixed layer stability followed by mixed layer erosion and nutrient upwelling, leading to transient episodes of primary production followed by down-mixing (e.g. Stramska et al., 1995; Koeve et al., 2002; Lomas et al., 2009; Thomsen et al., 2017) The observation of increasing export fluxes at the onset of destratification supports a growing body of observations that suggests flux export efficiency is enhanced when mixed layer stability is low and variable (Koeve et al., 2002; Conte et al., 1998, 2003; Thomsen et al., 2017).

Element concentration data (Table 3) provide insights on factors that contribute to flux compositional variability. Concentrations of nutrient elements associated with organic material are far more variable in the flux (e.g. Q-ranges of P, Zn and Cd of 68%, 87%, and 65%, respectively in the 1500 m flux) than are concentrations of elements that are associated with carbonates (e.g. Q-ranges of Ca, Mg and Sr of 17%, 34%, and 15%, respectively). This likely reflects the limited compositional range of skeletal carbonates in comparison to the wide range in the composition of organic phases, which can be sourced from

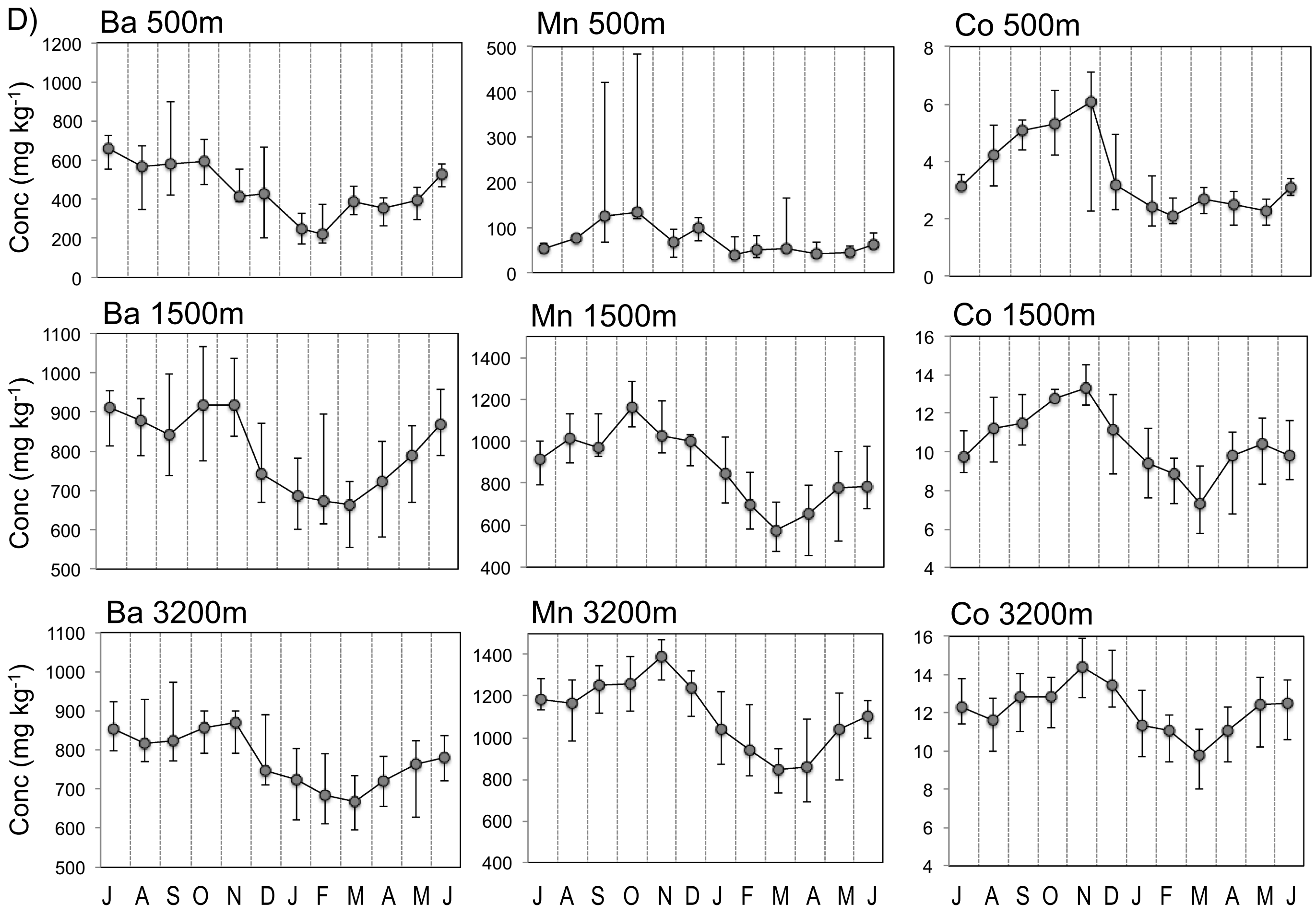

Fig. 6. (*continued*)

fresh, labile organic materials, zooplankton and microbial biomass, fecal pellets, etc. The compositional variability of lithogenic elements in the 1500 m flux (Q-range for Al, Sc and Ti of 41%, 39% and 47%, respectively) is intermediate between nutrient and carbonate elements, and suggests a limited range of lithogenic phases in the deep flux and/or that the lithogenic particle composition is effectively homogenized during deep water transport. This conclusion is also indicated by the low variability seen in lithogenic element ratios (Q-ranges < 20%) in the 1500 m and 3200 m fluxes.

The data also evidence significant interannual variability in the seasonal cycles of deep elemental fluxes. This variability partly arises from interannual variability in the overlying productivity (e.g. Steinberg et al., 2001; Lomas et al., 2013), which drives extrinsic flux patterns. However, the interannual variability in the 1500 m and 3200 m flux data also suggests variability in intrinsic flux generation within the deep water column. One possibility is that temporal variations in suspended particle concentrations and/or composition of deep water masses affects rates of chemical scavenging (e.g. Honeyman et al., 1988) and particle aggregation. Alternatively, there may be variability in deep water zooplankton populations and/or grazing pressure that might affect particle recycling and rates of biological aggregation of suspended material.

5.2. Lithogenic fluxes

Although Saharan dust deposition contributes significant amounts of lithogenic material to the region, the four-fold increase in the lithogenic element fluxes between 500 m and 3200 m depth at the OFP site clearly cannot be supported by aeolian dust deposition and indicates that there is a significant source from deep water lateral advection. The similarities in elemental ratios (Ti/Al, Fe/Ti) in the deep flux (Table 3) with suspended particles collected along the western North Atlantic margin (Ohnemus and Lam, 2015) provides strong evidence that the primary source of the deep lithogenic material is North American continental slope sediments that have been advected to the region by deep water currents. This conclusion is supported by the topographic divide found in the clay mineralogy of surface sediments to the east and west of the Mid Atlantic ridge (Biscaye, 1965), a feature that cannot be produced via aeolian deposition.

Resuspension of North American continental slope sediments and

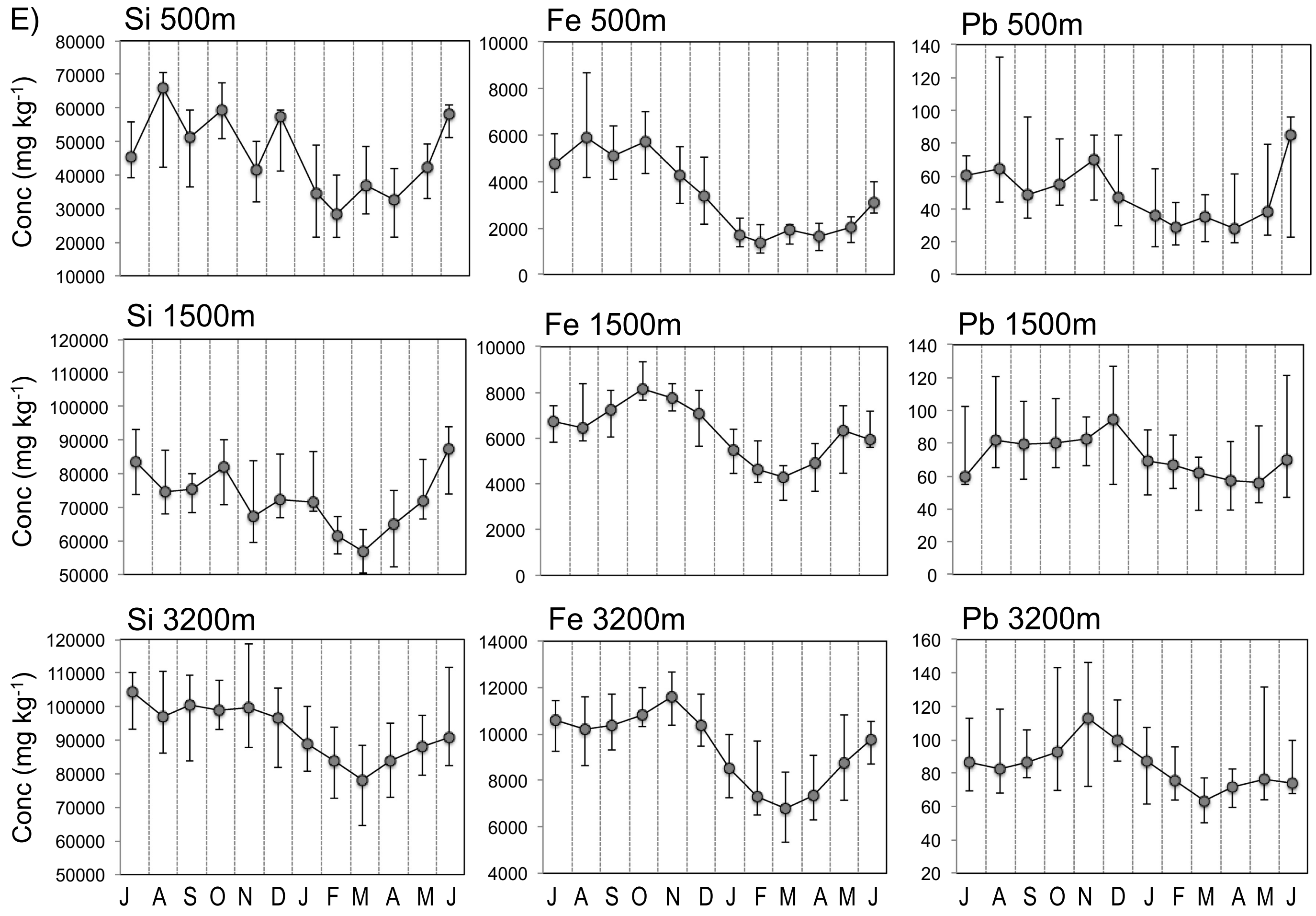

Fig. 6. (*continued*)

their transport to the western North Atlantic is well documented. Energy associated with Gulf Stream meanders and eddies propagates downward and periodically generates strong currents that resuspend seafloor sediments and create benthic storms along the continental US margin (reviewed in Gardner et al., 2017). Elevated suspended particle concentrations are a characteristic feature of western North Atlantic deep waters (Biscaye and Eittreim, 1977; Biscaye et al., 1988; Gardner et al., 2017). High concentrations of suspended particulate lithogenic elements have also been observed at midwater depths along the Line W transect from Cape Cod to Bermuda (Ohnemus and Lam, 2015), providing additional evidence for lateral transport of sediments resuspended by boundary current/slope interactions. Our results confirm earlier indications (Jickells et al., 1987; Huang and Conte, 2009) that the northwestern Sargasso Sea is a strong sink area for North American continental margin sediments advected into the North Atlantic gyre via Gulf Stream circulation.

5.3. *Authigenic mineralization*

The striking enrichment in concentrations of Mn in the particle flux with increasing depth (Table 3) indicates the significant production of authigenic Mn oxides by marine Mn-oxidizing bacteria (Nealson et al., 1988; Tebo et al., 2004; Bargar et al., 2005) in the mesopelagic. Mn oxides are well known to scavenge many elements, either via co-precipitation or adsorption (reviewed in Jeandel et al., 2015). The strong associations of excess concentrations of Fe, Co, Ni, V, Cr, and Pb with those of Mn in the 1500 m and 3200 m flux (Fig. 10) confirms the key role of authigenic Mn oxides in elemental scavenging and clearly show that Mn oxides are a major flux carrier phase for many elements in the deep water column. The increases in element enrichment factors (EFs) with depth is consistent with water column profiles of particulate Mn, Co, Zn, Cu, Ni and Pb at Bermuda that suggest uptake of these elements from the dissolved pool by Mn oxide scavenging (Sherrell and Boyle, 1992).

An interesting observation is the differences in the composition of Mn oxides at 1500 m and 3200 m depths, in particular the enrichments of Fe, Cu and V in the 3200 m flux (Figs. 8, 9). If Mn oxide scavenging is nonselective, i.e. it is a function of dissolved element concentrations, then this enrichment is rather enigmatic given the relatively constant concentrations in dissolved Fe, Cu and V in the deep water column. One hypothesis is that pressure and/or other depth related variables affect Mn- (and Fe-) oxidizing bacterial community composition and/or alter

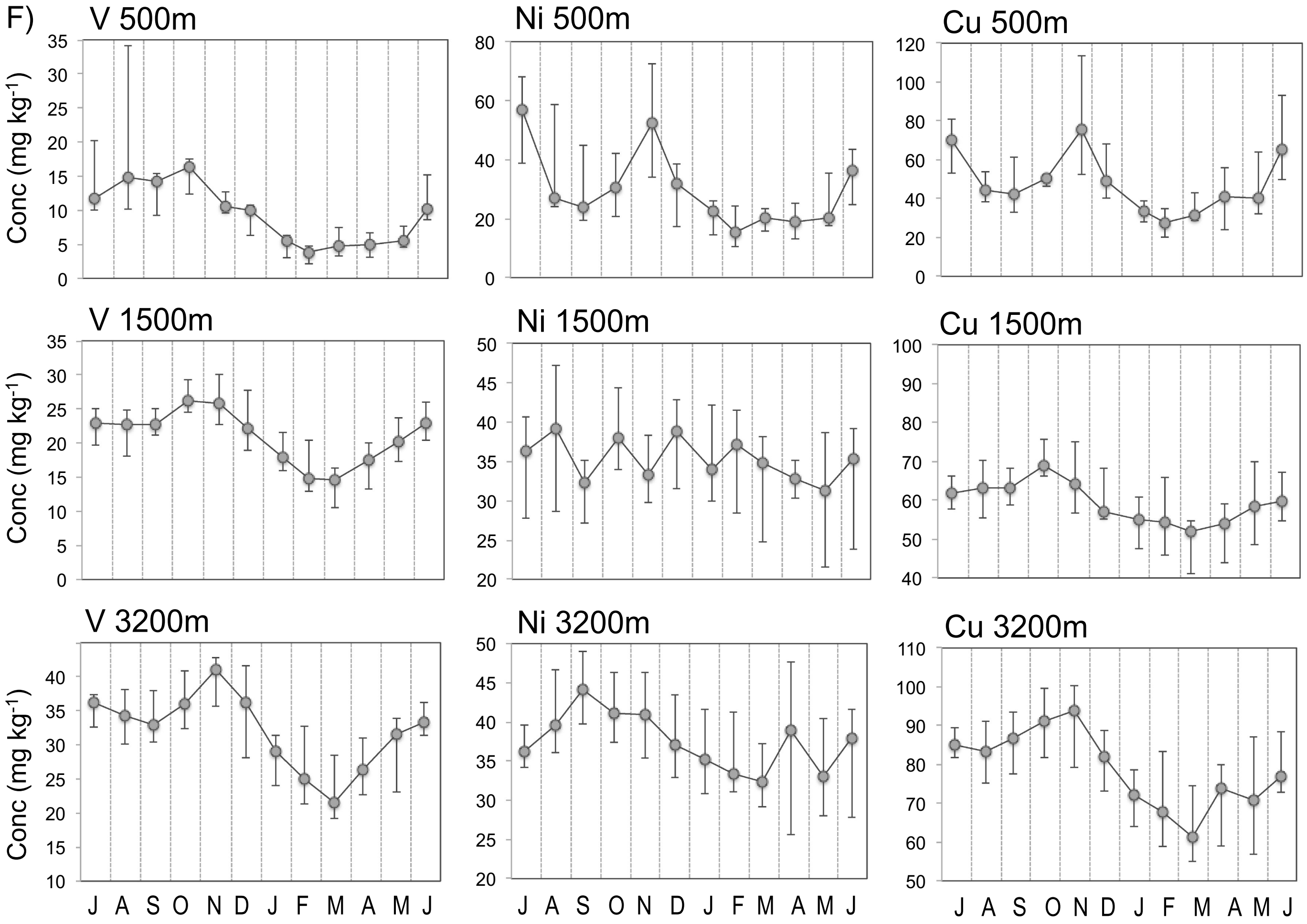

Fig. 6. (*continued*)

the mineral structure of the precipitated Mn oxides (e.g. Bargar et al., 2005). Alternatively, there may be compositional differences in advected sources at the two depths. The data do not allow us to distinguish the fraction of the authigenic signature generated locally from that contributed by Mn oxides associated with advected materials (c.f. Lam et al., 2015) to evaluate these hypotheses.

The large increase in Ba_{xs} concentration between 500 m and 1500 m provides further evidence that significant barite is produced in the mesopelagic (Van Beek et al., 2007). Although some Ba_{xs} may be associated with organic matter, opal, Mn/Fe oxyhydr(oxides) or other mineral phases such as rutile (Gonneea and Paytan, 2006; Griffith and Paytan, 2012), the strong Ba flux seasonality at 500 m depth (Fig. 3d) indicates that Ba_{xs} is associated with the export flux of phytodetritus, consistent with barite precipitation in microenvironments in decaying organic matter (Bishop, 1988).

In contrast to Mn_{xs}, there is no increase in Ba_{xs} flux or concentration between 1500 m and 3200 m depths (Tables 2 and 3), indicating that barite production is negligible in the deep water column. The flux and concentration increases observed between 1500 m and 3200 m for lithogenic elements and Mn_{xs}, but not for Ba_{xs}, also argue against non-silicate lithogenic minerals or Mn oxides (Gonneea and Paytan, 2006) as major flux carrier phases for Ba_{xs}. The data here do not allow us to distinguish between local precipitation and deep water scavenging of suspended barite particles produced elsewhere and advected to the region. However, the significant Ba_{xs} flux observed throughout the summer-fall period of minimum surface water productivity suggests that there is a significant intrinsic flux component for Ba_{xs} in addition to local production.

5.4. Evolution in elemental flux carrier phases with depth

Trends in elemental composition with depth highlight the evolving elemental composition of the particle flux. The sinking flux material rapidly becomes depleted in organic matter and associated elements (N, P, Cd, Zn) while becoming more enriched in lithogenic materials, authigenic minerals such as barite, and redox sensitive elements (Mn, Co, V, Fe) that are scavenged via the formation of oxide and hydroxide coatings on particles (Table 3). The observed changes in elemental fluxes (Figs. 3, 4) and in flux composition (Figs. 5, 6) are especially pronounced between 500 and 1500 m and provide further evidence of the importance of mesopelagic processes in controlling deep particle flux composition.

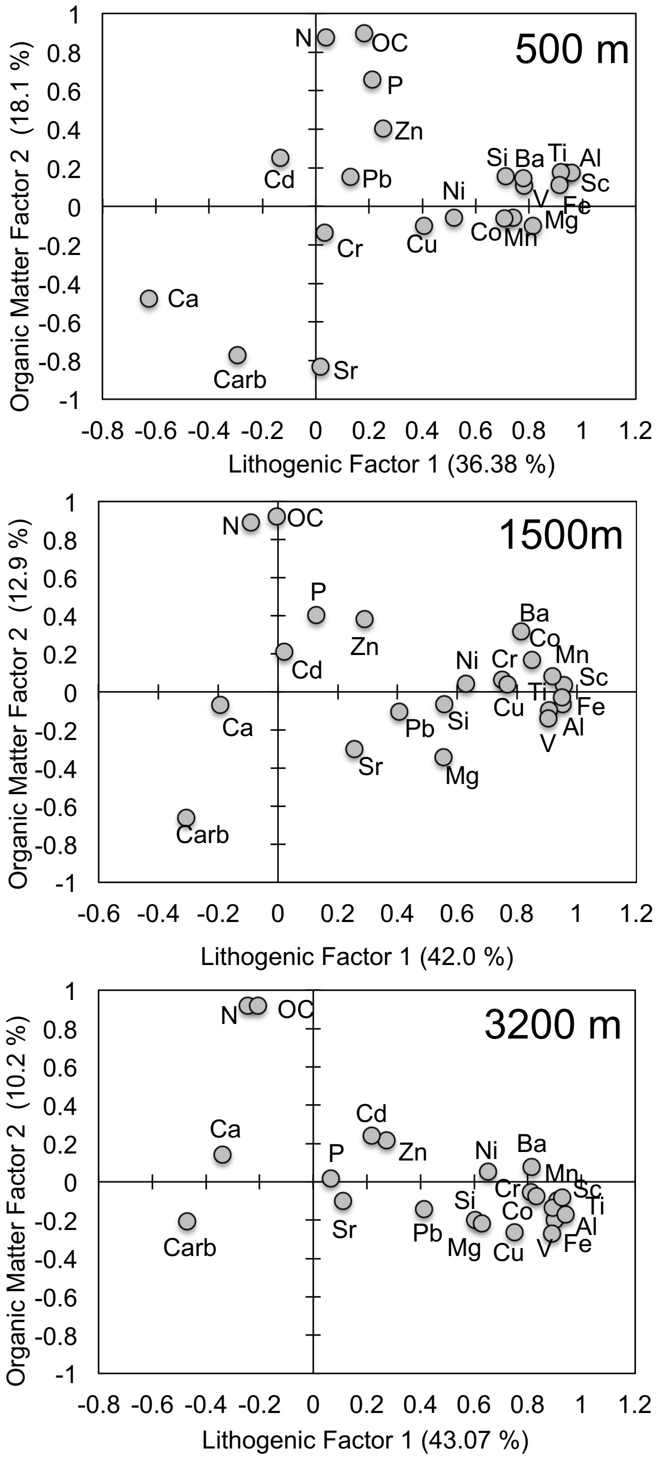

Fig. 7. Principal component loadings for total element concentrations on Factor 1 (“lithogenic”) versus Factor 2 (“organic matter”) in the flux at (a) 500 m, (b) 1500 m and (c) 3200 m depths.

The results clearly indicate major reorganizations of elemental associations with depth. In the upper mesopelagic, the geochemical behavior of many trace elements such as Zn, Cu Ni and Co that are incorporated into phytoplankton cellular materials (Morel and Price, 2003; Twining et al., 2015) is closely tied to organic matter flux and rates of organic carbon remineralization. For example, PCA factor loadings of excess concentrations indicate primary associations of P, Zn and Cd with organic matter at 500 m depth, and also significant associations of Ni and Cu with organic matter (Fig. 8). As labile organic carrier phases break down, elements that are initially associated with labile organic matrices (P, Cd, Zn, Co and Pb) show increasingly independent behavior relative to that of organic matter. By 1500 m depth, only P, Zn and Cd remain associated with organic matter. By 3200 m depth, P is no longer associated with organic matter and Zn and Cd associations are weak (Fig. 9). The data clearly show that with increasing depth, co-precipitation and/or scavenging of dissolved elements onto Mn oxide coatings on particles is an increasingly important process that controls the removal of many elements from the water column.

Table 4
Elemental enrichment factors (EF) in the particle flux relative to the composition of the upper continental crust (UCC, Rudnick and Gao, 2003). Median values over the time series are shown. Extreme fluxes from Hurricane Fabian and Igor plumes are not included in statistics.

	Depth		
	500 m	1500 m	3200 m
Mg	6.2	3.6	2.7
Si	3.0	2.1	1.9
P	323	25	9
Ca	205	95	62
Sc	1.1	1.0	0.9
Ti	1.2	1.1	1.1
V	1.6	2.0	2.2
Cr	2.3	1.2	1.2
Mn	2.2	10.4	9.2
Fe	1.5	1.5	1.6
Co	4.3	5.5	4.6
Ni	13	7	5
Cu	38	20	18
Zn	42	9	4
Sr	111	52	34
Cd	691	75	32
Ba	15	12	8
Pb	65	38	31

6. Conclusions and implications

The time-series of particulate elemental fluxes at the OFP site in the northern Sargasso Sea underscores the close linkage between the deep flux and the seasonal cycle of primary production and export in overlying surface waters. The deep flux elemental composition reflects seasonal variations in the relative strengths of two deep flux components: the first sourced from overlying surface water production and export (the “extrinsic” flux), and the second sourced from chemical scavenging and biological aggregation of suspended particles within the water column (the “intrinsic” flux). The late winter - spring maxima in deep water fluxes of elements associated with lithogenic and authigenic phases indicates that intrinsic flux generation varies in phase with export flux from overlying production, suggesting seasonal modulation in rates of particle aggregation.

There is a four-fold increase in the lithogenic flux between 500 m and 3200 m depth. The main source of the deep lithogenic flux material is North American continental margin material, rather than Saharan

Table 5

"Excess" fluxes (X_{xs}, in μg m^{-2} d^{-1}), concentrations ($[X]_{XS}$, in mg kg^{-1}) and lithogenic fraction (%lith) in the 500 m, 1500 m and 3200 m flux. Estimates use a first order assumption that the elemental composition of the lithogenic material approximates that of the upper continental crust (UCC, Rudnick and Gao, 2003). Median values over the time series are shown. Extreme fluxes from Hurricane Fabian and Igor plumes are not included in statistics.

Element	Depth								
	500 m			1500 m			3200 m		
	X_{xs} flux	$[X]_{XS}$	%lith	X_{xs} flux	$[X]_{XS}$	%lith	X_{xs} flux	$[X]_{XS}$	%lith
Mg	63	3393	18	143	4042	30	130	3871	40
Si (ppt)	536	25,907	40	1180	36,568	49	1438	41,664	54
P	186	8618	< 1	59	1639	4	26	734	13
Ca (ppt)	4948	250	1	8358	254	1	7963	241	2
Sc	0	0	94	0	0	100	0	0	100
Ti	0	29	84	1.5	47	90	1.5	42	93
V	0.1	3	59	0.3	10	51	0.6	17	48
Cr	0	3	73	0.1	2	80	0.1	3	82
Mn	0.6	28	54	26	809	10	34	1016	10
Fe	19	862	66	65	2029	67	111	3380	65
Co	0.04	2	20	0.3	9	18	0.3	9	24
Ni	0.4	22	6	0.9	29	16	1.0	30	20
Cu	0.9	40	2	1.9	56	5	2.6	75	6
Zn	2.1	117	< 1	1.8	59	13	1.2	35	23
Sr	33	1573	1	58	1753	2	55	1635	3
Cd	0.5	2.3	< 1	0.03	0.7	1	0.01	0.4	3
Ba	7.2	381	7	24.5	732	8	23.3	676	13
Pb	0.8	44	< 1	2.3	68	2	2.9	78	4

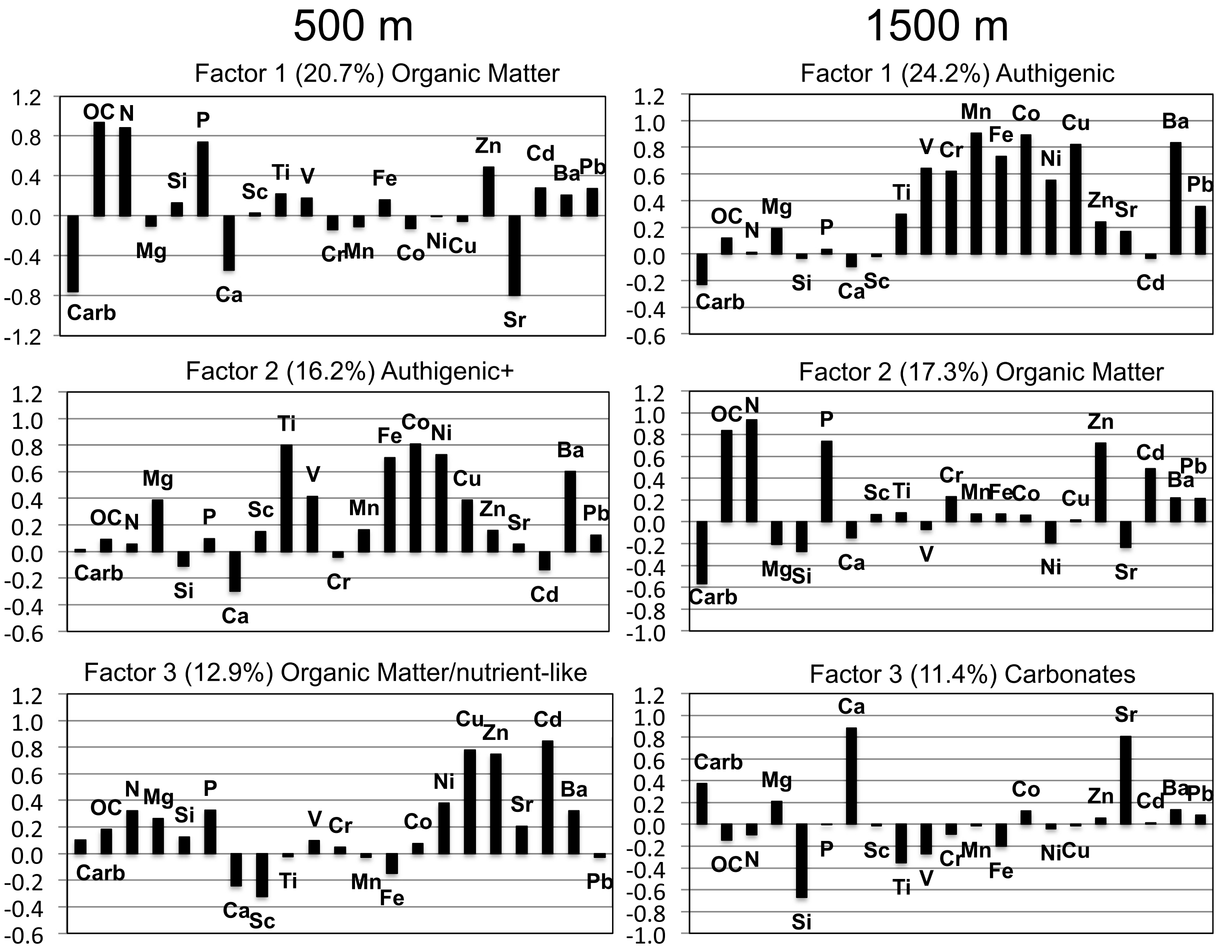
500 m

1500 m

Factor 1 (20.7%) Organic Matter

Factor 1 (24.2%) Authigenic

Factor 2 (16.2%) Authigenic+

Factor 2 (17.3%) Organic Matter

Factor 3 (12.9%) Organic Matter/nutrient-like

Factor 3 (11.4%) Carbonates

Fig. 8. Principal component factor loadings for excess elemental concentrations ($[X]_{xs}$) in the 500 m and 1500 m flux. $[X]_{xs}$ calculations assume the elemental composition of the lithogenic flux material approximates that of the upper continental crust (UCC, Rudnick and Gao, 2003).

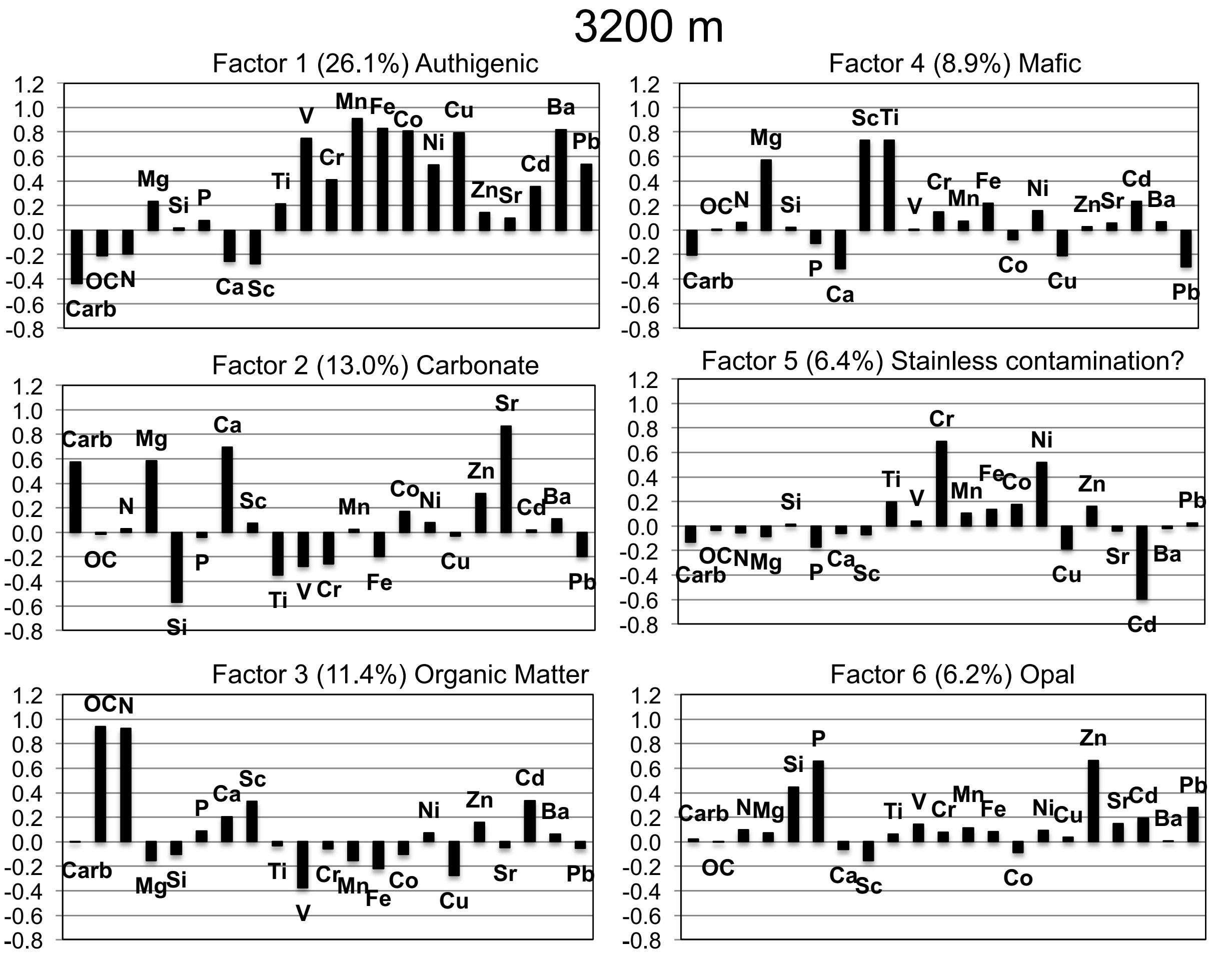

Fig. 9. Principal component factor loadings for elemental excess concentrations ($[X]_{xs}$) in the 3200 m flux.

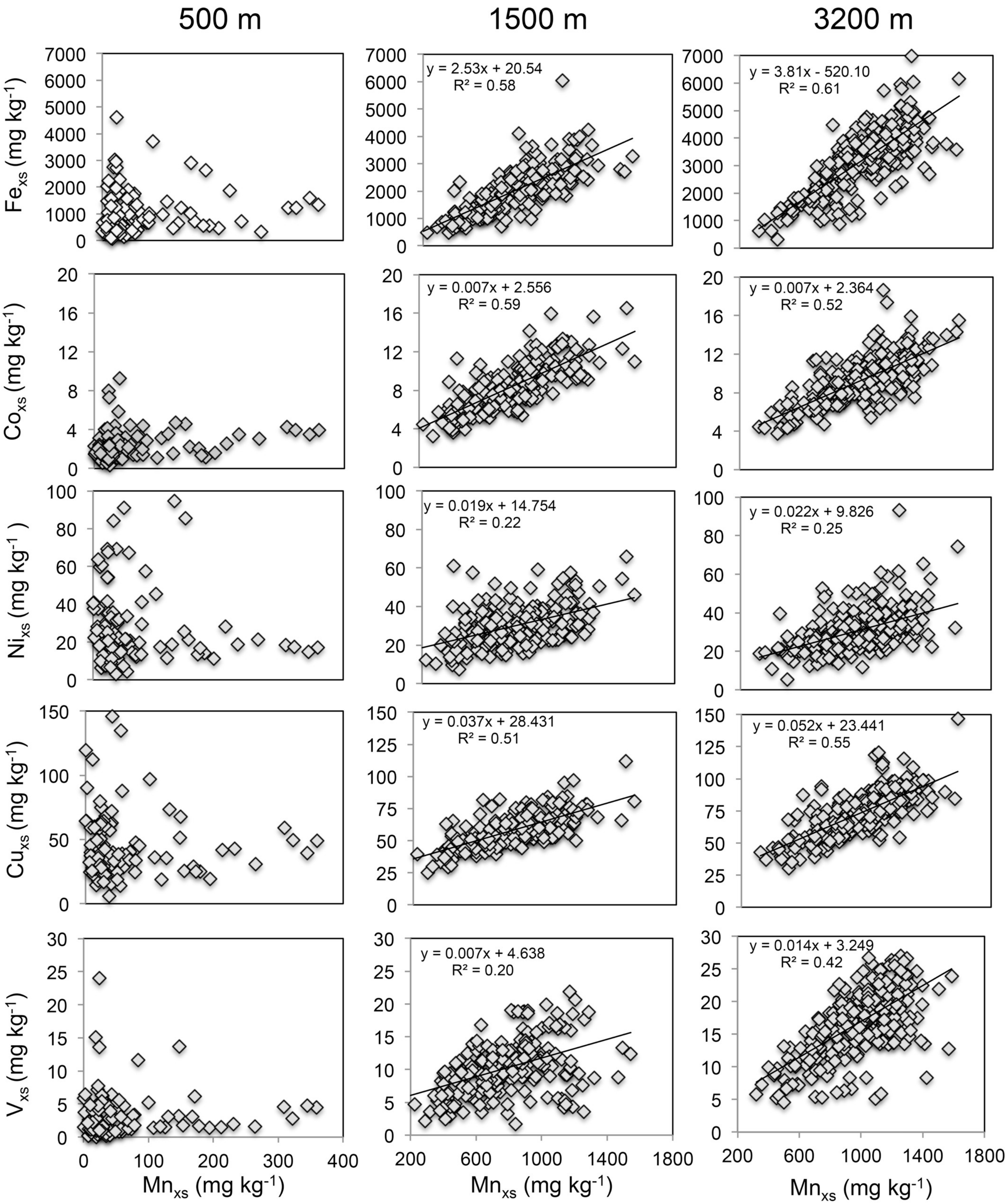

Fig. 10. Elemental excess concentrations ($[X]_{xs}$) of Fe, Co, Ni, Cu and V versus Mn in the particle flux in the 500 m, 1500 m and 3200 m flux.

dust. The results confirm that the region is a significant sink for resuspended continental slope sediments that are advected into the western North Atlantic gyre via Gulf Stream circulation.

High rates of authigenic mineralization accompany high rates of organic matter remineralization within the mesopelagic ocean. There are major reorganizations of element associations with flux carrier phases with depth. In particular, the geochemical behavior and flux of P becomes increasing independent of organic flux carrier phases, while that of Co, Ni, Cu and, to a lesser extent, V and Cr become increasingly controlled by scavenging onto magnesian oxides.

Acknowledgements

This work and the OFP time-series were supported by the Chemical Oceanography Program of the National Science Foundation by grants OCE 0509602, OCE 0623505, OCE 092285, OCE 1234294 and OCE 1536644. We thank J. Freidman, K. Garrison, A. Gaylord, A. Toltin, R. Franzblau, and B. Siranosian for assistance with sample processing and bulk analyses. We thank J. Aucan, D. Bean, W. Burton, M. Enright, M. Gonsior, D. Grundle, W. Halliday, H. Masters, R. Johnson, J. Ryder and the crews of the R/V Weatherbird and R/V Atlantic Explorer for mooring assistance at sea. We thank anonymous reviewers for constructive comments on the manuscript.

Declarations of interest

None.

Appendix A. Supplementary data

Supplementary data to this article can be found online at https://doi.org/10.1016/j.chemgeo.2018.11.001.

References

Arimoto, R., Duce, R.A., Ray, B.J., Ellis, W.G.Jr., Cullen, J.D., Merrill, J.T., 1995. Trace elements in the atmosphere over the North Atlantic. J. Geophys. Res. 100, 1199–1213. https://doi.org/10.1029/94JD02618.

Arimoto, R., Duce, R.A., Ray, B.J., Tomza, U., 2003. Dry deposition of trace elements to the western North Atlantic. Glob. Biogeochem. Cycles 17. https://doi.org/10.1029/2001GB001406.

Balistrieri, L., Brewer, P.G., Murray, J.W., 1981. Scavenging residence times of trace metals and surface chemistry of sinking particles in the deep ocean. Deep Sea Res. Part A 28, 101–121. https://doi.org/10.1016/0198-0149(81)90085-6.

Bargar, J.R., Webb, S.M., Tebo, B.M., 2005. EXAFS, XANES and in-Situ SR-XRD characterization of biogenic manganese oxides produced in sea water. Phys. Scr. T115, 888–890.

Biscaye, P.E., 1965. Mineralogy and sedimentation of recent deep-sea clay in the Atlantic Ocean and adjacent seas and oceans. Geol. Soc. Am. Bull. 76, 803–832.

Biscaye, P.E., Eittreim, C.E., 1977. Suspended particulate loads in the nepheloid layer of the abyssal Atlantic Ocean. Mar. Geol. 22, 155–172.

Biscaye, P.E., Anderson, R.F., Deck, B.L., 1988. Fluxes of particles and constituents to the eastern United States continental slope and rise: SEEP-I. Cont. Shelf Res. 8, 855–904.

Bishop, J.K.B., 1988. The barite-opal-organic carbon association in oceanic particulate matter. Nature 332, 341–343.

Bruland, K.W., Lohan, M.C., 2003. Controls on trace metals in seawater. In: Turekian, K.K., Holland, H.D. (Eds.), Treatise on Geochemistry. 6. pp. 23–47.

Burd, A.B., 2013. Modeling particle aggregation using size class and size spectrum approaches. J. Geophys. Res. Oceans 118, 3431–3442. https://doi.org/10.1022/jgrc.20255.

Calvert, S.E., Piper, D.Z., Thunell, R.C., Astor, Y., 2015. Elemental settling and burial fluxes in the Cariaco Basin. Mar. Chem. 177, 607–629. https://doi.org/10.1016/j.marchem.2015.10.001.

Carter, A.M., Conte, M.H., Weber, J.C., Shaw, L., 2016. Phosphorus phase associations in the deep ocean particle flux in the Sargasso Sea. In: AGU/ASLO Ocean Sciences Meeting, Abst. CT24A-0157.

Carvalho, R.A., Benfield, M.C., Santschi, P.H., 1999. Comparative bioaccumulation studies of colloidally complexed and free-ionic heavy metals in juvenile brown shrimp *Penaeus aztecus* (Crustacea: Decapoda: Penaeidae). Limnol. Oceanogr. 44, 403–414.

Clegg, S.L., Sarmiento, J.L., 1989. The hydrolytic scavenging of metal ions by marine particulate matter. Prog. Oceanogr. 23, 1–21.

Collier, R., Edmond, J., 1984. The trace element geochemistry of marine biogenic particulate matter. Prog. Oceanogr. 13, 113–199.

Conte, M., Weber, J.C., 2014. Particle flux in the deep Sargasso Sea: the 35 year Oceanic Flux Program time series. Oceanography 27, 142–147.

Conte, M.H., Weber, J.C., Ralph, N., 1998. Episodic particle flux in the deep Sargasso Sea: an organic geochemical assessment. Deep-Sea Res. I 45, 1819–1841.

Conte, M.H., Ralph, N., Ross, E.H., 2001. Seasonal and interannual variability in deep ocean particle fluxes at the Oceanic Flux Program/Bermuda Atlantic Time-series (BATS) site in the western Sargasso Sea near Bermuda. Deep Sea Res., Part II 48, 1471–1505.

Conte, M.H., Dickey, T.D., Weber, J.C., Johnson, R.J., Knap, A.H., 2003. Transient physical forcing of pulsed export of bioreactive organic material to the deep Sargasso Sea. Deep Sea Res., Part I 50, 1157–1187.

Cowen, J.P., 1992. Morphological study of marine bacterial capsules: implications for marine aggregates. Mar. Biol. 114, 85–95.

Cowen, J.P., Bruland, K.W., 1985. Metal deposits associated with bacteria: implications for Fe and Mn marine biogeochemistry. Deep-Sea Res. 32, 253–272.

Cullen, J.T., Maldonado, M.T., 2013. Biogeochemistry of cadmium and its release to the environment. In: Sigel, A., Sigel, H., Sigel, R.K.O. (Eds.), Cadmium: From Toxicity to Essentiality, Metal Ions in Life Sciences. 11. pp. 32–58. https://doi.org/10.1007/978-94-007-5179-8_2.

Dall'Olmo, G., Dingle, J., Polimene, L., Brewin, R.J.W., Claustre, H., 2016. Substantial energy input to the mesopelagic ecosystem from the seasonal mixed-layer pump. Nat. Geosci. 9 (11), 820–823. https://doi.org/10.1038/ngeo2818.

Deuser, W.G., 1986. Seasonal and interannual variations in deep-water particle fluxes in the Sargasso Sea and their relation to surface hydrography. Deep-Sea Res. 33, 225–246.

Deuser, W.G., Emeis, K., Ittekkot, V., Degens, E.T., 1983a. Fly-ash particles intercepted in the deep Sargasso Sea. Nature 305, 216–218.

Deuser, W.G., Brewer, P.G., Jickells, J.D., Commeau, R.F., 1983b. Biological control of the removal of abiogenic particles from the surface ocean. Science 219, 388–391.

Deuser, W.G., Jickells, T.D., King, P., Commeau, J.A., 1995. Decadal and annual changes in biogenic opal and carbonate fluxes to the deep Sargasso Sea. Deep-Sea Res. I 42, 1923–1932.

Dickey, T., Zedler, S., Frye, D., Jannasch, H., Manov, D., Sigurdson, D., McNeil, J.D., Dobeck, L., Yu, X., Gilboy, T., Bravo, C., Doney, S.C., Siegel, D.A., Nelson, N., 2001. Physical and biogeochemical variability from hours to years at the Bermuda Testbed Mooring site: June 1994–March 1998. Deep-Sea Res. II 48, 2105–2140.

Dymond, J., Collier, R., McManus, J., Honjo, S., Manganini, S., 1997. Can the aluminum and titanium contents of ocean sediments be used to determine the paleoproductivity of the oceans? Paleoceanography 12, 586–593. https://doi.org/10.1029/97PA01135.

Ellwood, M.J., Hunter, K.A., 2000. The incorporation of zinc and iron into the frustule of the marine diatom *Thalassiosira pseudonana*. Limnol. Oceanogr. 45, 1517–1524. https://doi.org/10.4319/lo.2000.45.7.1517.

Fisher, N.S., Wente, M., 1993. The release of trace elements by dying phytoplankton. Deep-Sea Res. I (40), 671–694.

Gardner, W.D., Tucholke, B.E., Richardson, M.J., Biscaye, P.E., 2017. Benthic storms, nepheloid layers, and linkage with upper ocean dynamics in the western North Atlantic. Mar. Geol. 385, 304–327. https://doi.org/10.1016/j.margeo.2016.12.012.

Gehlen, M., Beck, L., Calas, G., van Beusekom, J.E.E., 2002. Unraveling the atomic structure of biogenic silica: evidence of the structural association of Al and Si in diatom frustules. Geochim. Cosmochim. Acta 66, 1601–1609. https://doi.org/10.1016/S0016-7037(01)00877-8.

Gonneea, M.E., Paytan, A., 2006. Phase associations of barium in marine sediments. Mar. Chem. 100, 124–135.

Gorsky, G., Feneaux, R., 1998. The role of Appendicularia in marine food webs. In: Bone, Q. (Ed.), The Biology of Pelagic Tunicates. Oxford Univ Press, New York, pp. 161–169.

Griffith, E.M., Paytan, A., 2012. Barite in the ocean – occurrence, geochemistry and palaeoceanographic applications. Sedimentology 59, 1817–1835. https://doi.org/10.1111/j.1365–3091.2012.01327.

Gunnars, A., Blomquist, S., Johansson, P., Andersson, C., 2002. Formation of Fe(III) oxyhydroxide colloids in freshwater and brackish seawater, with incorporation of phosphate and calcium. Geochim. Cosmochim. Acta 66, 745–758.

Hawco, N.J., Lam, P.J., Lee, J.-M., Ohnemus, D.C., Noble, A.E., Wyatt, N.J., Lohan, M.C., Saito, M.A., 2018. Cobalt scavenging in the mesopelagic ocean and its influence on global mass balance: synthesizing water column and sedimentary fluxes. Mar. Chem. 201, 151–166. https://doi.org/10.1016/j.marchem.2017.09.001.

Honeyman, B.D., Balistrieri, L.S., Murray, J.W., 1988. Oceanic trace metal scavenging: the importance of particle concentration. Deep Sea Res. Part A 35, 227–246. https://doi.org/10.1016/0198-0149(88)90038-6.

Huang, S., Conte, M.H., 2009. Source/process apportionment of major and trace elements in sinking particles in the Sargasso Sea. Geochim. Cosmochim. Acta 73, 65–90.

Huang, S., Rahn, K.A., Arimoto, R., 1999. Semiannual cycles of pollution at Bermuda. J. Geophys. Res. 104, 30309–30318.

Huang, S., Sholkovitz, E.R., Conte, M.H., 2007. Application of high-temperature fusion for analysis of major and trace elements in marine sediment trap samples. Limnol. Oceanogr. Methods 5, 13–22.

Iyer, A., Mody, K., Jha, B., 2004. Accumulation of hexavalent chromium by an exopolysaccharide producing marine Enterobacter cloaceae. Mar. Pollut. Bull. 49, 974–977.

Jeandel, C., Rutgers van der Loeff, M., Lam, P.J., Roy-Barman, M., Sherrell, R.M., Kretschmer, S., German, C., Dehairs, F., 2015. What did we learn about ocean particle dynamics in the GEOSECS–JGOFS era? Prog. Oceanogr. 133, 6–16.

Jickells, T.D., Deuser, W.G., Knap, A.H., 1984. The sedimentation rates of trace elements in the Sargasso Sea measured by sediment trap. Deep-Sea Res. 31, 1169–1178.

Jickells, T.D., Church, T.M., Deuser, W.G., 1987. A comparison of atmospheric inputs and deep-ocean particle fluxes for the Sargasso Sea. Glob. Biogeochem. Cycles 1, 117–130.

Jickells, T.D., Deuser, W.G., Fleer, A., Hemleben, C., 1990. Variability of some elemental fluxes in the western tropical Atlantic Ocean. Oceanol. Acta 13, 291–298.

Joyce, T.M., Robbins, P., 1996. The long-term hydrographic record at Bermuda. J. Clim. 3121–3131.

Katija, K., Sherlock, R.E., Sherman, A.D., Robison, B.H., 2017. New technology reveals the rople of giant larvaceans in oceanic carbon cycling. Sci. Adv. 3. https://doi.org/10.1126/sciadv.1602374.

Koeve, W., Pollehne, F., Oschlies, A., Zeitzschel, B., 2002. Storm-induced convective export of organic matter during spring in the northeast Atlantic Ocean. Deep-Sea Res. I 49, 1431–1444.

Krause, J.W., Nelson, D.M., Lomas, M.W., 2010. Production, dissolution, accumulation and potential export of biogenic silica in a Sargasso Sea mode-water eddy. Limnol. Oceanogr. 55, 569–579.

Kuss, J., Kremling, K., 1999a. Particulate trace element fluxes in the deep northeast Atlantic Ocean. Deep-Sea Res. I 46, 149–169.

Kuss, J., Kremling, K., 1999b. Spatial variability of particle associated trace elements in near-surface waters of the North Atlantic (30°N/60°W to 60°N/2°W), derived by large volume sampling. Mar. Chem. 68, 71–86.

Kuss, J., Waniek, J.J., Kremling, K., Schulz-Bull, D.E., 2010. Seasonality of particle-associated trace element fluxes in the deep northeast Atlantic Ocean. Deep-Sea Res. I 57, 785–796.

Lam, P., Ohnemus, D.C., Auro, M.E., 2015. Size-fractionated major particle composition and concentration from the US GEOTRACES North Atlantic Zonal Transect. Deep-Sea Res. II 116, 303–320.

Latimer, J.C., Filippelli, G.M., Hendry, I., Newkirk, D.R., 2006. Opal-associated particulate phosphorus: implications for the marine P cycle. Geochim. Cosmochim. Acta 70, 3843–3854. https://doi.org/10.1016/j.gca.2006.04.033.

Lee, B.-G., Fisher, N.S., 1992. Degradation and elemental release rates from phytoplankton debris and their geochemical implications. Limnol. Oceanogr. 37, 1345–1360.

Li, Y.-H., Shoonmaker, J.E., 2003. Chemical composition and mineralogy of marine sediments. In: Treatise on Geochemistry. vol. 7. pp. 1–64.

Lomas, M.W., Roberts, N., Lipschultz, F., Krause, J., Neloson, D.M., Bates, N.R., 2009. Biogeochemical responses to late-winter storms in the Sargasso Sea. IV. Rapid succession of major phytoplankton groups. Deep Sea Res., Part I 56, 892–908.

Lomas, M.W., Bates, N.R., Johnson, R.J., Knap, A.H., Steinberg, D.K., Carlson, C.A., 2013. Two decades and counting: 24 years of sustained open ocean biogeochemical measurements in the Sargasso Sea. Deep-Sea Res. II 93, 16–32.

Madin, L., Deibel, D., 1998. Feeding and energetics of Thaliaea. In: Bone, Q. (Ed.), The Biology of Pelagic Tunicates. Oxford Univ Press, New York, pp. 81–103.

Martin, J.H., Knauer, G.A., 1973. The elemental composition of plankton. Geochim. Cosmochim. Acta 37, 1639–1653.

McGillicuddy, D.J., Robinson, A.R., Siegel, D.A., Jannasch, H.W., Johnson, R., Dickey, T.D., McNeil, J., Michaels, A.F., Knap, A.H., 1998. Influence of mesoscale eddies on new production in the Sargasso Sea. Nature 394, 263–265.

McNeil, J.D., Jannasch, H., Dickey, T., McGillicuddy, D., Brzezinski, M., Sakamoto, C.M., 1999. New chemical, bio-optical, and physical observations of upper ocean response to the passage of a mesoscale eddy. J. Geophys. Res. 104, 15537–15548.

Michaels, A.F., Knap, A.H., 1996. Overview of the US JGOFS Bermuda Atlantic Time-series Study (BATS) and the Hydrostation S program. Deep-Sea Res. II 43, 157–198.

Moffett, J.W., Ho, J., 1996. Oxidation of cobalt and manganese in seawater via a common microbially catalyzed pathway. Geochim. Cosmochim. Acta 60, 3415–3424.

Morel, F.M.M., Price, N.M., 2003. The biogeochemical cycles of trace metals in the oceans. Science 300, 944–947.

Moreno, T., Querol, X., Castillo, S., Alastuey, A., Herrmann, L., Mounkaila, M., Elvira, J., Gibbons, W., 2006. Geochemical variations in Aeolian mineral particles from the Sahara-Sahel dust corridor. Chemosphere 65, 261–270.

Morse, J.W., Bender, M.L., 1990. Partition coefficients in calcite: examination of factors influencing the validity of experimental results and their application to natural systems. Chem. Geol. 82, 265–277.

Mortlock, R.A., Froelich, P.N., 1989. A simple method for the rapid determination of biogenic opal in pelagic marine sediments. Deep-Sea Res. 36, 1415–1426.

Nealson, K.H., Tebo, B.M., Rosson, R.A., 1988. Occurrence and mechanisms of microbial oxidation of manganese. Adv. Appl. Microbiol. 33, 279–318.

Nelson, Y.M., Lion, L.W., Shuler, M.L., Ghiorse, W.C., 2002. Effect of oxide formation mechanisms on lead adsorption by biogenic manganese hydr(oxides), iron hydr (oxides) and their mixtures. Environ. Sci. Technol. 36, 4215.

Ohnemus, D.C., Lam, P.J., 2015. Cycling of lithogenic marine particles in the US GEOTRACES North Atlantic transect. Deep-Sea Res. II 116, 283–302. https://doi.org/10.1016/j.dsr2.2014.11.019.

Passow, U., 2002. Transparent exopolymer particles (TEP) in aquatic environments. Prog. Oceanogr. 55, 287–333.

Phillips, H., Joyce, T., 2007. Bermuda's tale of two time series: Hydrostation S and BATS. J. Phys. Oceanogr. 37, 554–571.

Pohl, C., Hennings, U., 1999. The effect of redox processes on the partitioning of Cd, Pb, Cu, and Mn between dissolved and particulate phases in the Baltic Sea. Mar. Chem. 65, 41–53.

Pohl, C., Löffler, A., Hennings, U., 2004. A sediment trap flux-study for trace metals under seasonal aspects in the stratified Baltic Sea (Gotland Basin; 57°19,20′N; 20°03,00′E). Mar. Chem. 84, 143–160.

Price, N.M., Morell, F.M.M., 1990. Cadmium and cobalt substitution for zinc in a marine diatom. Nature 344, 658–660.

Reinfelder, J.R., Fisher, N.S., 1991. The assimilation of elements ingested by marine copepods. Science 251, 794–796.

Reinfelder, J.R., Fisher, N.S., Fowler, S.W., Teyssié, J.-L., 1993. Release rates of trace elements and protein from decomposing planktonic debris. 2. Copepod carcasses and sediment trap particulate matter. J. Mar. Res. 51, 423–442.

Robison, B.H., Sherlock, R.E., Reisenbichler, K.R., 2010. The bathypelagic community of Monterey Canyon. Deep-Sea Res. II 57, 1551–1556. https://doi.org/10.1016/j.dsr2.2010.02.021.

Rudnick, R.L., Gao, S., 2003. Composition of the continental crust. In: Treatise on Geochemistry. vol. 3. pp. 1–64.

Saito, M.A., Moffett, J.W., 2002. Temporal and spatial variability of cobalt in the Atlantic Ocean. Geochim. Cosmochim. Acta 66, 1943–1953.

Sedwick, P.N., Church, T.M., Bowie, A.R., Marsay, C.M., Ussher, S.J., Achilles, K.M., Lethaby, P.J., Johnson, R.J., Sarin, M.M., McGillicuddy, D.J., 2005. Iron in the Sargasso Sea (BATS region) during summer: eolian imprint, spatio-temporal variability, and ecological implications. Glob. Biogeochem. Cycles 19, GB4006.

Shatova, O., Koweek, D., Conte, M.H., Weber, J.C., 2012. Contribution of zooplankton fecal pellets to particle flux in the mesopelagic Sargasso Sea. J. Plankton Res. 34, 905–921.

Shelly, R.U., Morton, P.L., Landing, W.M., 2015. Elemental ratios and enrichment factors in aerosols from the US-GEOTRACES North Atlantic transects. Deep-Sea Res. II 116, 262–272.

Sherrell, R., Boyle, E., 1992. The trace metal composition of suspended particles in the oceanic water column near Bermuda. Earth Planet. Sci. Lett. 111, 155–174.

Shieh, C.S., Duedall, I.W., 1988. Role of amorphous ferric oxyhydroxide in removal of anthropogenic vanadium from seawater. Mar. Chem. 25, 121–139.

Statham, P.J., Yeats, P.A., Landing, W.M., 1998. Manganese in the eastern Atlantic Ocean: processes influencing deep and surface water distributions. Mar. Chem. 61, 55–68.

Statham, P.J., Turner, T., Fones, G.R., 2005. Recycling of elements from particles in the ocean water column: evidence of in situ reduction and release of dissolved manganese. Geophys. Res. Abstr. 7, 07676.

Steinberg, D.K., Carlson, C.A., Bates, N.R., Johnson, R.J., Michaels, A.F., Knap, A.H., 2001. Overview of the U. S. JGOFS Bermuda Atlantic Time-Series Study (BATS): a decade look at ocean biology and biogeochemistry. Deep-Sea Res. II 48, 1405–1448.

Stern, J., Dellwig, O., Waniek, J.J., 2017. Deep sea fluxes of barium and lithogenic trace elements in the subtropical northeast Atlantic. Deep Sea Res., Part I 122, 72–80. https://doi.org/10.1016/j.dsr.2017.02.002.

Sternberg, E., Tang, D., Ho, T.-Y., Jeandel, C., Morel, F.M.M., 2005. Barium uptake and adsorption in diatoms. Geochim. Cosmochim. Acta 69, 2745–2752.

Stramska, M., Dickey, T.D., Marra, J., Plueddemann, A., Langdon, C., Weller, R., 1995. Bio-optical variability associated with phytoplankton dynamics in the North Atlantic Ocean during the spring and summer of 1991. J. Geophys. Res. 100, 6621–6632.

Sun, W.-P., Han, Z.-B., Hu, C.-Y., Pan, J.-M., 2016. Source composition and seasonal variation of particulate trace element fluxes in Prydz Bay, East Antarctica. Chemosphere 147, 318–327.

Sunda, W.G., Huntsman, S.A., 1995. Cobalt and zinc interreplacement in marine phytoplankton: biological and geochemical implications. Limnol. Oceanogr. 40, 1404–1417.

Talley, L.D., 1996. North Atlantic circulation and variability, reviewed for the CNLS conference. Phys. D 98, 625–646.

Tebo, B.M., Bargar, J.R., Clement, B.G., Dick, G.J., Murray, K.J., Parker, D., Verity, R., Webb, S.M., 2004. Biogenic manganese oxides: properties and mechanisms of formation. Annu. Rev. Earth Planet. Sci. 32, 287–328. https://doi.org/10.1146/annurev.earth.32.101802.120213.

Thomsen, L., Aguzzi, J., Costa, C., De Leo, F., Ogston, A., Purser, A., 2017. The oceanic biological pump: rapid carbon transfer to depth at continental margins during winter. Nat. Sci. Rep. 7, 10763. https://doi.org/10.1038/s41598-017-11075-6.

Tian, Z., Ollivier, P., Veron, A., Church, T.M., 2008. Atmospheric Fe deposition modes at Bermuda and the adjacent Sargasso Sea. Geochem. Geophys. Geosyst. 9, Q08007. https://doi.org/10.1029/2007GC001868.

Trapp, J.M., Millero, F.J., Prospero, J.M., 2008. Temporal variability of the elemental composition of African dust measured in trade wind aerosols at Barbados and Miami. Mar. Chem. 2008. https://doi.org/10.1016/j.marchem.2008.10.004.

Twining, B.S., Rauschenberg, S., Morton, P.L., Vogt, S., 2015. Metal contents of phytoplankton and labile particulate material in the North Atlantic Ocean. Prog. Oceanogr. 137, 261–283.

Van Beek, P., Francois, R., Conte, M., Reyss, J.-L., Souhant, M., Charette, M., 2007. ^{228}Ra/^{226}Ra and ^{226}Ra/Ba ratios in seawater and particles at the OFP site in the western Sargasso Sea near Bermuda. Geochim. Cosmochim. Acta 71, 71–86.

Verrado, D.J., Froelich, P.N., McIntyre, A., 1990. Determination of organic carbon and nitrogen in marine sediments using the Carlo Erba NA-1500 analyzer. Deep-Sea Res. 37, 157–165.

Wang, W.-X., Reinfelder, J.R., Lee, B.-G., Fisher, N.S., 1996. Assimilation and regeneration of trace elements by marine copepods. Limnol. Oceanogr. 41, 70–81.

Yao, W., Millero, F.J., 1996. Adsorption of phosphate on manganese dioxide in seawater. Environ. Sci. Technol. 30, 536–542. https://doi.org/10.1021/es950290x.

Youngbluth, M., Sornes, T., Hosia, A., Stemmann, L., 2008. Vertical distribution and relative abundance of gelatinous zooplankton, in situ observations near the Mid-Atlantic Ridge. Deep-Sea Res. II 55, 119–125. https://doi.org/10.1016/j.dsr2.2007.10.002.